If It's Not Broke, Break It, and then Break It Again: Understanding [Cp*Rh] Catalysts for Hydrogen Evolution by Investigation of Remarkably Inert Analogues

Thesis by Emily A. Boyd

In Partial Fulfillment of the Requirements for the Degree of
Bachelor of Science with Honors in Chemistry

University of Kansas
Lawrence, Kansas
May 2019

Acknowledgements

First, thank you to James for giving me the opportunity to do research in your group, and for encouraging an atmosphere where undergrads are trusted to motivate their own projects. My experience in the Blakemore group has been absolutely life-altering and has set the bar for anywhere I might end up in the future. I'm so glad I was in the right place at the right time to get to work with you!

Second, I will never stop being grateful for all of the things I've learned from Davide. Basically every thought I have about chemistry should be followed by a citation to "Helpful discussions with Davide Lionetti." Thank you so much for all of the time you have invested in explaining things to me, even when you have no time.

Thank you to Keaton for being a fantastic mentor and role model when I initially joined the group; I'm sorry I had to ask you how to set up the box trap (and the line) (and the e-chem cell) so many times.

Thank you to everyone else in the Blakemore group, past and present: Julie for stepping in as my mentor after Keaton left, and the many instances of bonding that followed; Will for our many many undergrad pacts; Amit for being a force of fun in the lab (I think I still owe you Cane's?); Wade for your eternal helpfulness and willingness to explain things from the very bottom up; Tyler for being a hard act to follow and for teaching me Origin despite my protests; David for teaching me e-chem and for your key insights into Game of Thrones; Yun for not letting me get away with anything, and for being an inspiring user of 2D NMR; Shaun for motivating me to wake up early and drink more water; Katie for exemplifying good time management; and Taylor for suffering through my attempts at explaining how to find a pK_a. I've also had a great time working with Riddhi, Joseph, Jonah, and Toni for the few months that we've overlapped.

I would also like to thank the other members of my thesis committee: Prof. Jackson, thank you for your help connecting me with James in the first place; and Prof. Barybin, thank you for taking a chance on letting me into your NMR class, and for your constant support since then.

As always, much appreciation to Victor for your endless expertise in pulling structures out of the tiniest of crystals. A huge thank you also to Sarah for help with NMR, and Justin for donating so much time to our EPR efforts.

And finally, thank you to my mom for being the first person I call in any bad, good, or even just boring situation; my dad for teaching me to look at the big picture; Clara for serenades when I'm stressed; and Zach for always being up to talk about really any research result, for always believing in me, and for always encouraging me to aim higher.

Chapter 1

SYNTHESIS, CHARACTERIZATION, AND ELECTROCHEMICAL ACTIVATION OF A DIPHOSPHINE-SUPPORTED HALF-SANDWICH MONOHYDRIDE

This chapter is adapted from a published manuscript: Boyd, E. A.; Lionetti, D.; Henke, W. C.; Day, V. W.; Blakemore, J. D. Preparation, Characterization, and Electrochemical Activation of a Model [Cp*Rh] Hydride. *Inorg. Chem.* **2019**, *58*, 3606-3615.

Abstract

Monomeric half-sandwich rhodium hydride complexes are often proposed as intermediates in catalytic cycles, but relatively few such compounds have been isolated and studied, limiting understanding of their properties. In this chapter, the preparation of a monomeric rhodium(III) hydride complex bearing the pentamethylcyclopentadienyl (Cp*) and bis(diphenylphosphino) benzene (dppb) ligands is reported. The hydride complex is formed rapidly upon addition of weak acid to a reduced precursor complex, Cp*Rh(dppb). Single-crystal X-ray diffraction data for the [Cp*Rh] hydride, which were previously unavailable for this class of compounds, provide evidence of the direct Rh–H interaction. Complementary infrared spectra show the Rh–H stretching frequency at 1986 cm^{-1}. In contrast to results with other [Cp*Rh] complexes bearing diimine ligands, treatment of the isolated hydride with strong acid does not result in H_2 evolution. Electrochemical studies reveal that the hydride complex can be reduced only at very negative potentials (ca. –2.5 V vs. ferrocenium/ferrocene), resulting in Rh–H bond cleavage and H_2 generation. Experimentally determined thermochemical parameters for reactions of the [Cp*Rh] hydride and its reduced form provide a rationale for the observed reactivity differences between the dppb and analogous diimine frameworks that can generate H_2 with moderately strong acids. These results are discussed in the context of development of design rules for improved catalysts bearing the [Cp*] ligand.

Introduction

Modern society's reliance on hydrocarbons as the fuel to power virtually every human process must soon be curbed in order to minimize the anthropogenic carbon dioxide emissions that are leading to accelerated climate change. Energy-efficient and environmentally sustainable generation of dihydrogen (H_2) is one attractive means of addressing this challenge from multiple

angles. First, H_2 could serve as a carbon-free alternative to traditional fossil fuels, as water is the only product of combustion of H_2. It is also a very energy dense fuel by mass; as comparison, the heat of combustion of H_2 is 34 kcal g^{-1} compared to 11.4 kcal g^{-1} for octane. While the changes in infrastructure necessary for large-scale conversion to a hydrogen fuel economy are likely far off, the existing market for H_2 offers a more immediate application of efficient production methods. The annual demand for hydrogen in the United States (primarily for use in oil refining and in the Haber-Bosch process) totals up to 13.8 million metric tons.[1] Approximately 95% of this feedstock hydrogen is currently produced via steam-reforming of methane, in which methane from natural gas is combined with steam to generate hydrogen with CO_2 as a byproduct.[2] Moreover, the reaction is performed at 700–1000ºC, a temperature which is typically attained by consumption of fossil fuels and therefore leads to further emission of CO_2.

A promising clean alternative for production of hydrogen as a feedstock and a potential fuel is to form H_2 directly from its simplest components: two protons and two electrons. This could be accomplished by the water-splitting reaction depicted in Scheme 1, in which water provides an environmentally sustainable source of protons and electrons. The net reaction is uphill by 119 kcal mol^{-1}, necessitating some form of energy input.[3,4] Ideally, electricity from a renewable energy source (such as wind or solar) could drive electrocatalysis of the water-splitting reaction.

$2H_2O \rightleftharpoons 4H^+ + 4e^- + O_2$	$\Delta G^o = 111.6$ kcal mol^{-1}	(1)
$4H^+ + 4e^- \rightleftharpoons 2H_2$	$\Delta G^o = 2(3.6$ kcal $mol^{-1})$	(2)
$2H_2O \rightleftharpoons 2H_2 + O_2$	$\Delta G^o = 118.8$ kcal mol^{-1}	(3)

Scheme 1.1: Free energy changes associated with the water-splitting reaction in CH_3CN.

Notably, the half-reaction for combination of protons and electrons to generate H_2 is only slightly endergonic (ΔG^o = 3.6 kcal mol^{-1}); however, extra energy input in the form of electrochemical

overpotential is required to overcome the activation energy of the reaction and obtain appreciable reaction rates. Catalysts for hydrogen evolution lower this kinetic barrier (and thus the overpotential) by streamlining the paths taken by protons and electrons toward their eventual combination into H_2. A detailed understanding of the properties that allow good catalysts to efficiently manage the reactants is therefore necessary in order to develop design rules to kinetically favor hydrogen evolution and minimize overpotentials.

Our group has selected a Rh(III) complex supported by Cp* and bpy (Cp* = η^5-pentamethylcyclopentadienyl, bpy = κ^2-2,2'-bipyridyl) as a model hydrogen evolution catalyst for this type of mechanistic interrogation. First reported by Grätzel and Kölle in 1987, this catalyst is an ideal model system both because of its straightforward, modular synthesis (facilitating structure-function studies) and because of the ubiquity of the Cp* and bpy ligands in inorganic and organometallic chemistry (making insight into their roles potentially transferrable to other systems).[5] In cases where catalysis is driven electrochemically, two-electron reduction of the rhodium(III) species in the presence of suitably strong acids (e.g., anilinium triflate, pK_a = 10.6 in CH_3CN[6]) results in quantitative formation of H_2 and regeneration of the rhodium(III) complex.[7] Because of its high efficiency and stability, the complex has been immobilized on various surfaces to perform catalysis, used to hydrogenate unsaturated organic molecules, and extended to a biochemical application as a catalyst for hydride transfer in the conversion of NAD+ to NADH.[8,9,10,11]

The mechanism of H_2 generation with this catalyst system was originally proposed to involve two-electron reduction of the precatalyst to generate a rhodium(I) complex that is subsequently protonated to form a [Cp*Rh] hydride species. This hydride complex would then undergo protonolysis to release H_2.[12] The same hydride intermediate has also been implicated in generation

of NADH from NAD^+ in related work on electrochemically-driven enzymes.[8,13] Signals consistent with the presence of a hydride under stringent reaction conditions (large excess of sodium formate, $Na^+[HCOO]^-$, as hydride source) have been observed by proton nuclear magnetic resonance (^1H NMR) in the case of a catalyst supported by 6,6′-dimethyl-2,2′-bipyridyl.[14] The analogous [Cp*Ir] hydride is well known, and has even been crystallographically characterized, lending credence to the possibility of the involvement of an analogous species in the chemistry of [Cp*Rh] complexes.[15] Nonetheless, despite the proposed involvement of this hydride complex in a number of catalytic mechanisms, neither isolation nor complete *in situ* characterization of this compound has been reported; thus, the involvement of alternative formulations of this protonated species in catalysis cannot be ruled out.

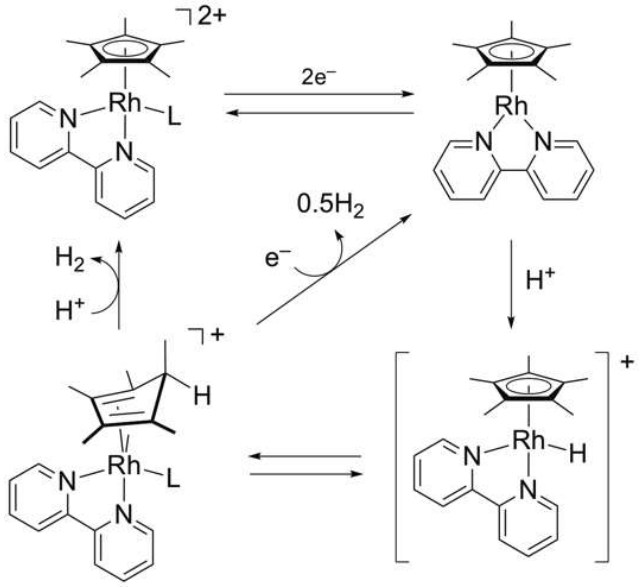

Scheme 1.2: Hydrogen evolution catalyzed by Cp*Rh(bpy). L = halide or coordinated solvent (e.g., CH_3CN).

Indeed, recent work has shown that under several conditions, protonation of $Cp^*Rh^I(bpy)$ results in formation of an η^4-pentamethylcyclopentadiene (Cp*H) species rather than the presumed rhodium hydride. Miller and coworkers reported that addition of strong acid (HCl, $pK_a < 10.30$ in CH_3CN[16]) to Cp*Rh(bpy) results in generation of bound [Cp*H];[17] we have found that the weak

acid triethylammonium (pK_a = 18.8 in CH_3CN[6]) can be exploited to cleanly generate complexes bearing [Cp*H] that can subsequently be isolated and stored in pure form on preparative scale (Scheme 2).[18,19] The isolated [Cp*H] species react with further proton equivalents to generate H_2, indicating that they cannot be eliminated as intermediates in the catalytic cycle of $[Cp^*Rh(bpy)Cl]^+$. Beyond the Cp*Rh(bpy) hydrogen evolution system, the non-innocence of Cp* and the role of [Cp*H] species in various catalytic transformations has been a subject of growing interest. For example, Peters and coworkers very recently reported EPR characterization of ligand-protonated decamethylcobaltocene, the thermochemical properties of which suggest possible application as a PCET reagent for generation of very weak bonds (< 30 kcal mol^{-1}).[20] Interestingly, they observe both *exo* and *endo* orientation of the [Cp*H] "special" proton with respect to the Co center, suggesting direct protonation at the ligand. This finding contrasts markedly with our X-ray crystallography and 2D NMR experiments showing that the special proton in $[(Cp^*H)Rh(bpy)]^+$ is found exclusively with *endo* disposition both in solid state and solution.[19] This orientation coupled with Miller's observation of a hydride signal at low temperature followed by conversion to [Cp*H] upon warming suggest that the initial site of protonation may be at the rhodium center prior to tautomerization onto the Cp* ring.[17] Given this result, it remains unclear whether the observed [Cp*H] complexes are active in catalysis or if they are off-cycle species that interconvert with a transient metal-hydride which serves as the active intermediate toward H_2 evolution. We therefore targeted generation of an isolable [Cp*Rh] monohydride for comparison to the ligand-protonated species in order to gain insight into possible modes of reactivity in Cp*Rh(bpy)-catalyzed hydrogen evolution. Such a study of chemical behavior dependent on protonation site across otherwise analogous complexes could provide a rationale for understanding differences in

reactivity between the rapidly expanding class of [Cp*H] complexes and their more conventional metal-hydride isomers.

In selecting a strategy to meet this research goal, we were encouraged both by literature reports of [Cp*Rh] hydride complexes stabilized by phosphine ligands and by computational studies which suggest replacement of bipyridine with a bidentate diphosphine ligand in Cp*Rh(bpy) might favor hydride formation.[21] Early work from Klingert and Werner showed that treatment of $Cp^*Rh(PMe_3)_2$ with NH_4PF_6 affords $[Cp^*Rh(PMe_3)_2H]^+$.[22] Faller and co-workers later found that an analogous monohydride is sufficiently stable for purification by column chromatography.[23] This finding is complemented by reports of crystallographic characterization of rhodium hydride compounds stabilized by phosphine ligands but not ligated by [Cp*],[24] as well as a more recent report of a crystallographically characterized $[Cp^*Fe^{II}]$ complex stabilized by phosphine ligands.[25] In another key study of interest here, Faraone and co-workers demonstrated preparation of a diphosphine-ligated [CpRh] hydride, although no structural data were collected and the hydride ligand could not be detected by ^1H NMR.[26] Other work from Klingert and Werner includes studies of Rh complexes with bridging PMe_3 ligands.[27,28] Complementary to the monohydride diphosphine [Cp*Rh] complex of interest here, Jones has studied the properties of dihydride monophosphine [Cp*Rh] complexes.[29,30] Lluch, Lledós, and Heinekey investigated a related [Cp*Ir] dihydride with a chelating phosphine ligand, and showed that one [H] ligand was sufficiently hydridic to evolve H_2 by reaction with trace water.[31] However, we are unaware of prior studies of the electrochemical properties of [Cp*Rh] hydride complexes. Such work would complement studies examining reduction of analogous diphosphine [Cp*Rh] complexes without hydride ligands, work with analogous half-sandwich cobalt complexes, and quite recent work from

Collomb and co-workers that examined electrochemical H_2 generation pathways in rhodium poly(bipyridyl) complexes. [32,33]

In this chapter, the isolation and study of a [Cp*Rh] monohydride supported by the bidentate chelate ligand bis(diphenyl)phosphino benzene (dppb) are described. The new complex Cp*Rh(dppb) (**2** in Scheme 3) reacts with one equivalent of anilinium (pK_a = 10.6 in CH_3CN[6]) to cleanly afford the hydride complex $[Cp^*Rh(dppb)H]^+OTf^-$ (**3**). Electrochemical studies show that this compound is reduced at –2.32 V versus the ferrocenium/ferrocene couple (denoted hereafter as $Fc^{+/0}$), giving rise to H_2. Treatment of **3** with excess strong acid ($[DMFH]^+$, pK_a = 6.1 in CH_3CN[6]) does not result in hydrogen evolution, consistent with experimentally determined thermochemical values associated with the hydride complex. These results are discussed in the context of developing design rules for new [Cp*Rh]-based catalysts.

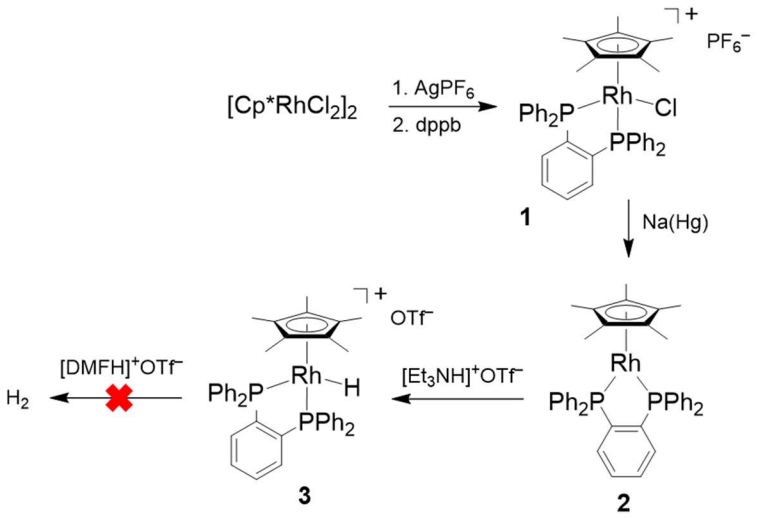

Scheme 1.3: Summary of preparation and reactivity of [Cp*Rh] complexes supported by the dppb ligand.

Synthesis and Characterization of [Cp*Rh^{III}(dppb)Cl][PF_6] (1)

*Synthesis and Crystal Structure of **1***

The dppb ligand was metallated to form complex **1** in a procedure similar to that used for the preparation of analogous bipyridyl [Cp*Rh] complexes (Scheme 1.3, see Appendix 1 for General Considerations). 2 equiv. of commercially available dppb was added as a CH_2Cl_2 solution to a suspension of 1 equiv. of $[Cp^*RhCl_2]_2$ in CH_2Cl_2. Addition of 2 equiv. of $AgPF_6$ in CH_2Cl_2 solution as a chloride-abstracting agent resulted in rapid precipitation of colorless solid AgCl and a change in the color of the reaction mixture from brick-red to orange. After filtration and triteration from a concentrated CH_2Cl_2 solution with Et_2O, pure material was obtained by crystallization with vapor diffusion of Et_2O into a concentrated THF solution of **1** (see Scheme 1.3, 78% yield). The same strategy was employed to obtain single-crystals suitable for X-ray diffraction (XRD) studies. The geometry at the formally rhodium(III) center in **1** is pseudo-octahedral, with a first coordination sphere around the metal center containing [Cp*], the expected κ^2-dppb, and a single bound chloride anion (Figure 1.1, see Appendix 3 for detailed structural information). The dppb is forced downward by clash with the bulky [Cp*] ligand: in the structure of **1**, the angle between the plane containing the [Cp*] ligand and the plane containing Rh, P1, and P2 is 66°; in the analogous $[Cp^*Rh(bpy)Cl]^+$ complex,[34] the angle between the [Cp*] plane and the plane containing Rh and the bound nitrogen atoms is 59°. This suggests that the steric bulk of the dppb framework (specifically that of the terminal phenyl groups) has a substantial effect on the geometry of the interaction between the bidentate ligand and the [Cp*Rh] motif.

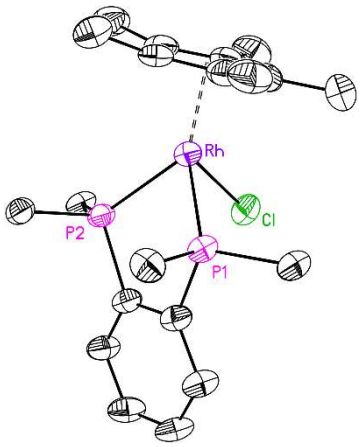

Figure 1.1: Crystal structure of **1**. H atoms, PF_6 counteranion, and terminal phenyl groups omitted for clarity.

*NMR Characterization of **1***

All complexes were characterized by Nuclear Magnetic Resonance spectroscopy (NMR) to confirm structure and provide an estimate of their purity. The ^{1}H NMR spectrum of **1** (Figure 1.2) shows a triplet at 1.56 Hz that integrates to 15 equivalent protons, corresponding to the methyl groups of the freely-rotating Cp* ligand. The triplet splitting is the result of coupling to the two equivalent I = ½ phosphorus atoms of the dppb ligand ($^3J_{H,P}$ = 3.4 Hz), confirming coordination of both Cp* and dppb to the rhodium center. The signals in the aromatic region integrate to a total of 24 protons, consistent with the number of aromatic protons in the dppb ligand; moreover, based on a full suite of 2D NMR experiments, we were able to fully assign the spectrum (see Figure 1.2 for numbering scheme and Appendix 2 for 2D NMR spectra). Due to the C_s symmetry of the complex, the dppb ligand only contains one mirror plane lying perpendicular to the benzene bridge while both sets of two phenyl groups connected to the same phosphorus atom are inequivalent (i.e., one set is tilted up toward the Cp* ring while the other set is tilted down toward the chloride ligand). From homonuclear ^{1}H correlation spectroscopy (COSY, Figure A2.1), in which cross peaks indicate coupling between proton signals, it is possible to separate the eight aromatic multiplets into three distinct groups of isolated coupling networks corresponding to the “up”

phenyl protons, the "down" phenyl protons, and the benzene bridge protons. Based on integration of the 1D spectrum and further analysis of the COSY cross peaks (see Appendix 2 for detailed rationale for assignments), we can assign characteristic peak shapes to the *ortho*, *para*, and *meta* protons of the phenyl rings with respect to the phosphorus atom; assignment of the *ortho* protons (positions 4 and 8) as the most complicated multiplet structures is supported by their proximity to the $I = ½$ phosphorus and rhodium nuclei, giving rise to further detectable couplings. Furthermore, Nuclear Overhauser Effect Spectroscopy (NOESY) facilitated differentiation between the "up" and "down" phenyl protons and the two proton environments in the benzene backbone. In NOESY, cross peaks reveal the proximity of protons to each other in space. The more upfield set of phenyl protons shows a NOESY cross peak with the Cp* methyl protons (Figure A2.3) and can therefore be identified as the "up" phenyl groups. This assignment is consistent with the orientation of the "down" phenyl protons toward the deshielding chloride ligand and "up" phenyl protons toward the shielding Cp* methyl groups, giving rise to downfield and upfield shifts, respectively.

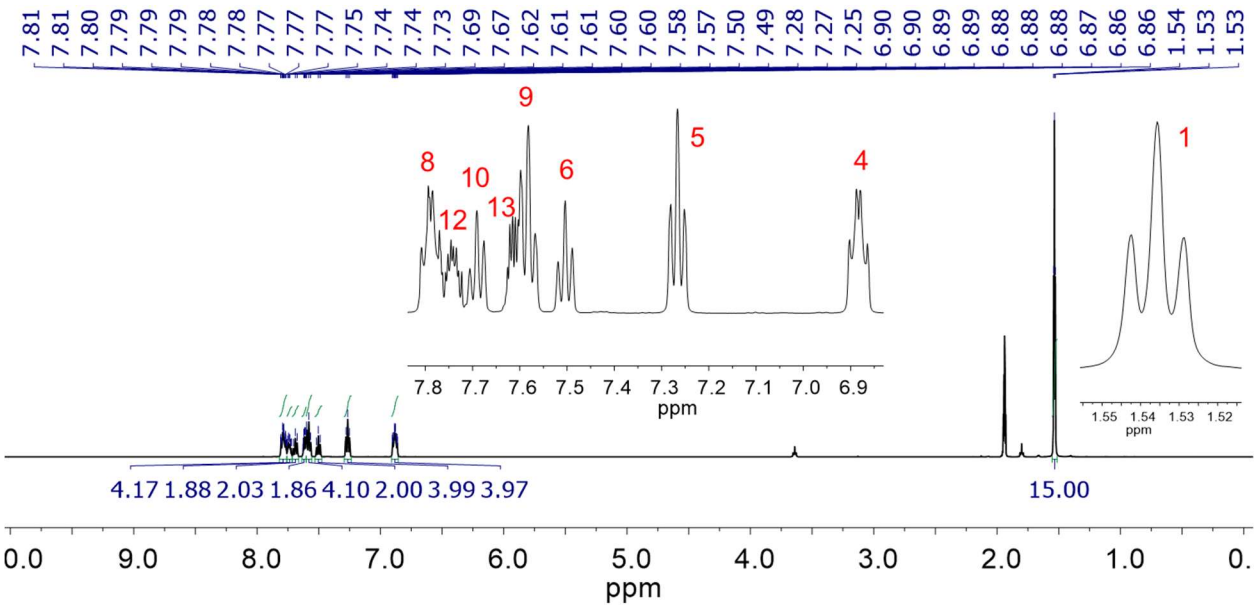

Figure 1.2: ^{1}H NMR spectrum (500 MHz, CD_3CN) of **1**.

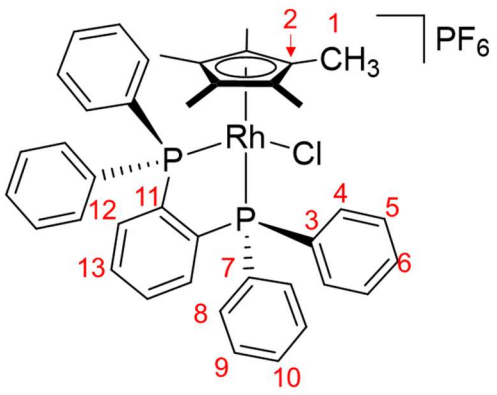

Figure 1.3: Numbering scheme for assignment of NMR data for complex **1**.

Assignment of the $^{13}C\{^{1}H\}$ NMR spectrum of **1** (Figure 1.4) also required 2D techniques to account for all thirteen carbon environments in the molecule, as the presence of the spin-active phosphorus and rhodium nuclei leads to complicated splitting and signal overlap. Heteronuclear single quantum coherence (HSQC) spectroscopy is a 2D NMR experiment in which cross peaks between the ^{1}H and $^{13}C\{^{1}H\}$ spectrum indicate which protons are bonded to which carbon atoms. The HSQC spectrum of **1** provides unambiguous evidence for direct correlation of several peaks in the $^{13}C\{^{1}H\}$ spectrum with proton environments in the ^{1}H spectrum (see Figure A2.4). The peaks corresponding to the *ortho* and *meta* carbon environments of both the "up" and "down" phenyl rings appear as triplets with coupling constants of approximately 6 Hz; the precise source of this coupling is unclear, especially because the magnitude of the coupling does not decrease around the ring as distance from the spin-active nuclei increases as is observed in the free ligand.[35] However, nearly identical ~6 Hz triplet profiles are observed for all of the *ortho* and *meta* carbons of the dppb phenyl groups in the series of complexes described here, suggesting that the unexpected splitting pattern is brought about by bidentate chelation of dppb to the rhodium center. While the carbon peaks between 131.2-131.6 ppm are too closely spaced to distinguish with

confidence, every proton environment shows a distinct cross peak in this region, indicating that all primary and tertiary carbon environments in **1** can be accounted for.

The last type of 2D NMR used to assign the spectra of **1** was heteronuclear multiple bond correlation (HMBC) spectroscopy, which is identical to HSQC except its cross peaks show correlation between carbons and protons separated by two or three bonds. This technique is especially useful in identifying quaternary carbons, which typically appear as low-intensity signals because of their slow relaxation times. **1** has four quaternary carbon environments. First, the Cp* ring carbon environment is easily identified based on comparison with previous work as the peak at 104.36 ppm, which appears as a doublet of triplets (J = 5.5, 2.7 Hz) due to coupling to one rhodium and two phosphorus nuclei. Cross peaks in the HMBC spectrum of **1** (Figure A2.5) reveal the remaining three quaternary carbons (see Appendix 2).

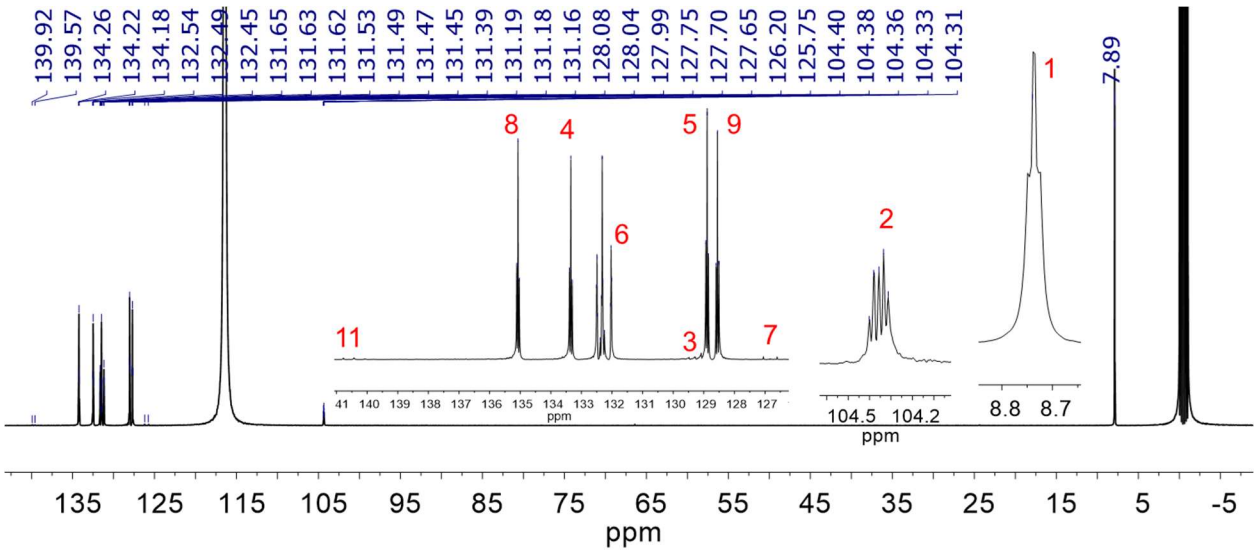

Figure 1.4: $^{13}C\{^{1}H\}$ NMR spectrum (126 MHz, CD_3CN) of **1**.

Finally, the $^{31}P\{^{1}H\}$ and ^{19}F NMR spectra of **1** (upper panel of Figure 1.5 and Figure A2.6) are fully consistent with the structure. The phosphorus atoms in dppb couple to rhodium and appear as a doublet at 58.32 ppm with $^{1}J_{P,Rh}$ = 129.9 Hz. The $^{31}P\{^{1}H\}$ NMR of **1** also includes a septet at

–147.65 ppm (see Figure A2.7). This signal and the doublet at –73.77 ppm in the ^{19}F NMR (both with $^{1}J_{F,P}$ = 706 Hz) correspond to the $[PF_6]^-$ counteranion.

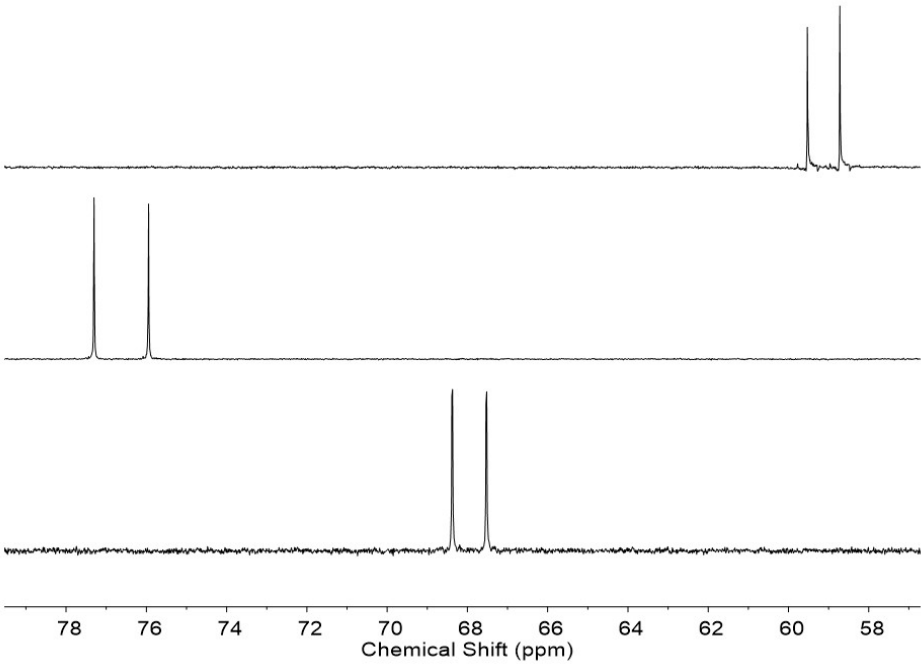

Figure 1.5: $^{31}P\{^{1}H\}$ NMR (162 MHz) of **1** (top, CD_3CN, $^{1}J_{P,Rh}$ = 131 Hz), **2** (middle, C_6D_6, $^{1}J_{P,Rh}$ = 220 Hz), and **3** (bottom, CD_3CN, $^{1}J_{P,Rh}$ = 138 Hz).

*Cyclic Voltammetry of **1***

The first cathodic sweep of a cyclic voltammogram (CV) of **1** beginning near –0.3 V displays an initial reduction event centered at –0.85 V vs. $Fc^{+/0}$ (Figure 1.6). The peak-to-peak separation of the cathodic and anodic waves is significant (ca. 300 mV), suggesting a chemical reaction occurs upon reduction. Furthermore, synthetic work (*vide infra*) and comparison of peak areas in a solution containing a 1:2 mixture of **1** and ferrocene suggests that the reduction of **1** involves transfer of two electrons (Figure 1.6). This agrees well with prior work on [Cp*Rh] diimine complexes, which typically undergo 2e$^-$ reduction near –1.0 V vs. $Fc^{+/0}$.[7,**Error! Bookmark not defined.**,36] The reduction event for **1** displays the typical profile of an ECE mechanism, in which an initial electrochemical reduction is followed by a chemical reaction (here, a structural rearrangement

upon loss of bound chloride) that generates a transient complex with a more positive reduction potential (i.e., $[Cp^*Rh^{II}(dppb)]^+$). Therefore, a second electron is immediately transferred following the first, giving rise to the net two-electron wave. A similar profile for this $2e^-$ reduction is observed in voltammetry across a range of scan rates (see Figure 1.7), suggesting that the coupled chemical reactions are reasonably fast on the timescale of voltammetry. The observed peak currents for both the reduction and oxidation events vary linearly with the square root of scan rate, confirming both the oxidized and reduced forms of **1** are soluble and freely diffusing (Figure 1.7).

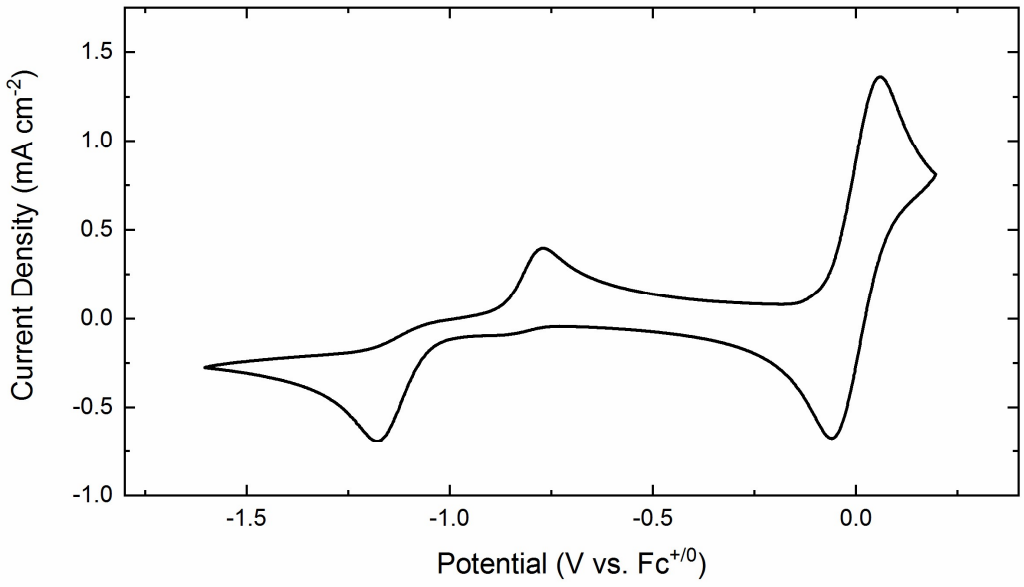

Figure 1.6: Cyclic voltammetry of **1** (MeCN, 0.1 M $[^nBu_4N][PF_6]$, 100 mV/s) with two equivalents of ferrocene. The second complete cycle of voltammetry is shown here.

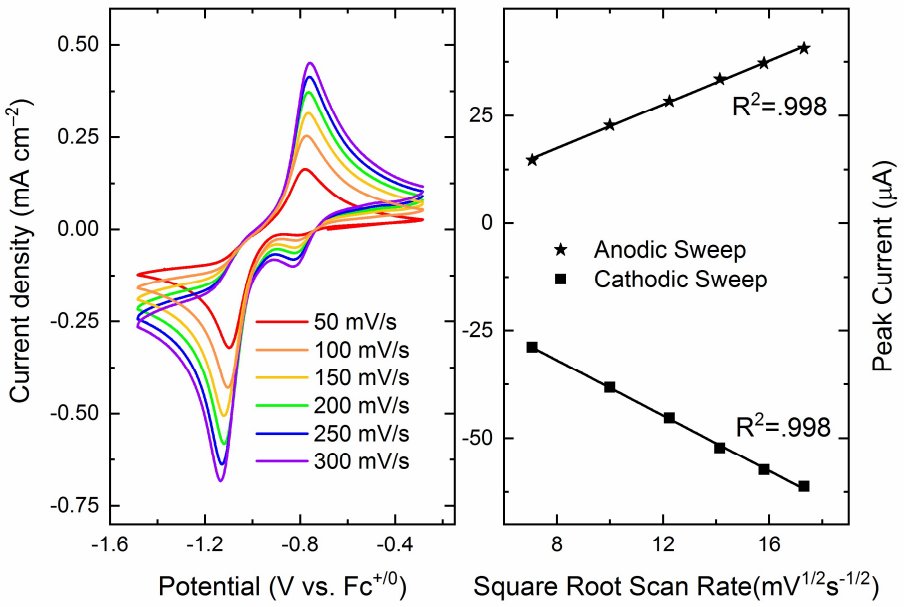

Figure 1.7: Left: cyclic voltammetry of **1** at varying scan rate in MeCN (0.1 M [^{n}Bu$_4$N][PF$_6$]). Right: linear dependence of peak current on square root of scan rate with the y-intercept set to 0.

As shown in Figure 1.7, in the second and subsequent cycles of voltammetry, a new reductive feature appears at a slightly more positive potential than the dominant reduction wave. Specifically, a small new reductive wave appears with $E_{p,c} = -0.82$ V. The appearance of this wave upon multiple cycling is consistent with initial reduction of **1** (virtually all chloride-bound when dissolved in the electrolyte solution) by two electrons to form the rhodium(I) species **2** (Scheme 1.3). Subsequent re-oxidation and ligand coordination can result in two possible products, chloride-bound **1** or the analogous solvento complex, [Cp*Rh(dppb)(NCMe)]$^{2+}$. The small, additional reductive wave thus corresponds to two-electron reduction of [Cp*Rh(dppb)(NCMe)]$^{2+}$ to form **2**. The shift in reduction potential for the solvento species is consistent with analogous observations in bpy-supported Co, Rh, and Ir systems.[37]

This electrochemical response is reminiscent of that of [Cp*Rh] complexes bearing bpy or related 4,4′-disubstituted 2,2′-bipyridyl ligands.[7,38] In the case of the parent bpy system, a single

2e⁻, ECE-type reduction event gives rise to a five-coordinate 18e⁻ species.[5] The five-coordinate complex Cp*Rh(bpy) has been chemically prepared and structurally characterized, confirming its identity as the product of reduction of the rhodium(III) starting material. Notably, this formally rhodium(I) complex displays significant delocalization of electron density into the π-system of the bpy ligand, as judged by single-crystal XRD and UV-visible spectroscopy.[39]

Synthesis and Characterization of Cp*Rh^{I}(dppb) (2)

In accord with the two-electron reduction of **1** observed by cyclic voltammetry, treatment of a THF suspension of **1** with sodium amalgam ($E°$ ≈ –2.4 V[40], 10 equiv.) results in generation of **2**. Over the course of the reaction, the suspension of orange **1** in THF darkens considerably to form a dark red, homogeneous solution. Following filtration and extraction with hexanes, diamagnetic **2** can be isolated in pure form (85% yield).

Characterization of **2** by ^{1}H NMR (Figure 1.8) indicates retention of both the [Cp*] and dppb ligands, as the 15 equivalent protons of the freely rotating [Cp*] ring still show coupling to the two equivalent bound phosphorus atoms ($^{3}J_{H,P}$ = 1.8 Hz), similar to data collected for **1** ($^{3}J_{H,P}$ = 3.4 Hz). The spectrum is also consistent with generation of a five-coordinate, C_{2v} species containing a mirror plane in the plane of the benzyl bridge in the dppb ligand, causing the six inequivalent proton environments in the phenyl groups of **1** to collapse to three environments which can be assigned by analogy to the peak shapes for the phenyl protons of **1** (see Appendix 2)**.** NOESY was again used to differentiate between the two benzene proton environments (Figure A2.8). The phosphorus-adjacent proton (position 8) exhibits more defined splitting structure, consistent with stronger coupling to the phosphorus atoms through fewer bonds.

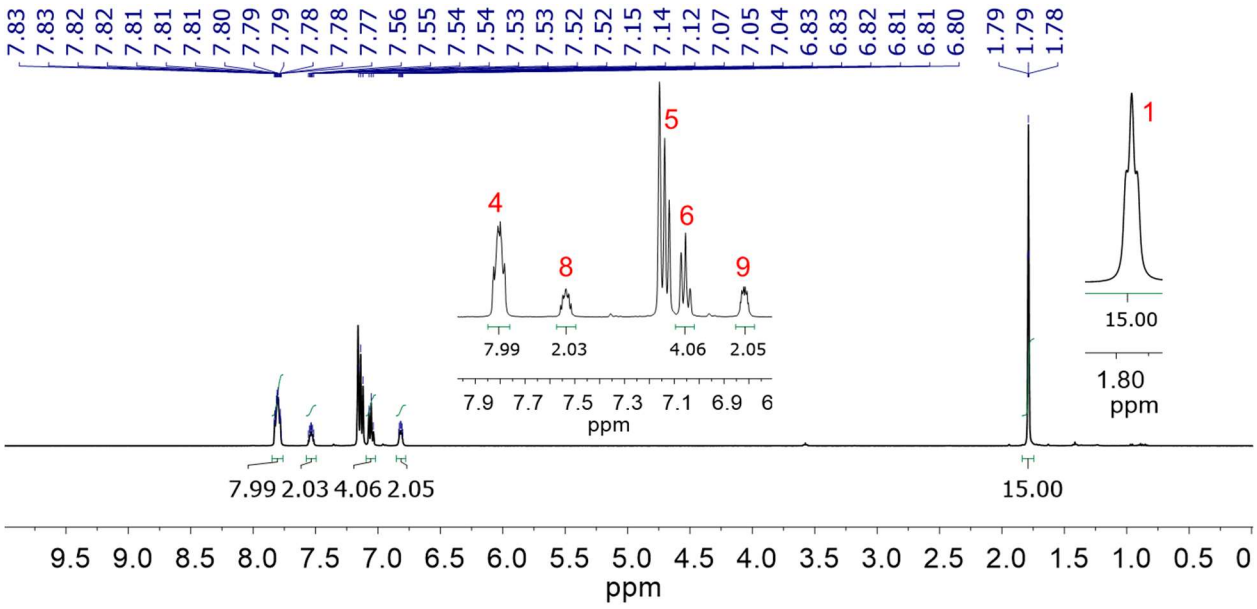

Figure 1.8: ^{1}H NMR spectrum (500 MHz, C_6D_6) of **2**.

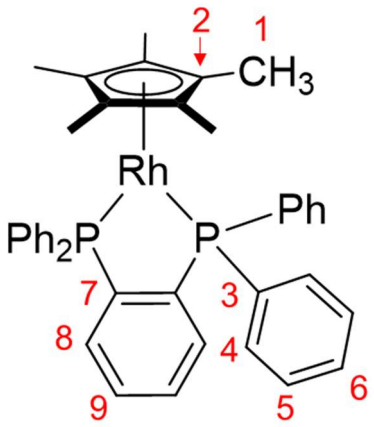

Figure 1.9: Numbering scheme for assignment of NMR data for complex **2**.

The $^{13}C\{^{1}H\}$ NMR spectrum of **2** (Figure 1.10) shows the nine expected signals. The Cp* methyl carbons appear as a singlet at 10.84 ppm; the loss of coupling to the phosphorus atoms ($^{3}J_{C,P}$ = 1.5 Hz in **1**) is consistent with the reduction in the $^{4}J_{H,P}$ for the Cp* methyl protons of **2** compared to **1**. Similarly, the Cp* ring carbons of **2** appear as a quartet (J = 2.8 Hz) at 96.06 ppm rather than the triplet of doublets in **1**, indicating that the Cp* ring carbon – phosphorus coupling has decreased to be approximately equal in magnitude to the carbon – rhodium coupling (which

remains nearly constant at approximately 2.8 Hz), causing the complicated splitting to collapse into a quartet. The dppb carbon signals in the aromatic region can be assigned via 2D spectroscopy (see Appendix 2 for spectra and assignment rationale).

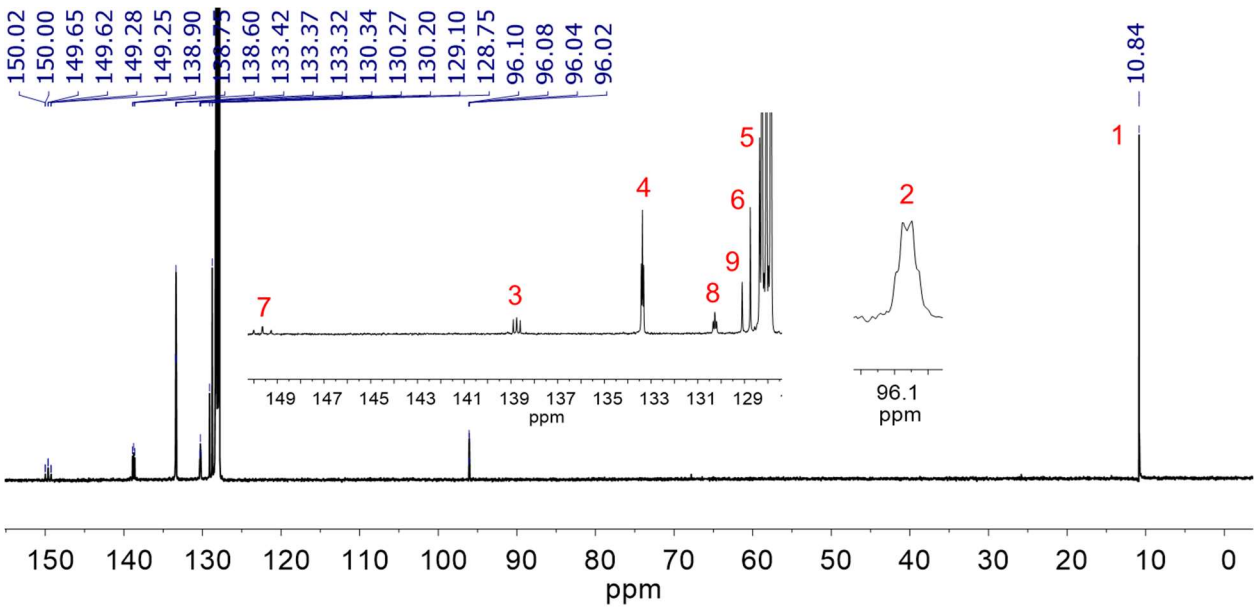

Figure 1.10: $^{13}C\{^{1}H\}$ NMR spectrum (126 MHz, C_6D_6) of **2**.

$^{31}P\{^{1}H\}$ NMR spectra (Figure 1.5, middle spectrum) support assignment of reduction of the rhodium metal center; $^{1}J_{P,Rh}$ increases from 131 Hz in **1** to 220 Hz in **2**, in accord with formation of a more electron-rich rhodium center which can engage in backdonation to the pi-acidic phosphine moieties. The phosphine resonances also shift downfield (ca. 9 ppm) upon reduction. Crystals of this complex suitable for XRD studies could not be obtained due to the high solubility of this species in most organic solvents. However, as the ^{1}H NMR does not indicate the presence of additional ligands bound to the Rh center and is consistent with C_{2v} symmetry, we conclude that this complex, similar to Cp*Rh(bpy), is a five-coordinate, $18e^-$ complex.

*Cyclic Voltammetry of **2***

Cyclic voltammetry data obtained with isolated **2** (Figure 1.11, red scan) confirm that this compound is the product of electrochemical reduction of **1**. Starting an initial anodic sweep from

reducing potentials, we observe a sole oxidation wave ($E_{p,a}$ = –0.73 V) coupled to a sole reduction wave ($E_{p,c}$ = –0.82 V). This two-electron event is centered at –0.78 V vs. $Fc^{+/0}$, slightly more positive than the rhodium(III/I) couple measured for the chloride-containing starting material **1** (Figure 1.11, orange scan). This is consistent with generation of the more oxidizing $[Cp^*Rh(dppb)(NCMe)]^{2+}$ upon 2e⁻ oxidation of **2**. The reduction wave measured for this solvento complex generated from **2** *in situ* (Figure 1.7) is shifted positive from the reduction wave measured for chloride-bound **1** but coincides with the new anodic feature that appears in the second scan of **1**, supporting our earlier assignment of this new feature as reduction of the solvento complex. Because the 2e⁻ couple is the result of potential inversion in an ECE process with a fast chemical step, the observed peak cathodic potential ($E_{p,c}$) corresponds to the $Rh^{III/II}$ reduction while the observed peak anodic potential ($E_{p,a}$) corresponds to the $Rh^{II/I}$ oxidation. By assuming the electrochemical electron transfer rates for the [Cp*Rh] species are comparable to those for ferrocene (i.e., $\Delta E_p(Fc^{+/0}) \approx \Delta E_p(Rh^{n+1/n})$), we used the peak-to-peak separation of ferrocene to extrapolate the one-electron reduction potentials for the $Rh^{III/II}$ and $Rh^{II/I}$ couples using eqs. 6 and 7.

$$\Delta E_p(Fc^{+/0}) = \Delta E_p(Rh^{n+1/n}) = E_{p,a} - E_{p,c} \quad (4)$$

$$E_{1/2} = \frac{E_{p,a} + E_{p,c}}{2} \quad (5)$$

$$E_{1/2}(Rh^{III/II}) = \frac{2E_{p,c} + \Delta E_p(Fc^{+/0})}{2} \quad (6)$$

$$E_{1/2}(Rh^{II/I}) = \frac{2E_{p,a} - \Delta E_p(Fc^{+/0})}{2} \quad (7)$$

Coincidentally, the 100 mV peak-to-peak separation of the ECE process in **2** is identical to that of the $1e^-$ couple in ferrocene (Figure 1.12), resulting in $E_{1/2}(Rh^{III/II}) = E_{1/2}(Rh^{II/I}) = -0.78$ V vs. $Fc^{+/0}$. This result is fully consistent with computerized numerical simulations of the CV data.[41] Scan rate-dependent studies confirm that **2**, and its oxidation product $[Cp^*Rh(dppb)(NCMe)]^{2+}$, are freely diffusing, soluble species (Figure 1.13).

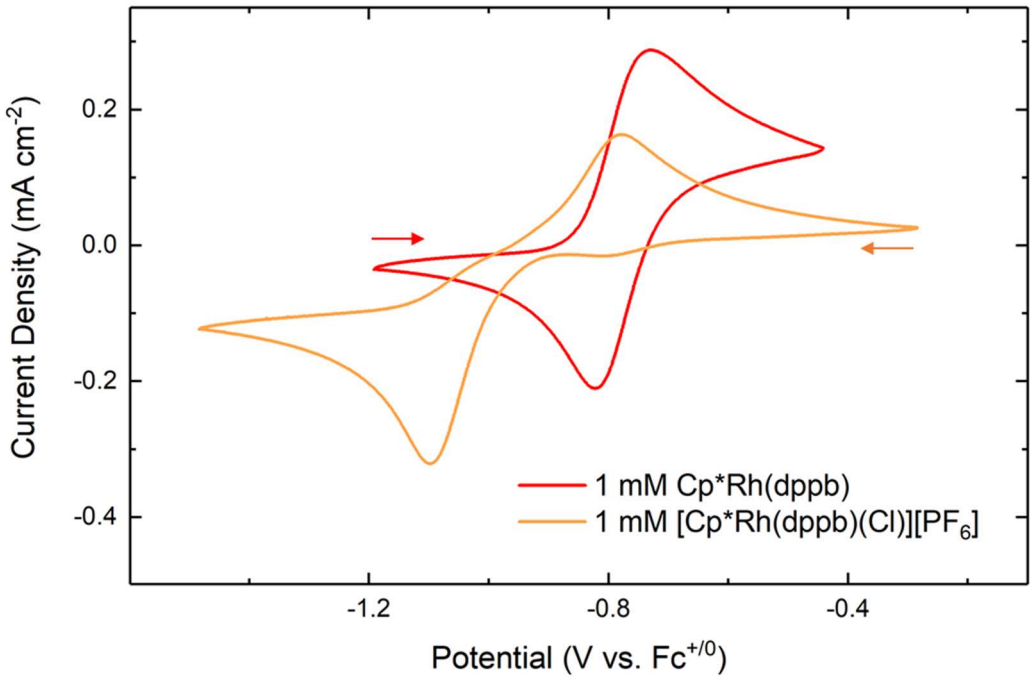

Figure 1.11: Cyclic voltammetry of **1** (orange scan, 1 mM) and **2** (red scan, 1 mM). Electrolyte: 0.1 M $TBAPF_6$ in CH_3CN, scan rate: 100 mV/s, electrode: highly oriented pyrolytic graphite. The initial potential of the voltammogram of **1** (orange) is at ca. –0.30 V, and the initial potential of the voltammogram of **2** (red) is at ca. –1.2 V. The second cycle of voltammetry is shown for both complexes.

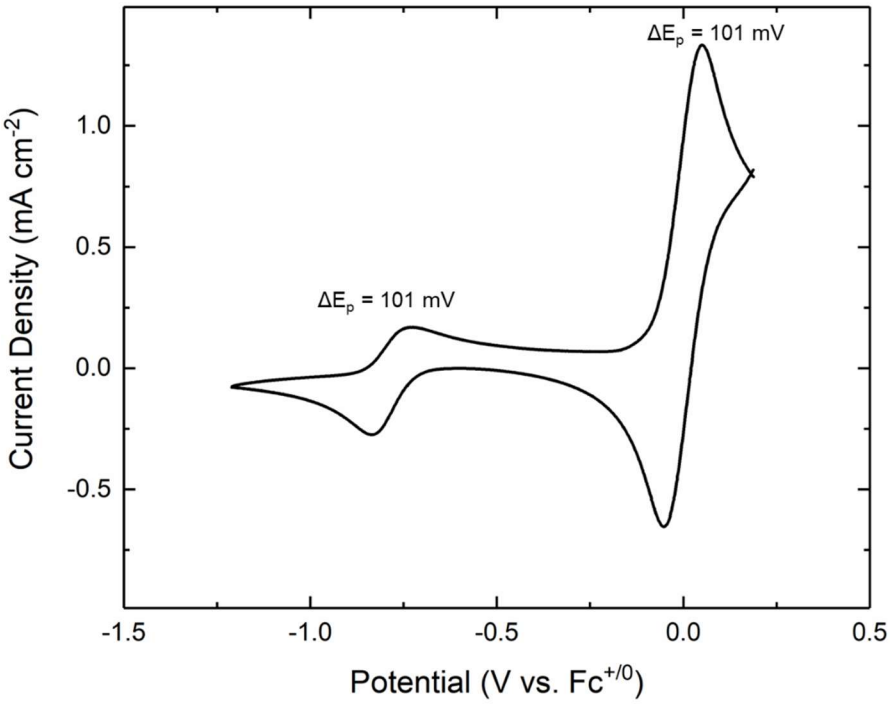

Figure 1.12: Cyclic voltammetry of **2** with ferrocene. Electrolyte: 0.1 M $TBAPF_6$ in CH_3CN, scan rate: 100 mV/s, electrode: highly oriented pyrolytic graphite. The initial potential of the voltammogram is at ca. –1.2 V. The second cycle of voltammetry is shown here.

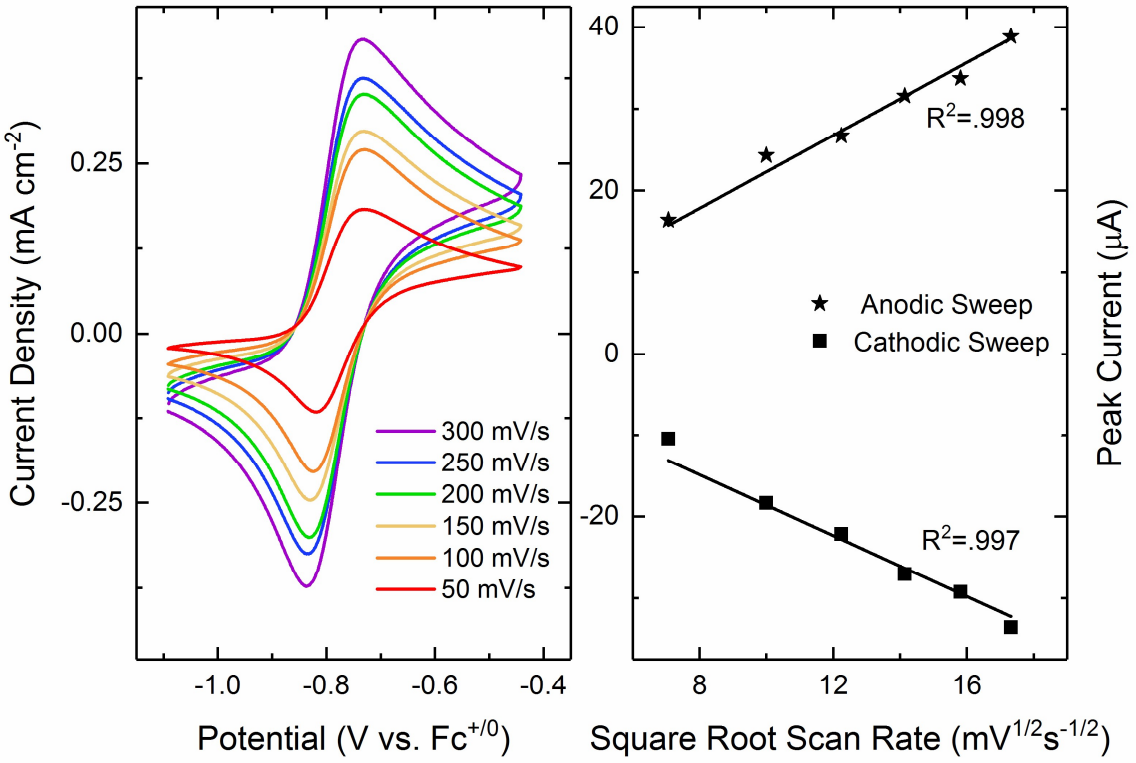

Figure 1.13: Left: cyclic voltammetry of **2** at varying scan rate in MeCN (0.1 M [^{n}Bu$_4$N][PF$_6$]). Right: linear dependence of peak current on square root of scan rate with the y-intercept set to 0.

Synthesis and spectroscopic characterization of [Cp*Rh^{III}(dppb)H][OTf] (3)

With **2** in hand, we explored the possibility of generating a hydride species by treatment of **2** with acid. For the analogous Cp*Rh(bpy) system, treatment with triethylammonium bromide (pK_a = 18.6 in CH_3CN) results in generation of the isolable (Cp*H)Rh(bpy)Br complex.[19] However, as **2** has a more positive reduction potential than Cp*Rh(bpy), we targeted the stronger acid anilinium triflate (pK_a = 10.6 in MeCN[66]) for generation of a singly-protonated complex.[42] Treatment of **2** in CH_3CN with 1.0 equiv. of anilinium triflate in thawing THF results in a visible lightening of the solution to lemon yellow without formation of a detectable precipitate. Following work up, ^{1}H NMR reveals a distinctive new signal at –11.8 ppm consistent with formation of a metal hydride species (Figure 1.14). This signal appears as a quartet (rather than the expected doublet of triplets

or triplet of doublets) due to an apparent coincidental similarity in the H,Rh and H,P coupling constants (i.e., $^{1}J_{H,Rh} \approx {}^{2}J_{H,P} \approx 29$ Hz). Importantly, whereas proton transfer to [Cp*] in $[(Cp^*H)Rh(bpy)]^+$ results in three inequivalent methyl resonances in its ^{1}H NMR spectrum (a doublet and two singlets are observed),[17,18] a single resonance for the [Cp*] protons is present in data for **3** at 1.58 ppm (Figure 1.14), excluding the possibility of generation of any [Cp*H] species or free pentamethylcyclopentadiene. The Cp* signal appears as a triplet of doublets, where splitting to the two equivalent phosphorus atoms ($^{4}J_{H,P} = 2.9$ Hz) gives rise to a triplet as in complexes **1** and **2** while the new $I = ½$ hydride nucleus leads to further splitting of each triplet peak into doublets ($^{4}J_{H,H} = 1.2$ Hz). The peaks in the aromatic region of **3** integrate to a total of 24 protons as expected for the dppb ligand, but significant signal overlap precludes full assignment of the spectra.

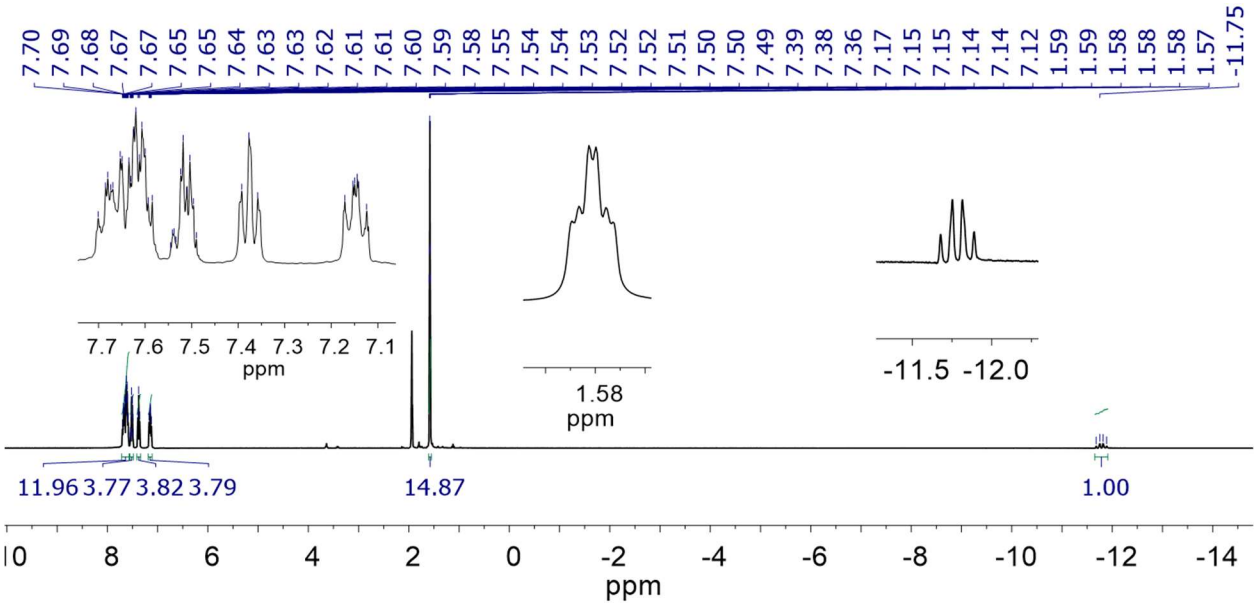

Figure 1.14: ^{1}H NMR spectrum (CD_3CN, 500 MHz) of **3**.

Unsurprisingly given their shared C_s symmetry, the $^{13}C\{^{1}H\}$ spectrum of **3** (Figure 1.15) has a qualitatively similar profile to complex **1** (Figure 1.4). The Cp* methyl carbons appear as a singlet

at 8.16 ppm, while coupling to rhodium, phosphorus, and perhaps even the hydride gives the Cp* ring carbons a complicated multiplet splitting at 101.57 ppm. As in **1**, the aromatic region shows four sharp triplets with $J \approx 6$ Hz that can likely be assigned to the *ortho* and *meta* positions on the sets of "up" and "down" dppb phenyl groups. Similarly, the weakly split triplets ($J = 1.4$ Hz) at 131.00 and 130.78 ppm are reminiscent of the peak shape of the *para* phenyl carbons in **2**. By similar analogy to **2**, comparison of the coupling constants for the triplets at 130.48 ppm and 131.16 ppm ($J = 9.2$ Hz and $J = 2.5$ Hz, respectively) suggests that the signal with larger splitting corresponds to the carbons adjacent to the phosphorus substituents on the benzene backbone, leaving the narrower triplet as the benzyl carbons separated from the phosphorus atoms by three bonds. The three aromatic quaternary carbon signals could not be located and are likely obscured by the more intense aromatic peaks.

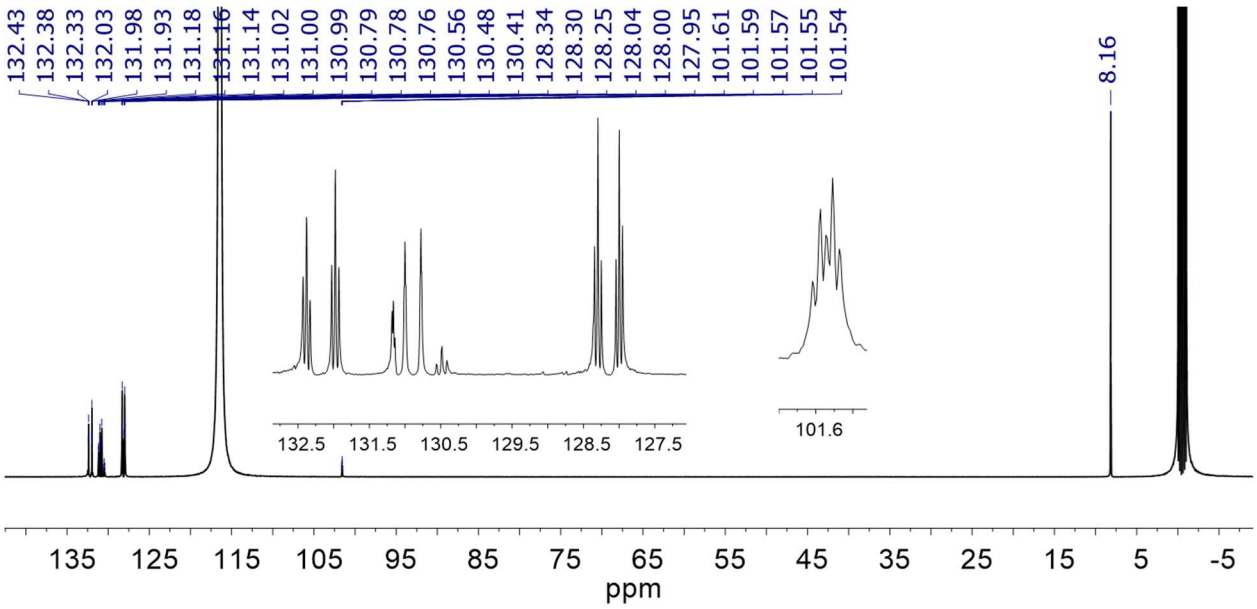

Figure 1.15: $^{13}C\{^{1}H\}$ NMR spectrum (CD_3CN, 126 MHz) of **3**.

The $^{31}P\{^{1}H\}$ spectrum of **3** (lower panel of Figure 1.5) also confirms formation of a new complex; a lone doublet is observed at 67.9 ppm with $^{1}J_{P,Rh}$ = 138 Hz. The magnitude of the coupling constant is consistent with a rhodium(III) species (compare to $^{1}J_{P,Rh}$ = 131 Hz in Rh(III) **1** and $^{1}J_{P,Rh}$ = 220 Hz in Rh(I) **2**). In accord with all these data, the infrared spectrum of **3** shows a distinctive [Rh–H] stretch at 1986 cm^{-1} (Figure 1.16) that is absent in the spectrum of **2**.

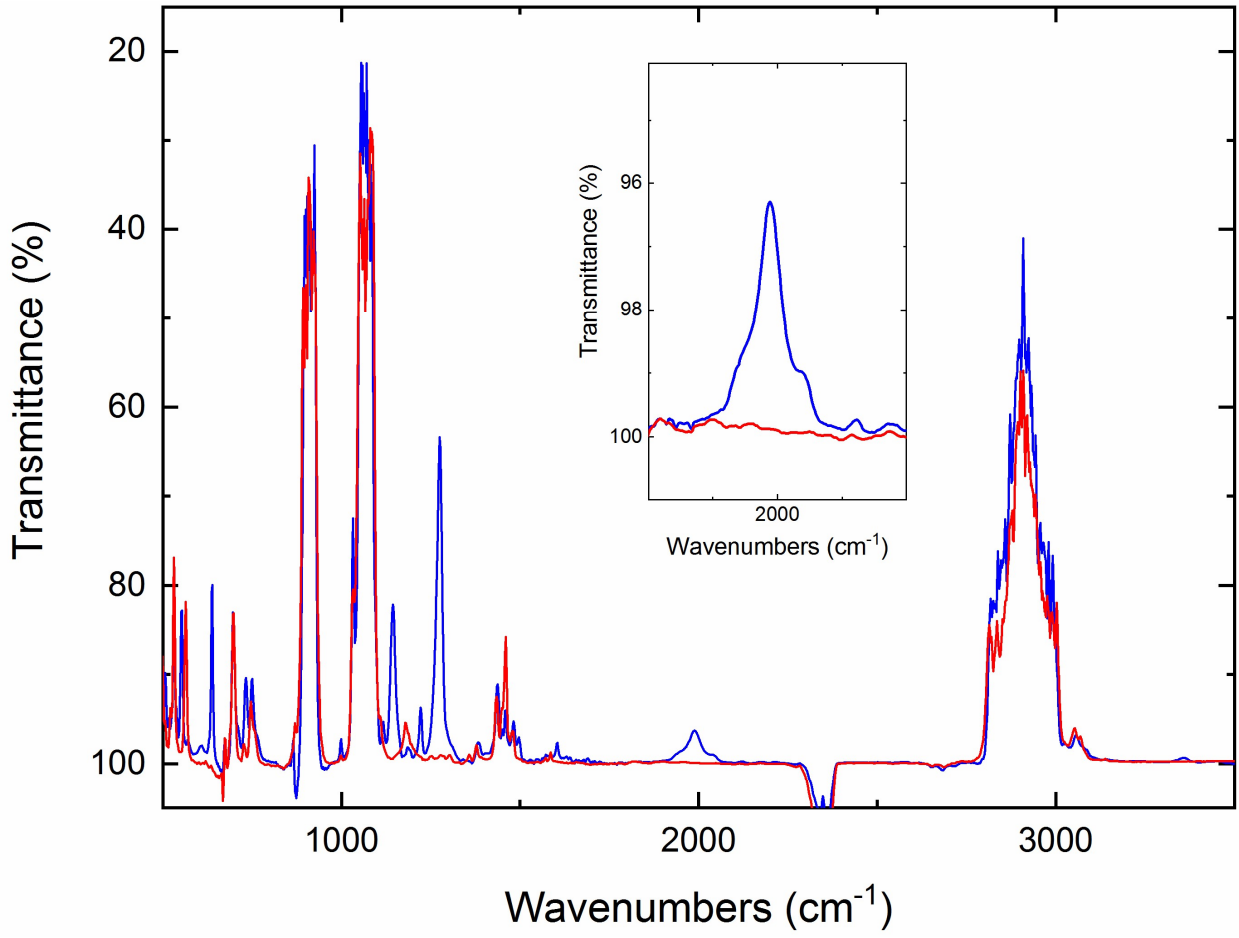

Figure 1.16: IR spectra of **2** (red) and **3** (blue) in THF. The inset highlights the Rh–H stretch at 1986 cm^{-1}.

Vapor diffusion of diethyl ether into a concentrated solution of **3** in THF yielded small light-yellow crystals suitable for XRD studies (see Appendix 3 for full crystallographic information). The geometry at the formally rhodium(III) metal center is again pseudo-octahedral, with dppb

retained in the κ^2 mode and [Cp*] bound in the typical η^5 mode (Figure 1.17). [Cp*] is planar, indicating that it retains its aromatic nature and no [Cp*H] material has formed. Gratifyingly, the hydride ligand (H17) was located in the Fourier difference map, and its position was freely refined. H17 is bound to the rhodium center, confirming the generation of a metal hydride moiety. The data provide an estimated Rh–H17 bond distance of 1.76(7) Å. However, the large amount of electron density associated with the rhodium center could lead to underestimation of this bond distance and thus this apparent bond length should not be interpreted any further.[43]

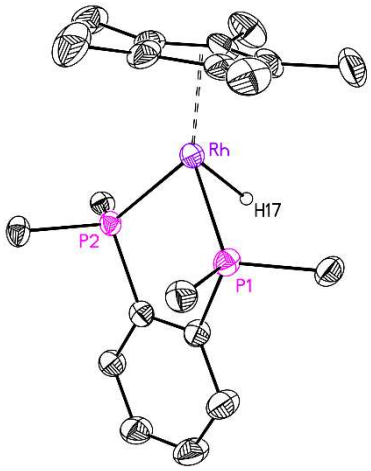

Figure 1.17: Crystal structure of **3**. All H atoms not bound to Rh, outer-sphere triflate counteranion, and terminal phenyl groups omitted for clarity.

Chemical properties of the [Cp*Rh] Hydride (3).

Use of eq. 12 in Scheme 1.4 to calculate the thermodynamic driving force of hydrogen evolution with **2** ($E^o_1 = E^o_2 = -0.78$ V) and $[DMFH]^+$ ($pK_a = 6.1$ in CH_3CN[6]) reveals that the reaction would be substantially exergonic, with $\Delta G^o_{HER} = -15.6$ kcal mol^{-1}, in good agreement with calculation of the difference between the estimated thermodynamic potential required for H_2 evolution with $[DMFH]^+[OTf]^-$ ($E^{o\prime}(H^+/H_2) = -0.389$ V)[40] and the reducing power of the

Cp*Rh(dppb) complex ($E_{1/2}(Rh^{III}/Rh^{I})$ = –0.78 V) to obtain an overpotential of ca. 17 kcal mol^{-1}.[44,45,46] While the previously studied Cp*Rh(diimine) complexes are more potent reducing agents ($E_{1/2}(Rh^{III}/Rh^{II})$ = –1.05, $E_{1/2}(Rh^{III}/Rh^{II})$ = –1.03 V) than **2**, the driving force for H_2 evolution from **2** with $[DMFH]^+$ as acid is essentially equivalent to that for H_2 evolution from Cp*Rh(bpy) with anilinium (pK_a = 10.6 in CH_3CN[6], ΔG^o_{HER} = –15.3 kcal mol^{-1}) as proton source. So, thermodynamically, the net reaction (5) should be equally spontaneous in the dppb and bpy systems when the H^+ source is adjusted to account for differences in reduction potential.

$[Rh^{I}] \rightleftharpoons [Rh^{II}]^+ + e^-$	$\Delta G^o = 23.06(E^o_1)$ kcal mol^{-1}	(8)
$[Rh^{II}]^+ \rightleftharpoons [Rh^{III}]^{2+} + e^-$	$\Delta G^o = 23.06(E^o_2)$ kcal mol^{-1}	(9)
$2\ B–H \rightleftharpoons 2\ B^- + 2H^+$	$\Delta G^o = 2(1.37)(pK_{a,acid})$ kcal mol^{-1}	(10)
$2H^+ + 2e^- \rightleftharpoons H_2$	$\Delta G^o = 3.6$ kcal mol^{-1}	(11)
$[Rh^{I}] + 2\ B–H \rightleftharpoons [Rh^{III}] + 2\ B^- + H_2$	$\Delta G^o_{HER} = 23.06\ (E^o_1 + E^o_2) + 2.74\ pK_{a,acid} + 3.6$ kcal mol^{-1}	(12)

Scheme 1.4: Derivation of thermodynamic driving force for H_2 evolution with $[Rh^{I}]$ and a proton source (ΔG^o_{HER}).[3]

Indeed, as discussed above, treatment of the isolated protonated species $[(Cp^*H)Rh(bpy)]^+$ with anilinium results in rapid generation of H_2 concurrent with a color change indicative of consumption of the Rh(I) species and generation of $[Cp^*Rh(bpy)]^{2+}$.[19] In the case of **3**, however, addition of $[DMFH]^+[OTf]^-$ does not lead to any detectable reactivity over 48 h as determined by ^{1}H NMR spectroscopy (Figure 1.18). Heating such a sample at 50°C overnight also does not lead to reactivity. This indicates that in the first protonation step of the overall reaction (eq. 12), the dppb complex **2** must be trapped at the inert rhodium-hydride **3** which prevents further reaction with protons. Storage of the first H^+ equivalent on the [Cp*] ring, evidently enabled by bpy but disfavored by dppb, appears to promote further reaction with H^+ to generate H_2.

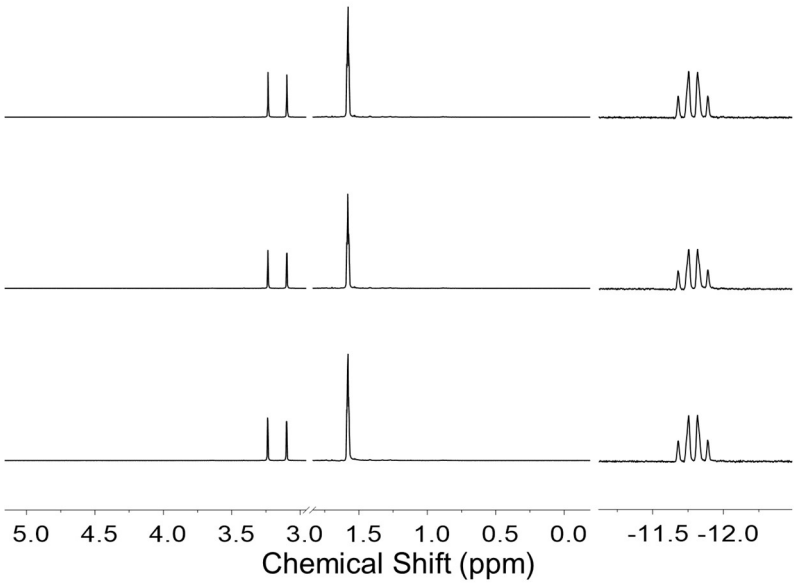

Figure 1.18: Partial ^{1}H NMR spectra of a 1:1 mixture of **3** and [DMFH][OTf] in CD_3CN after 15 min (lower panel), 24 hrs (middle), and 48 hrs (upper).

It is important to emphasize that the diametrically opposed results of reactivity studies with the bpy and dppb [Cp*Rh] systems do not imply that protonation at the Cp* ligand is required for hydrogen evolution while formation of a rhodium hydride eliminates it, or that the [Cp*H] complex is truly a catalytic intermediate. In fact, partial formation of Rh–H species is observed with diimine-based complexes by ^{1}H NMR spectroscopy. Specifically, we observe minor hydride signals *in situ* when we treat Rh(I) starting materials (e.g., Cp*Rh(^{R}bpy), ^{R}bpy = 4,4'-R_2-bpy, R = ^{t}Bu, H, CF_3), both competent H_2 evolution catalysts at their respective Rh(III/I) couples, with $[C_6H_5NH_3]^+$ (anilinium, pK_a = 10.6 in CH_3CN[6]) as proton source; upfield resonances around –9 ppm (see Figure 1.19) are indicative of Rh–H moieties. These signals are similar to those in prior reports of a hydride detected at low temperature[17] and another under aqueous conditions.[14] On the other hand, protonation of the Rh(I) complex supported by ^{CF3}bpy does not give rise to any detectable hydride species. This system is also a poor catalyst at the potential of its Rh(III/I) couple,

and only displays appreciable catalysis upon further reduction.[7] In the present system supported by the dppb ligand, hydride complex **3** is the only product of protonation of the corresponding Rh(I) species **2** (i.e., no (Cp*H)-containing species are observed) and the system is not a catalyst for H_2 evolution. Notably, the two sets of complexes that display a single product upon protonation (^{CF3}bpy and dppb) also display attenuated (or completely absent) catalysis at their respective Rh(III/I) couples. These observations are in good agreement with the results of computational studies on the mechanism of proton transfer in these systems, which implicated acid-dependent mechanisms of H_2 evolution via intermediates in which the first H^+ equivalent delivered "bridges" between the metal center and the [Cp*] ring.[21]

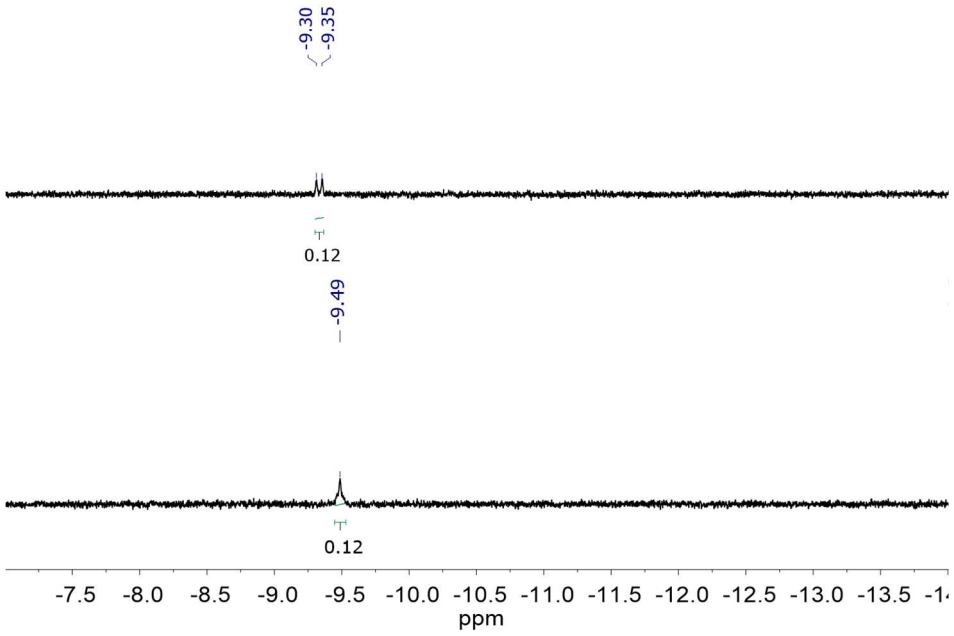

Figure 1.19: Upfield region of the ^{1}H NMR spectrum (400 MHz, CD_3CN) of [(Cp*H)Rh(^{R}bpy)][OTf] generated *in situ* with anilinium triflate (R=^{t}Bu (lower panel), H (upper panel)).

If the ability of the protonated species to access "bridging" states between the [(Cp*H)Rh] and [Rh–H] extremes is indeed the key to promoting catalytic behavior, then excessive stabilization of either motif ([(Cp*H)Rh] by ^{CF3}bpy, [Rh–H] by dppb) introduces a barrier to further reactivity that

cannot be overcome under the conditions studied. By tuning the basicity at the Cp* ligand and the rhodium center as well as by modulating the electron density at the metal, the properties of the supporting bidentate ligands (bpy, dppb) play a key role in affecting how tightly the $1H^+$ and $2e^-$ necessary to evolve H_2 with exogenous acid are bound to either the metal center or the Cp* ligand. The stark contrast between the robust catalysis of select Cp*Rh(diimine) complexes and the inertness of Cp*Rh(dppb) toward H_2 evolution suggests that a design rule for catalysis of small-molecule transformations with [Cp*Rh] complexes could be a requirement for enabling access to both [Cp*H] intermediates and Rh–H complexes rather than strong stabilization of one of these forms over the other. Further discernment of the thermochemical parameters and kinetic barriers involved in evolution of H_2 from [Cp*Rh] complexes bearing diphosphine and diimine ligands thus remains of interest and will be discussed later in this chapter.

Electrochemical properties of the [Cp*Rh] Hydride (3)

Having observed that **3** does not react even with strong acids, we were interested in the electrochemical properties of this apparently stable compound. Initially, we moved to confirm that there is no electrocatalytic generation of H_2 driven by formation of the Rh^{III}–H species (**3**). For example, addition of $[C_6H_5NH_3][OTf]$ to an electrochemical cell containing **1** results in loss of reversibility for the $2e^-$ wave observed by cyclic voltammetry and growth of a new feature at negative potentials (Figure 1.20, left panel, light and dark blue traces). This is consistent with generation of the hydride species **3** in a chemical reaction between electrochemically generated **2** and H^+. However, there is no catalytic enhancement above the electrode background in these studies at relevant potentials, even in the presence of excess acid; the profile of a solution of **1** with 5 equiv. acid (resulting in a solution of **3** with 4 equiv. acid after consumption of 1 equiv. acid after

reduction of **1** to **2** and subsequent protonation) is virtually identical to a solution of 4 equiv. acid, as depicted in the right panel of Figure 1.20. This result contrasts with prior work on Cp*Rh(diimine) complexes under similar conditions.[7]

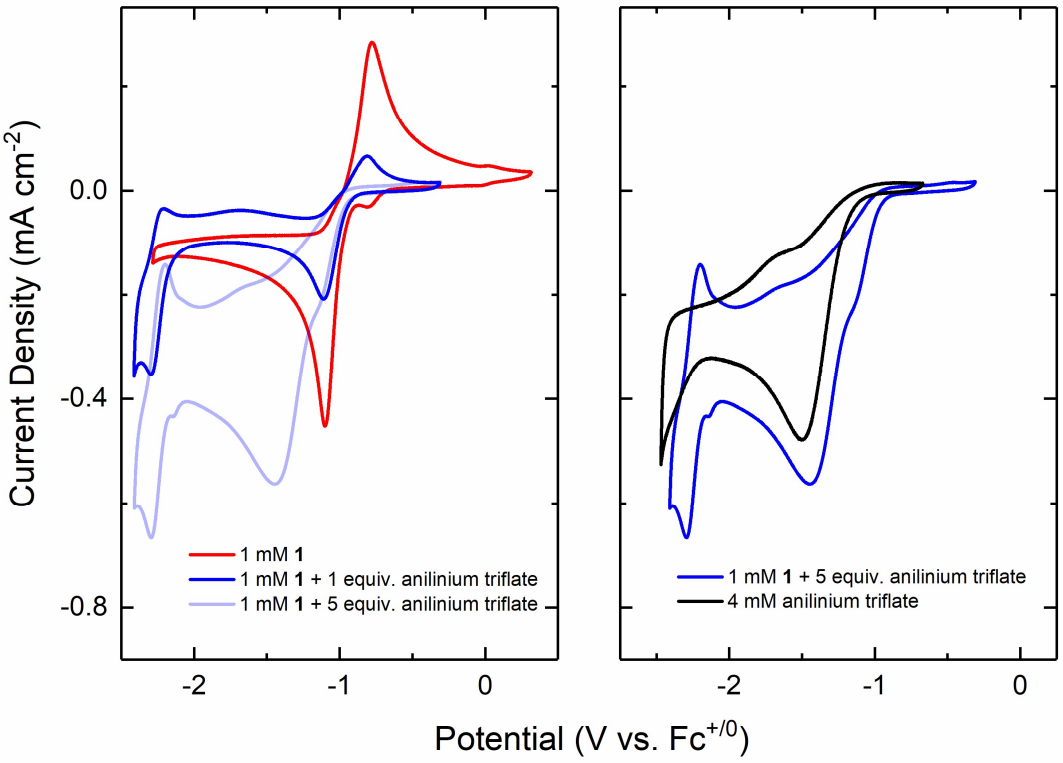

Figure 1.20: Left: cyclic voltammetry of **1** (1 mM) with additions of anilinium triflate. Right: cyclic voltammetry of **1** (1 mM) with 5 equiv. anilinium triflate compared to a blank of the acid (4 mM). Electrolyte: 0.1 M $TBAPF_6$ in CH_3CN, scan rate: 100 mV/s, electrode: highly oriented pyrolytic graphite. The second cycle of voltammetry is shown here.

However, interrogation of isolated **3** suggests that further reduction of the hydride complex is possible. In the CV of isolated **3**, a similar cathodic wave observed to that arising from *in situ* generation of **3** in Figure 1.20 is observed at –2.34 V vs. $Fc^{+/0}$, near the limit of polarization for our conditions (Figure 1.21). A small corresponding anodic wave is observed at –2.24 V, suggesting that the electrochemical reduction of **3** is followed by a chemical reaction (in an EC-

type process). In accord with this theory, increasing the voltammetric scan rate (Figure 1.22) results in improved electrochemical reversibility, and suggests an approximate midpoint potential for $1e^-$ reduction of **3** near –2.29 V. The peak current for the reduction event varies linearly with the square root of scan rate, in accord with the soluble and freely diffusing nature of **3** (Figure 1.22). A new anodic wave, absent prior to electrochemical reduction of **3**, appears at $E_{p,c}$ = –0.73 V after these cathodic scans (Figures 1.21 and 1.23). The potential for this new process is consistent with that for oxidation of the Rh(I) complex **2** to the corresponding solvento Rh(III) species (Figure 1.21, red scan); this observation suggests that reduction of **3** leads to at least partial loss of the hydride ligand and concomitant regeneration of the non-protonated rhodium(I) species **2**.

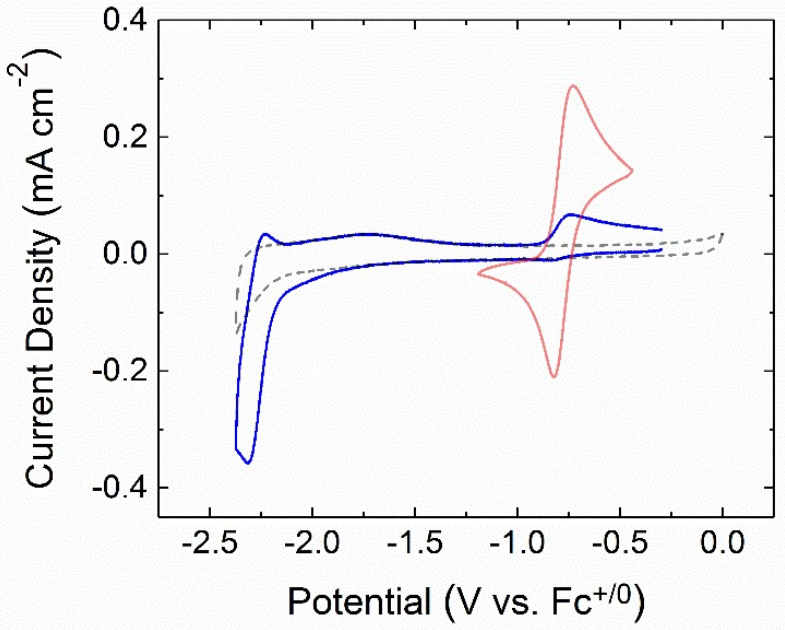

Figure 1.21: Cyclic voltammetry of **2** (red, 1 mM), **3** (blue, 1 mM), and a blank (dashed). Electrolyte: 0.1 M $TBAPF_6$ in MeCN, scan rate: 100 mV/s, electrode: highly oriented pyrolytic graphite. The initial potentials of the voltammograms are as follows: for **2**, –1.2 V; for **3**, –0.30 V; for the blank, 0 V.

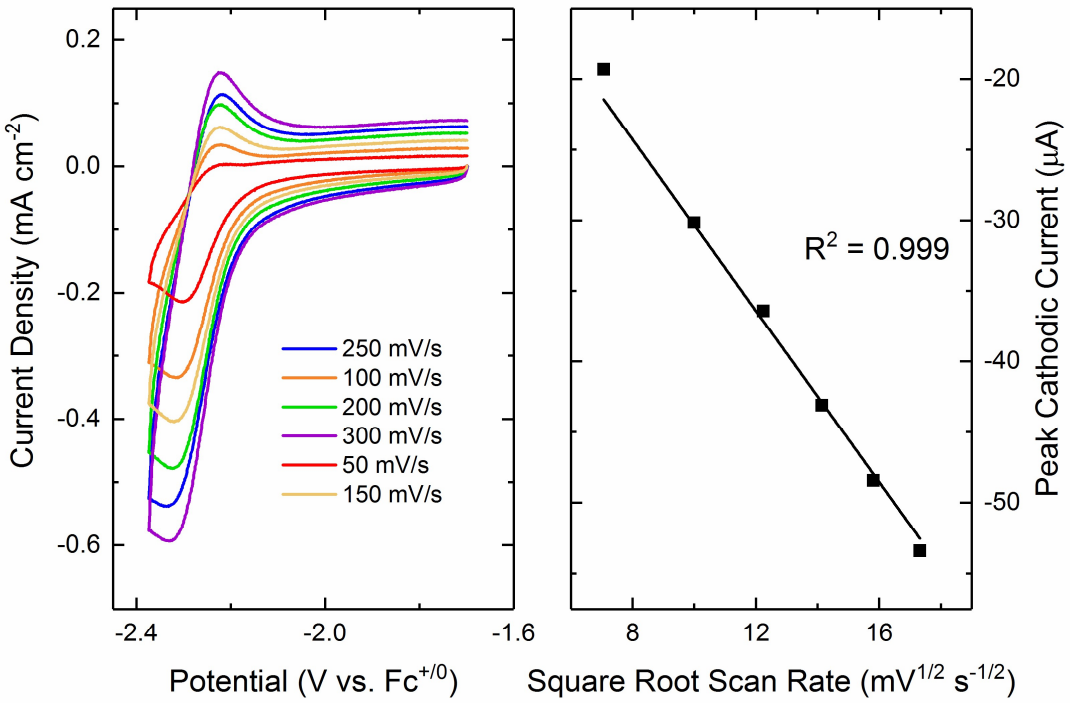

Figure 1.22: Left: cyclic voltammetry of **3** at varying scan rate in MeCN (0.1 M [^{n}Bu$_4$N][PF$_6$]). Right: linear dependence of peak cathodic current on square root of scan rate with the y-intercept set to 0.

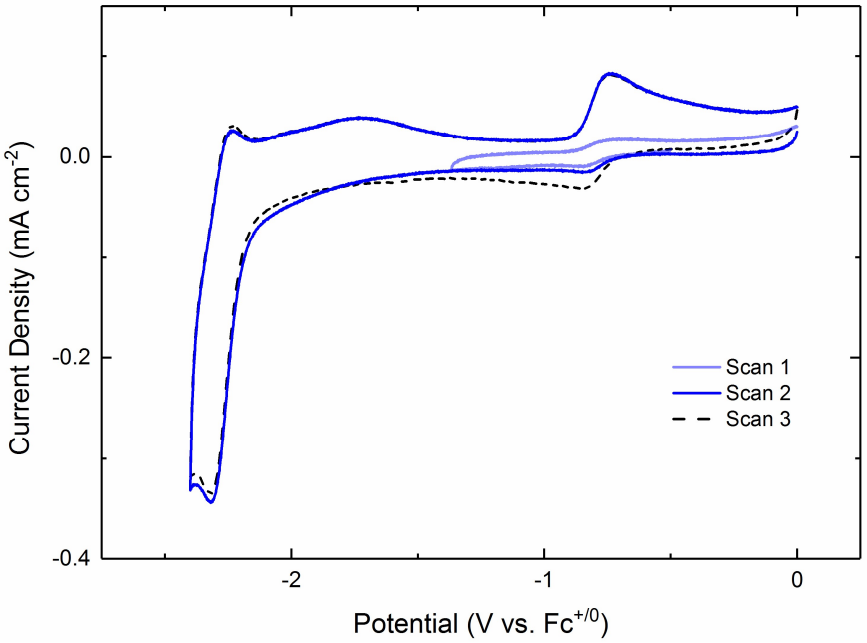

Figure 1.23: Multiple scans of cyclic voltammetry of **3**. Electrolyte: 0.1 M $TBAPF_6$ in MeCN, scan rate: 100 mV/s, electrode: highly oriented pyrolytic graphite. The initial potential of the voltammogram is 0 V.

These results are reminiscent of the observation of a $1e^-$ reduction event ($E_{p,c}$ = –1.45 V) in the CV of $[(Cp^*H)Rh(^{CF3}bpy)]^{2+}$ (^{CF3}bpy = 4,4'-di(trifluromethyl)-2,2'bipyridine).[7] Reduction of this species can lead to generation of H_2 (0.5 equiv per Rh complex) and formation of $Cp^*Rh(^{CF3}bpy)$, consistent with net formal loss of a hydrogen atom (H•). An analogous reduction was observed in [(Cp*H)Rh(bpy)Br] ($E_{p,c}$ = –1.73 V) and leads to a similar H_2 evolution pathway; chemical reactivity and bulk electrolysis experiments confirmed generation of Cp*Rh(bpy) and H_2 upon $1e^-$ reduction of [(Cp*H)Rh(bpy)Br].[19] Thus, we propose that reduction of **3** leads to release of H_2 and regeneration of Rh(I) complex **2**, according to the following equation (eq. 9):

$$2[Cp^*Rh(dppb)H]^+ + 2e^- \rightarrow H_2 + 2Cp^*Rh(dppb) \quad (13)$$

To test this hypothesis, we targeted both bulk electrolysis and chemical reduction experiments to determine the products of reduction of **3**. Controlled potential electrolysis of **3** was carried out

at –2.23 V vs. $Fc^{+/0}$ (Figure 1.24) for 1.1 h; headspace analysis by gas chromatography (GC) revealed the presence of H_2 with a 58% Faradaic yield. The primary metal-containing product of the electrolysis was identified as **2** via UV-visible spectroscopy (see Figure 1.25). Similarly, treatment of **3** with 1 equiv of sodium naphthalenide ($Na[C_8H_{10}]$, $E° = –3.10$ V)[40] results in a color change from light yellow to dark red in seconds, suggesting generation of **2**. Headspace analysis by GC confirms generation of H_2 upon chemical reduction. Consistent with the electrochemical work, the primary metal-containing product of the reduction was identified as **2** via $^{31}P\{^1H\}$ NMR spectroscopy (Figure 1.26).

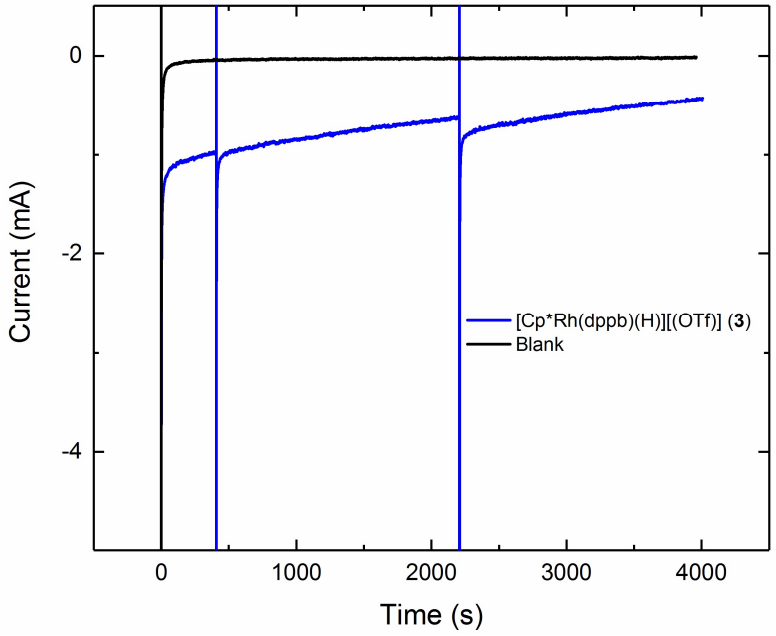

Figure 1.26: Current passed in bulk electrolyses at –2.282 V vs. $Fc^{+/0}$ of 1 mM **3** and a blank (0.1 M $[^nBu_4N][PF_6]$, 10 mM ferrocene). Spikes in the data for **3** correspond to pausing and restarting the electrolysis.

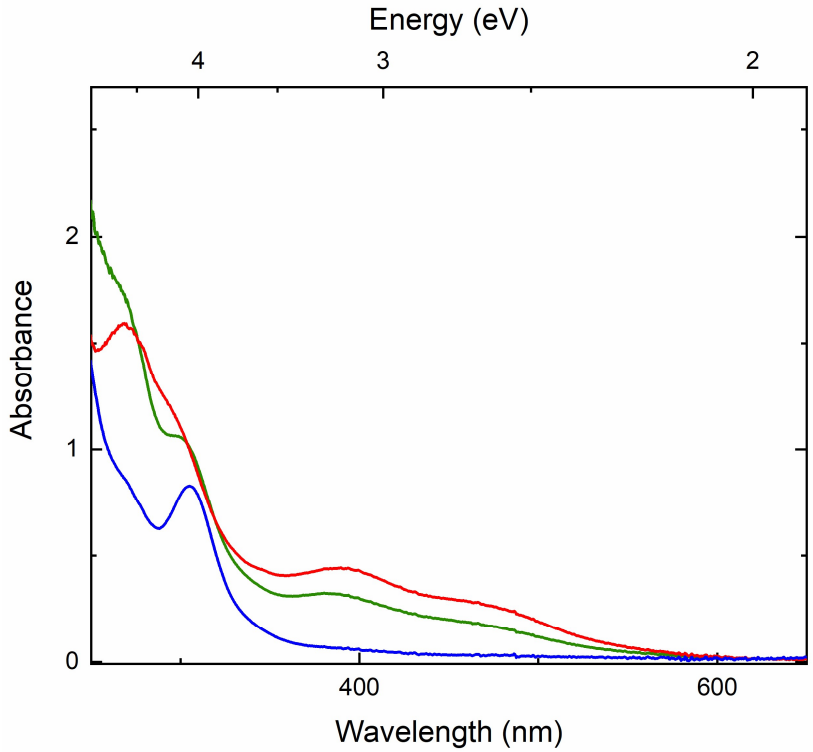

Figure 1.25: Electronic absorption spectra of **2** in THF (red), **3** in THF (blue), and an aliquot diluted 10-fold from bulk electrolysis of 1 mM **3** at –2.282 V vs. $Fc^{+/0}$ for 66 minutes (green). The spectrum indicates ~0.65 mM **2** in the bulk electrolysis aliquot, or 65% conversion of **3** to **2**.

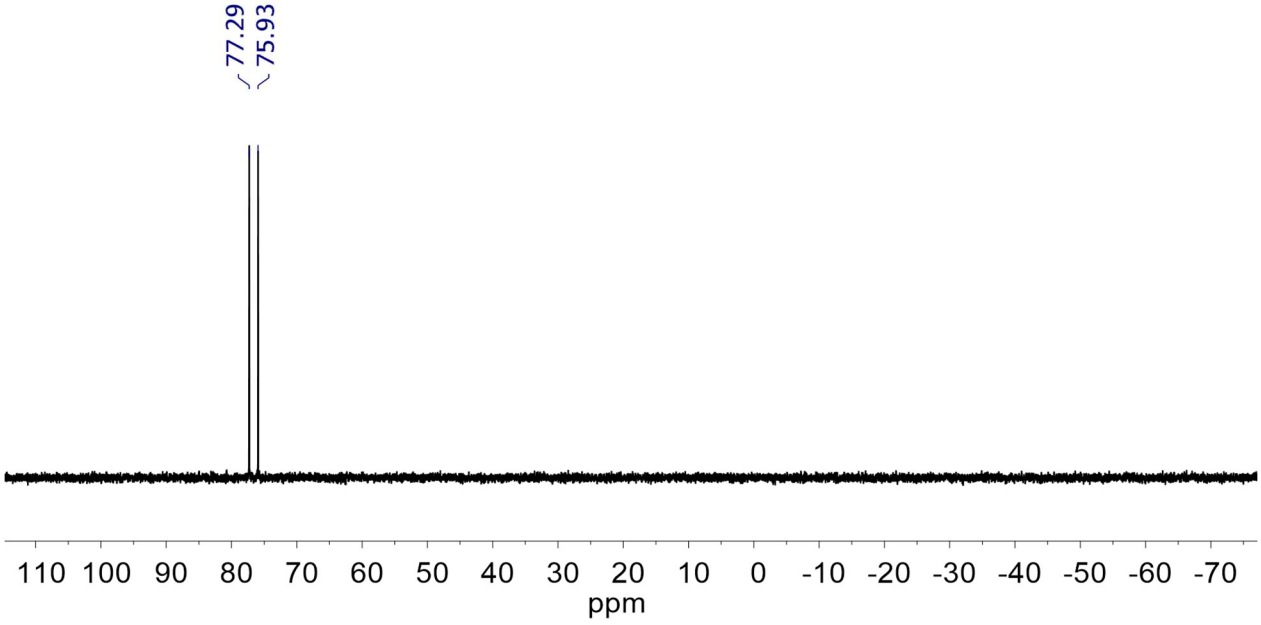

Figure 1.26: $^{31}P\{^{1}H\}$ NMR spectrum (162 MHz, C_6D_6) of an aliquot from chemical reduction of **3** with sodium naphthalenide.

Thus, despite the resistance of the Rh–H complex **3** to protonolysis, generation of H_2 from this complex can be achieved via $1e^-$ reduction (Figure 7). This process is analogous to the catalytic H_2 evolution that can be induced by reduction of [Cp*H] complexes supported by bpy[19] and ^{CF3}bpy,[7] as well as H_2 evolution mechanisms that have been demonstrated for cobaloximes,[47] $[Cp^*Ir(bpy)H]^+$,[48] and poly(bipyridyl) rhodium hydrides.[32] However, we note that the modest Faradaic yield of H_2 measured following electrolysis of **3** contrasts with the near unity yield encountered in our work with the bpy and ^{CF3}bpy complexes. We ascribe this diminished efficiency to side reactions that can occur under the extremely reducing conditions necessary for electrochemical activation of **3**. The reductions of the rhodium complexes bearing [Cp*H] are centered on the bpy ligands, due to the presence of low-lying, delocalized bpy π* orbitals. As a result, these processes occur at substantially more positive potentials (–1.73 and –1.45 V, respectively) than the reduction measured for **3** (–2.34 V).[49] As comparison, the free dppb ligand is reduced at a more negative potential,[50] while other metal complexes of dppb do not manifest ligand-centered reductions at relevant potentials.[51,52] Moreover, the related $[Cp^*Rh(bpy)Me]^+$ complex undergoes both quasi-reversible diimine-centered reduction ($E_{1/2}$ = –1.78 V) and metal-centered reduction ($E_{p,c}$ = –2.22 V), as demonstrated by chemical and spectroscopic studies.[38] Thus, we propose that the reduction of **3** is likely to be metal-centered, leading to generation of a reactive (transient) Rh^{II}–H complex that could undergo Rh–H bond homolysis or protonolysis by an exogenous H^+ source. The notion of a transient Rh^{II} complex is consistent with the appearance of a small anodic wave ($E_{p,a}$ = –2.24 V) coupled to reduction of **3** (see Figure 1.21). This coupled anodic feature is most pronounced in the presence of excess acid (Figure 1.20), consistent with continuous reprotonation of **2** to generate **3** after the hydrogen evolution reaction of reduced **3**.

Thermochemical Basis for Reactivity Modes of 3

Scheme 1.5 summarizes the reactivity (and lack thereof) of the [Cp*Rh] monohydride **3** described thus far, which is directly complementary to that observed for analogous Cp*Rh(diimine) complexes. While protonation of Cp*Rh(bpy) with triethylammonium yields the ligand-protonated species [(Cp*H)Rh(bpy)][OTf], an identical protonation reaction with Cp*Rh(dppb) gives the rhodium hydride species **3**. The hydride species is inert to further reaction with protons, whereas the [Cp*H] complex reacts readily with $[DMFH]^+$ (pK_a = 6.1 in CH_3CN[6]) to generate hydrogen. Because the $[Cp^*Rh^I]$ complexes of dppb and bpy are both thermodynamically capable of reacting with an acid as strong as $[DMFH]^+$, we infer that the rhodium(III) hydride supported by dppb impedes the hydrogen evolution reactivity that the diimine [Cp*H] complexes promote. It could do so either kinetically (i.e., the activation barrier for hydrogen evolution with the hydride species is markedly higher than with the [Cp*H] species) or thermodynamically (i.e., the net free energy change for hydrogen evolution from the rhodium hydride is positive while that from the [Cp*H] complex is negative). Given the stability of the hydride complex at elevated temperature (50°C) over several days, we postulated that thermodynamics play the definitive role here. We therefore set out to obtain quantitative thermodynamic data that might illuminate the source of the divergent reactivity with protons of the otherwise analogous [Cp*Rh(diimine)] and [Cp*Rh(dppb)] series.

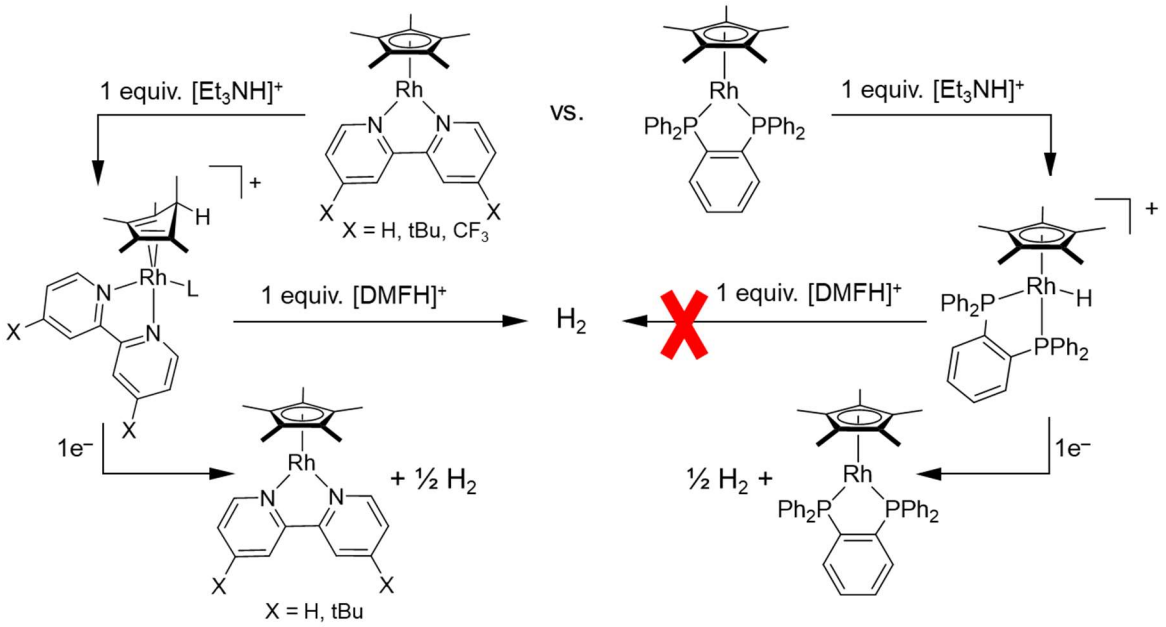

Scheme 1.5: Comparison between H_2 evolution chemistry on the Cp*Rh(dppb) and Cp*Rh(bpy) platforms.

Thermodynamic square schemes are useful tools for evaluation of various thermochemical parameters as insight into mechanisms of chemical processes. In the generalized square scheme in Figure 1.27, vertical (red) reactions represent electron transfer (ET) steps, while horizontal (blue) reactions represent proton transfer (PT) steps. The ET and PT pathways on each side of a square are thermodynamically equivalent to transfer of H•, represented by the diagonal (blue) reactions. The free energy change associated with net loss of a hydrogen atom is formally equal to the bond dissociation free energy (*BDFE*), and can therefore be derived from the free energies of the individual PT/ET steps in the Bordwell equation for CH_3CN (eq. 14).[45,53-57,,,,] Similarly, the green curved arrows cutting across two tiers in Figure 1.27 correspond to net loss of a hydride (H^-), which is thermodynamically equivalent to loss of H^+ and $2e^-$, allowing the free energy of hydride transfer (referred to as "hydricity", ΔG^{o}_{H-}) to be calculated from one pK_a and two reduction potentials using eq. 15.[3]

$$BDFE = 1.37\mathrm{p}K_a + 23.06E_{1/2} + 54.9 \quad (14)$$

$$\Delta G^{o}_{H-} = 1.37\mathrm{p}K_a + 23.06(E_{1/2} + E_{1/2}^{'}) + 79.6 \quad (15)$$

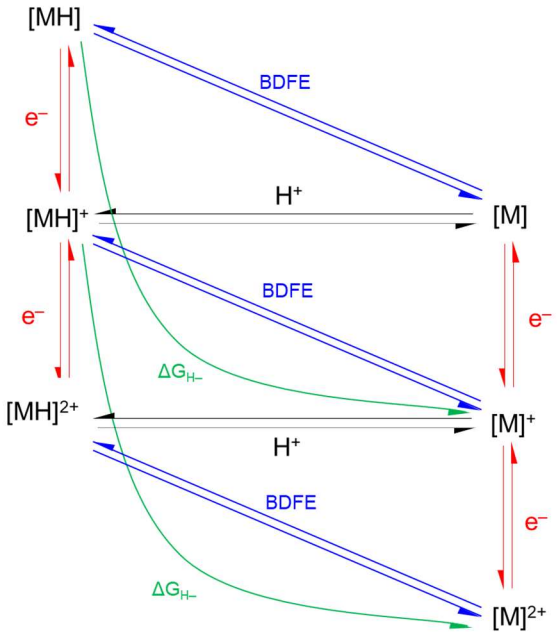

Figure 1.27: Thermochemical "square" scheme for determining *BDFE* and hydricity (ΔG_{H-}).

The reduction potentials for use in eqs. 14 and 15 were determined from cyclic voltammetry of complexes **2** and **3**. Data for the [Cp*Rh^{III}–Cl] species **1** was not considered, as the speciation arising from competing coordination between chloride anions and solvent molecules following oxidation complicates the thermodynamic relationships used to derive eqs. 14 and 15. Fortunately, **2** provides sufficient electrochemical information to complete the non-protonated side of the thermochemical diagram for this system (i.e., vertical processes on the right side of Figure 1.27). As discussed previously, the [Cp*Rh^{I}] species **2** (corresponding to [M] in Figure 1.27) undergoes a quasireversible net 2e$^-$ process centered at –0.78 V vs. Fc$^{+/0}$ which can be decomposed into two 1e$^-$ events where $E_{1/2}(\mathrm{Rh}^{II/I}) = E_{1/2}(\mathrm{Rh}^{III/II}) = -0.78$ V. Similarly, electrochemistry of the [Cp*Rh–H] **3** (i.e., [MH]$^+$ in Figure 1.27) provides approximate redox potentials for the two ET processes

on the left side of Figure 1.27. At fast scan rates, the 1e$^-$ reduction of **3** becomes quasireversible (Figure 1.22) with $E_{1/2}$ = –2.29 V vs. $Fc^{+/0}$.

The final piece of data required to unlock all of the thermodynamic values in Figure 1 is the pK_a of the $[Rh^{III}–H]^+$ **3**. To obtain this key value, triethylamine (pK_a of triethylammonium = 18.8 in CH_3CN[6]) was added to **3** and growth in of **2** was monitored by electronic absorption spectroscopy (see Figure 1.30). Based on the absorption of the resulting solution at 476 nm, where **2** absorbs intensely (ε = 2420 M^{-1} cm^{-1}, Figure 1.28) and **3** shows no absorption (Figure 1.29), the pK_a of **3** ([MH^+ in Figure 1.27) was determined to be 20.0 ± 0.1. Interestingly, this pK_a value is nearly identical to that of [(Cp*H)Rh(bpy)][OTf] (pK_a = 20.4 ± 0.1)[41] despite the differing locations of the relevant proton in each complex and the ca. 250 mV stronger reducing power of Cp*Rh(bpy) (the conjugate base of $[(Cp^*H)Rh(bpy)]^+$) compared Cp*Rh(dppb).

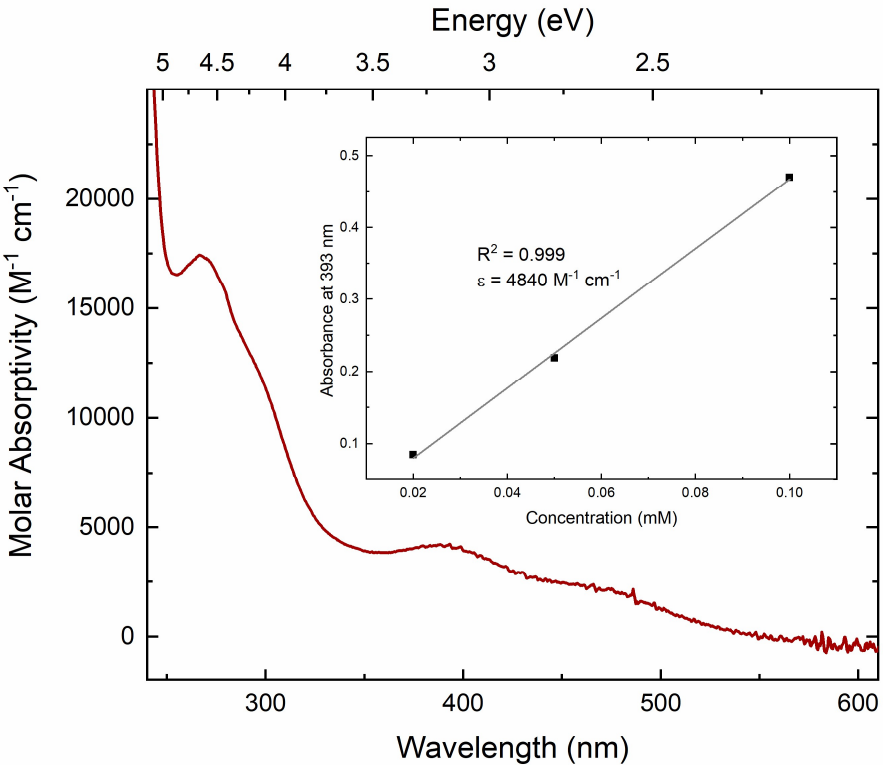

Figure 1.28: Electronic absorption spectrum of **2** in CH_3CN. The inset shows a plot of absorbance at 393 nm vs. concentration used to calculate molar absorptivity at this wavelength. A similar plot was generated at 476 nm for use in pK_a determinations.

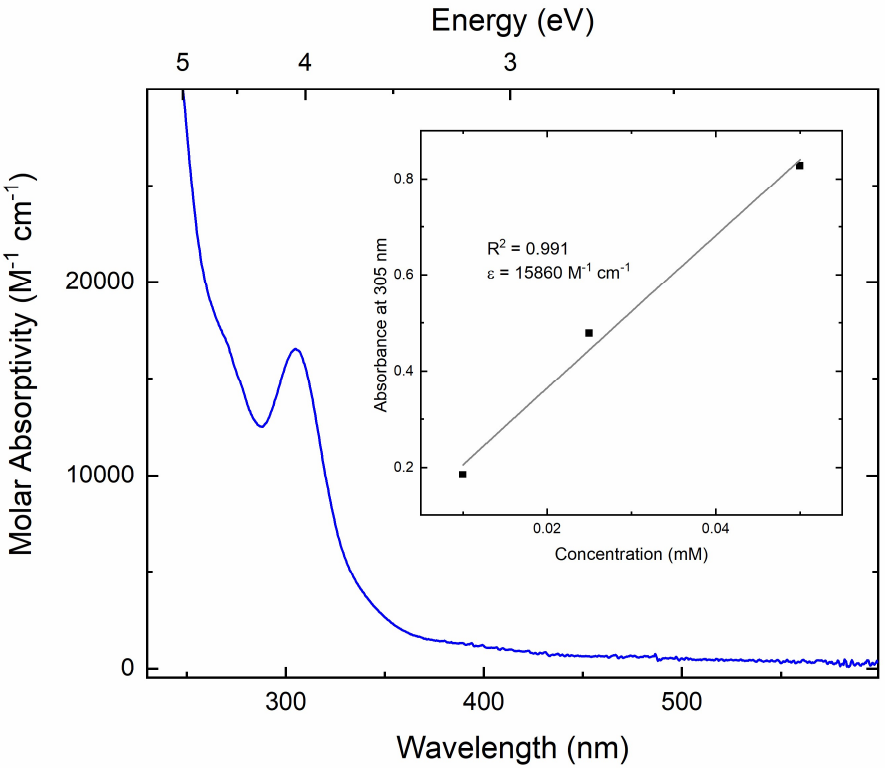

Figure 1.29: Electronic absorption spectrum of **3** in CH_3CN. The inset shows a plot of absorbance at 305 nm vs. concentration used to calculate molar absorptivity at this wavelength.

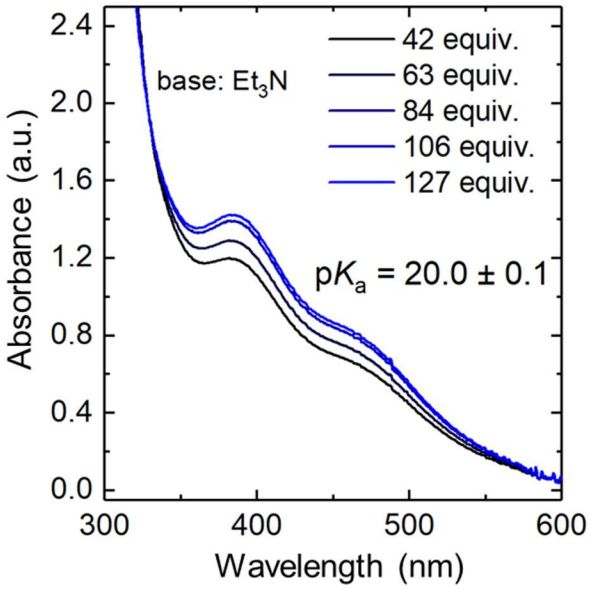

Figure 1.30: Electronic absorption data for addition of Et_3N to **3** in CH_3CN to determine pK_a. $[\mathbf{3}]_i$ = 0.34 mM.

With all of these values for the ET/PT steps in hand, we calculated *BDFE* and ΔG^{o}_{H-} for **3** as well as for its reduced form (i.e., $[MH]^+$ and [MH] in Figure 1.27). The results are summarized in Tables 1.1 and 1.2 along with comparison to analogous values from the bpy series.[41] As evidenced by the more positive *BDFE* and ΔG^{o}_{H-} values, in the oxidized form the dppb-supported rhodium-hydride is significantly stabilized relative to $[(Cp^*H)Rh(bpy)]^+$, fully consistent with the observed reactivity of these complexes. By contrast, the reduced form of **3** (**3**$^-$) is much less stable to loss of H• or H^- than the bpy analogue, due primarily to the much more negative reduction potential of **3**. The dramatic decrease in thermodynamic stability between **3** and **3**$^-$ correlates well with the enhanced hydrogen evolution reactivity upon chemical and electrochemical reduction of **3** in comparison to the complete lack of reactivity observed for the starting $[Rh^{III}–H]^+$ species.

Table 1.1: Thermochemical parameters for $[Cp^*Rh(H)(dppb)]^+$ (**3**) and $[(Cp^*H)Rh(bpy)]^+$.

L	$[MH]^+$ form	pK_a	$E_{1/2}([M]^{2+/+})^a$	$E_{1/2}([M]^{+/0})^a$	$BDFE^b$	$\Delta G^{o}_{H-}{}^b$
dppb	[Rh–H]	20.0	–0.78	–0.78	64.3	71.0
bpy	[Cp*H]	20.4	–1.05	–1.03	59.1	59.6

^{a} V vs. $Fc^{+/0}$. ^{b} kcal mol^{-1}.

Table 1.2: Thermochemical parameters for reduced forms of $[Cp^*Rh(H)(dppb)]^+$ (**3**$^-$) and $[(Cp^*H)Rh(bpy)]^+$.

Ligand	pK_a	$E_{1/2}([MH]^{+/0})^a$	$E_{1/2}([M]^{+/0})^a$	$BDFE^b$	$\Delta G^{o}_{H-}{}^b$
dppb	20.0	–2.29	–0.78	30.4	37.1
bpy	20.4	–1.74	–1.03	42.7	43.5

^{a} V vs. $Fc^{+/0}$. ^{b} kcal mol^{-1}.

It is important to note that the reported hydricity for **3** does not account for the solvent binding chemical step that occurs prior to the second oxidation of **2** (i.e., the chemical step in the ECE mechanism). A more rigorous equation for calculating hydricity in this system is shown in Scheme 1.6, in which an additional term corresponding to the equilibrium of solvent binding to a formally $[Rh^{II}]$ species is explicitly included. This extra term depends on the equilibrium constant (K_{eq}) for solvent binding to the 17e$^-$ $[Cp^*Rh^{II}(dppb)]^+$ complex generated from oxidation of **2** to form the 19e$^-$ solvento complex $[Cp^*Rh^{III}(NCCH_3)(dppb)]^{2+}$. While we have not experimentally measured

K_{eq}, simulations of the CV data of **2** produce an equilibrium constant of 0.05, which corresponds to a ΔG^o value of only 1.7 kcal mol^{-1} in eq. 18.[41] Moreover, any value for K_{eq} ranging from 0.01 – 100 corresponds to ΔG^o values of only ± 2.5 kcal mol^{-1}. In the dppb framework, the only value affected by this omission is the hydricity of **3** (and therefore the calculation of the driving force for heterolytic hydrogen evolution from this complex, *vide infra*). We therefore opted to omit solvent coordination thermodynamics from our determinations of the values in Tables 1.1-1.4.

$[Rh^{III}–H]^+ \rightleftharpoons [Rh^{I}] + H^+$	$\Delta G^o = 1.37(pK_a)$	(16)
$[Rh^{I}] \rightleftharpoons [Rh^{II}]^+ + e^-$	$\Delta G^o = 23.06(E_{1/2})$	(17)
$[Rh^{II}]^+ + CH_3CN \rightleftharpoons [Rh^{II}–NCCH_3]^+$	$\Delta G^o = –0.586(\ln K_{eq})$	(18)
$[Rh^{II}–NCCH_3]^+ \rightleftharpoons [Rh^{III}–NCCH_3]^{2+} + e^-$	$\Delta G^o = 23.06(E_{1/2}')$	(19)
$H^+ + 2e^- \rightleftharpoons H^-$	$\Delta G^o = 79.6$ kcal mol^{-1}	(20)
$[Rh^{III}–H]^+ + CH_3CN \rightleftharpoons H^- + [Rh^{III}–NCCH_3]^{2+}$	$\Delta G^o_{H–} = 1.37(pK_a) + 23.06(E_{1/2} + E_{1/2}') – 0.586(\ln K_{eq}) + 79.6$ kcal mol^{-1}	(21)

Scheme 1.6: Derivation of hydricity ($\Delta G^o_{H–}$) from a pK_a and two reduction potentials with a solvent coordination step explicitly included.

To fully quantify the observed reactivity differences between the diphosphine and diimine ligand systems, the *BDFE* and $\Delta G^o_{H–}$ values can be substituted into the expressions derived from the Hess cycles in Scheme 1.7 for the free energy of homolytic and heterolytic hydrogen evolution (eqs. 24 and 28). The resulting thermodynamic driving forces with a variety of acid sources for **3**, its reduced form, and the corresponding bpy complexes are summarized in Tables 1.3 and 1.4. Notably, all of the determined values align well with the previously discussed patterns in reactivity. Neither **3** nor $[(Cp^*H)Rh(bpy)]^+$ is thermodynamically capable of making H_2 homolytically, as is expected given our ability to isolate and store these protonated complexes. Furthermore, while reaction with anilinium or $[DMFH]^+$ is predicted to be spontaneous with the bpy-supported (Cp*H) complex, the hydricity of **3** is too high to react with any of the acids listed. In practice, we have shown that the (Cp*H) species is capable of catalytic hydrogen evolution with anilinium triflate as

well as facile reaction with $[DMFH]^+$ to liberate H_2;[19] **3**, on the other hand, is completely unreactive with either proton source. Thus, our initial hypothesis that the [Cp*Rh–H] complex ligated by dppb acts as a thermodynamic well in the reaction between $[Rh^I]$ and acid is supported by the thermochemical data. In fact, we can further elaborate this point by rearranging eq. 24 to solve for the pK_a required for the reaction to be spontaneous (eq. 25); for **3**, that pK_a is 3.6. In other words, only with an acid three orders of magnitude stronger than $[DMFH]^+$ is stabilization of the conjugate base a strong enough driving force to bring the free energy of the products of hydrogen evolution below that of the rhodium-hydride. Importantly, because the pK_a's of **3** and $[(Cp^*H)Rh(bpy)]^+$ are virtually identical, the only source of the stark contrast in hydricity values between the two complexes is the reduction potentials. So, thermodynamically, the sole impact of dppb on the catalytic ability of the [Cp*Rh] motif lies in its modulation of electron density at the metal center, making it more difficult to remove the $2e^-$ necessary to generate H_2 with a proton source. The design rule that emerges directly from this result is simply to synthesize catalysts that have electron-rich metal centers; however, as this route would only result in higher overpotentials, a more attractive strategy might be to target a ligand set that decreases the basicity at both the metal center and the Cp* ligand, perhaps allowing access to the bridging hydride-[Cp*H] sites discussed previously.

$$2[X–H] \rightleftharpoons 2H\bullet + 2X \qquad \Delta G^o = 2(BDFE_{X–H}) \qquad (22)$$

$$2H\bullet \rightleftharpoons H_2 \qquad \Delta G^o = -102.3 \text{ kcal mol}^{-1} \qquad (23)$$

$$2[X–H] \rightleftharpoons 2X + H_2 \qquad \Delta G^o_{HER} = 2(BDFE_{X–H}) - 102.3 \text{ kcal mol}^{-1} \qquad (24)$$

$$[X–H] \rightleftharpoons [X]^+ + H^- \qquad \Delta G^o = \Delta G^o_{H-} \qquad (25)$$

$$[B–H] \rightleftharpoons B^- + H^+ \qquad \Delta G^o = 1.37(pK_{a,acid}) \qquad (26)$$

$$H^+ + H^- \rightleftharpoons H_2 \qquad \Delta G^o = -76 \text{ kcal mol}^{-1} \qquad (27)$$

$$[X–H] + [B–H] \rightleftharpoons [X]^+ + B^- + H_2 \qquad \Delta G^o_{HER} = \Delta G^o_{H-} + 1.37(pK_{a,acid}) - 76 \text{ kcal mol}^{-1} \qquad (28)$$

$$pK_{a,acid} < 0.73(\Delta G^o_{H-}) - 55.5 \qquad (29)$$

Scheme 1.7: Derivation of thermodynamic driving force for H_2 evolution (ΔG^o_{HER}) from a generic compound [X–H] via homolytic (upper) and heterolytic (lower) mechanisms.[3]

Table 1.3: Thermodynamic driving for H_2 evolution from **3** and $[(Cp^*H)Rh(bpy)]^+$ via homolytic and heterolytic mechanisms with increasing acid strength.

Ligand	$\Delta G^o_{HER,homolytic}$ [a]	$\Delta G^o_{HER,heterolytic}$ [a]		
		$[Et_3NH]^+$ [b]	$[C_6H_5NH_3]^+$ [c]	$[DMFH]^+$ [d]
dppb	+26.7	+20.8	+9.5	+3.4
bpy	+15.9	+9.3	–1.9	–8.0

[a] V vs. $Fc^{+/0}$. [b] kcal mol^{-1}. [c] pK_a in CH_3CN = 18.8. [d] pK_a in CH_3CN = 10.6 [e] pK_a in CH_3CN = 6.1.

Table 1.4: Thermodynamic driving for H_2 evolution from $\mathbf{3}^-$ and the reduced form of $[(Cp^*H)Rh(bpy)]^+$ via homolytic and heterolytic mechanisms with increasing acid strength.

Ligand	$\Delta G^o_{HER,homolytic}$ [a]	$\Delta G^o_{HER,heterolytic}$ [a]	
		$[Et_3NH]^+$ [b]	$[C_6H_5NH_3]^+$ [c]
dppb	–41.5	–13.1	–24.4
bpy	–16.9	–6.7	–18.0

[a] kcal mol^{-1}. [b] pK_a in CH_3CN = 18.8. [c] pK_a in CH_3CN = 10.6 [d] pK_a in CH_3CN = 6.1.

Thermochemical parameters such as *BDFE* and ΔG^o_{H-} can be applied to multiple desirable reactions beyond hydrogen evolution. For example, reduction of the greenhouse gas CO_2 to formate (a useful chemical feedstock) is the result of net H^- transfer to CO_2, meaning the hydricity of any given compound can be compared to that of formate (44 kcal mol^{-1})[3] to predict spontaneity of CO_2 hydrogenation using eq. 30.

$$\Delta G^{o}_{CO2red} = \Delta G^{o}_{H-} - \Delta G^{o}_{H-,\,formate} \quad (30)$$

On this basis, the rhodium(III)-hydride is predicted to be fully inert to hydride transfer to CO_2 by 27 kcal mol^{-1}. Meanwhile, the strong reducing power of **3**$^{-}$ (and corresponding low ΔG^{o}_{H-}) causes reduction of CO_2 to formate with **3**$^{-}$ to be thermodynamically favorable, with a driving force of –6.9 kcal mol^{-1}. However, homolytic hydrogen evolution from **3**$^{-}$ is significantly more favorable, with $\Delta G^{o}_{HER,homolytic} - \Delta G^{o}_{CO2red}$ = –34.6 kcal mol^{-1}. A very large activation energy for thermodynamically-preferred homolytic hydrogen evolution with **3**$^{-}$ would therefore be necessary to kinetically promote CO_2 reduction. Based on the irreversibility of the reduction of **3** at typical scan rates of ca. 100 mV s^{-1} (Figure 1.21), the rate of reaction of **3**$^{-}$ to generate H_2 is on the order of the CV timescale. Thus, given the strong thermodynamic preference for and observed lack of kinetic barriers to hydrogen evolution from **3**$^{-}$, we did not attempt CO_2 hydrogenation via reduction of **3**.

The dppb-supported [Cp*Rh] system shows one more regime of reactivity that can be thermodynamically explored. In addition to the previously discussed 1e^{-} reduction, **3** also exhibits a fully irreversible oxidation with $E_{p,a}$ = 0.99 V vs. $Fc^{+/0}$ (Figure 1.31, upper trace). In electrochemistry of the free ligand (Figure 1.31, lower trace), a similar irreversible oxidation is observed at ca. 0.4 V vs. $Fc^{+/0}$; we conclude that 1e^{-} oxidation of **3** is ligand-centered. The anodic shift in potential of ca. 500 mV between free dppb and **3** is consistent with coordination of the ligand to the relatively electron-poor, formally rhodium(III) metal center. When the potential is swept back negative, a cathodic feature that is absent in scans that do not include the 1e^{-} oxidation at 0.99 V grows in with $E_{p,c}$ = –0.82 V vs. $Fc^{+/0}$. This new reduction coincides exactly with the peak cathodic potential of the [$Rh^{III/II}$] couple in **2**, suggesting that following oxidation of **3**, a chemical reaction occurs that generates non-protonated [Rh^{III}]. While eqs. 14 and 15 are only

rigorously applicable to reversible systems, substitution of peak potentials can yield useful upper or lower bounds on various thermochemical values. By rearranging eq. 14 to solve for pK_a, the *BDFE* and $E_{p,a}$ of **3** can be used to calculate the lower bound of the pK_a of the product of oxidation of **3** (**3**$^+$) to be ≥ –9.8. This value suggests that ligand-centered oxidation of **3** increases its acidity by up to 30 orders of magnitude. Using this pK_a and the potential of the [$Rh^{III/II}$] couple in **2** (i.e., the sides of the lowest tier in Figure 1.27), we can also calculate the *BDFE* of **3**$^+$ to be ≥ 23.5 kcal mol^{-1}.

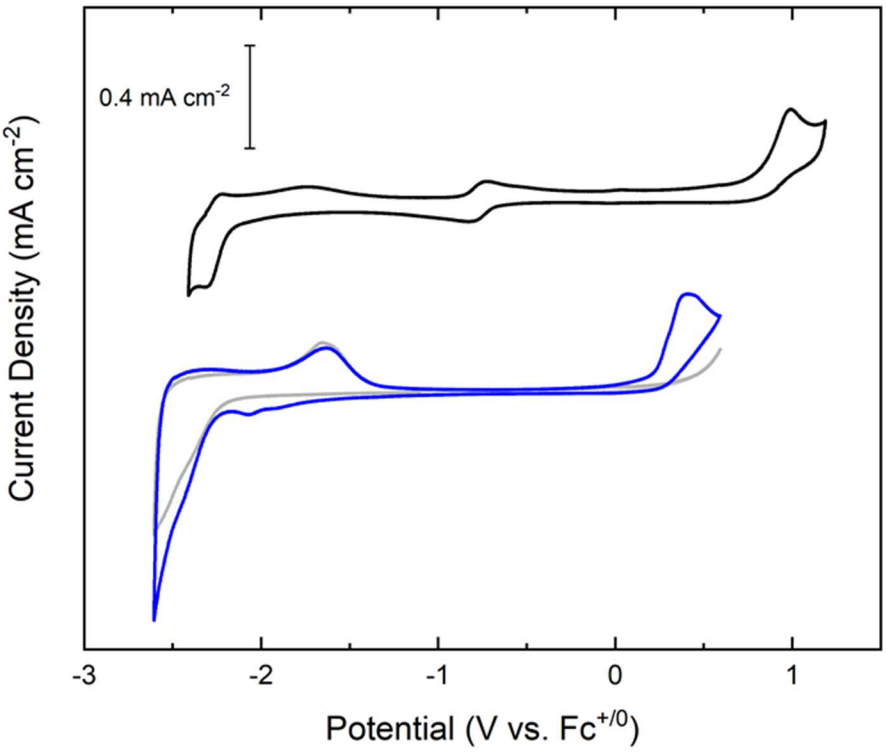

Figure 1.31: Cyclic voltammetry of **3** (1 mM, upper trace; scan 2 is shown) and free dppb ligand (1 mM, lower set of traces; scan 2 of dppb in blue, with a blank in light gray). Electrolyte: 0.1 M $TBAPF_6$ in MeCN, scan rate: 100 mV/s, electrode: highly oriented pyrolytic graphite. The initial potential of all voltammograms is ca. –0.3 V vs. $Fc^{+/0}$.

Based on these bounded values for **3**$^+$, we can suggest several thermodynamically favorable mechanisms. First, ΔG^{o}_{HER} by a homolytic pathway with **3**$^+$ is favorable by up to –55.3 kcal mol^{-1}. Removal of H• from **3**$^+$ would generate [Cp*Rh^{III}(dppb)($NCCH_3$)]$^{2+}$, consistent with

observation of growth in of the [$Rh^{III/II}$] couple of **2** following oxidation of **3**. Alternatively, $\mathbf{3}^+$ formed at the electrode could be deprotonated by **3** in the bulk solution. The products of this reaction would be [$Cp^*Rh^{III}(dppb)(NCCH_3]^{2+}$ and **2**, which would undergo oxidation at the very positive potential necessary to oxidize **3** and form more Rh^{III} solvento species. This mechanism is therefore also consistent with observation of formation of [$Cp^*Rh^{III}(dppb)(NCCH_3]^{2+}$ by CV. In this regime, $\mathbf{3}^+$ behaves as the acid source in eq. 24. ΔG^{o}_{HER} for the heterolytic process, in which oxidized **3** acts as proton donor and **3** acts as hydride donor, can therefore be bounded at ≥ -18.4 kcal mol^{-1}. Of course, all of these values are overestimates of the reactivity of $\mathbf{3}^+$ because the peak anodic potential of **3** is by definition more positive than the midpoint potential of the corresponding theoretical reversible redox couple. Additionally, the previously mentioned omission of free energy changes related to solvent binding is relevant to every determined value in the lowest tier of Figure 1.27. However, even if the midpoint potential of the oxidation of **3** is as much as 100 mV less positive than $E_{p,a}$, the resulting pK_a value only increases by 1.7 units, the *BDFE* of $\mathbf{3}^+$ only increases by ca. 2 kcal mol^{-1}, and the driving forces for homolytic and heterolytic hydrogen evolution retain their signs. Overall, then, it is very likely that ligand-centered oxidation of **3** at 0.99 V vs. $Fc^{+/0}$ serves to thermodynamically activate the inert [Rh^{III}–H] to a similar degree as reduction at the metal center, giving rise to the irreversibility of this oxidation in electrochemistry. Further study of an analogous [Cp*Rh–H] with a reversible oxidation might provide more substantive evidence of this additional reactivity manifold. This concept is tested in Chapter 2.

Conclusions and Future Directions

The rhodium half-sandwich complex Cp*Rh(dppb) reacts with acid to form an isolable monohydride, $[Cp^*Rh(dppb)H]^+OTf^-$. There is no evidence of generation of coordinated pentamethylcyclopentadiene or free Cp*H under these conditions, in accord with formation of a

strong Rh–H bond. This interaction is quite stable, as the hydride complex is not protonated by the strong acid $DMFH^+$ to yield H_2 over 48 h of monitoring by NMR, consistent with the experimentally determined positive driving force for reaction between the hydride complex and $[DMFH]^+$ (ΔG^o_{HER} = 3.4 kcal mol^{-1}). However, the isolated hydride undergoes reduction at –2.34 V, leading to generation of H_2 and formation of Cp*Rh(dppb); this correlates well with the ΔG^o_{HER} of homolytic H_2 evolution from the reduced rhodium(III) hydride, which was found to be –41.5 kcal mol^{-1}. Taken together, these studies suggest that $[Cp^*Rh^{III}]$ hydride complexes can be remarkably stable species. As over-stabilization of both [Cp*H] complexes and Rh–H species appears to impede productive catalysis, a possible design rule for improved catalysis involving proton-driven transformations with compounds in the [Cp*Rh] family may be use of ligands that enable H-bridging states between the metal center and the [Cp*] ring.

While thermochemical work provides a strong basis for rationalization of the various reactivity manifolds of the rhodium hydride **3**, the key factors influencing site of protonation (i.e., at the metal center vs. at the Cp* ring) remain unknown. One plausible explanation is that phosphines are better Lewis bases then imine ligands, leading to stabilization of the rhodium(III) center in **3** rather than the formal rhodium(I) oxidation state in [Cp*H] complexes. Decreasing the electron-donating ability of dppb (e.g., by exchanging the phenyl rings for pentafluorophenyl- rings) with the intent of favoring formation of a [(Cp*H)Rh(diphosphine)] is one strategy for testing this hypothesis.

Chapter 2

REMOTE OXIDATIVE ACTIVATION OF A HETEROBIMETALLIC DIPHOSPHINE-SUPPORTED HALF-SANDWICH MONOHYDRIDE

This chapter is the basis of a manuscript in preparation: Boyd, E. A.; Lionetti, D.; Day, V. W.; Blakemore, J. D. Remote Oxidative Activation of a [Cp*Rh] Monohydride. *In preparation.*

Abstract

In this chapter, the preparation and characterization of a series of [Cp*Rh(dppf)] complexes (Cp* = η^5-pentamethylcyclopentadienyl, dppf = κ^2-bis-(diphenylphosphinoferrocene)] are described, with particular attention paid to the outcomes of proton and electron transfer on this framework. Notably, Cp*Rh(dppf) exhibits a quasireversible $Rh^{II/I}$ reduction at –0.96 V vs. $Fc^{+/0}$ rather than undergoing a net $2e^-$ $Rh^{III/I}$ process as is often observed on the [Cp*Rh] platform. This behavior provides access to a species in the relatively uncommon rhodium(II) oxidation state which has been characterized by EPR. Protonation of Cp*Rh(dppf) results in formation of an isolable [Cp*Rh] monohydride that is inert to protonolysis, providing a second example of the stabilizing effect bidentate diphosphine ligands have on Rh–H bonds as introduced and described in Chapter 1. The quasireversibility of the dppf-centered $Fe^{III/II}$ couple of the rhodium monohydride $[Cp*Rh(dppf)H]^+$ at +0.41 V vs. the ferrocenium/ferrocene redox couple (denoted $Fc^{+/0}$) facilitates a rigorous thermochemical analysis of the system, from which we have determined that oxidation at the dppf ligand results in dramatically increased acidity of the Rh–H bond by 23 pK_a units.

Introduction

A primary strength of transition metal catalysts lies in their ability to cycle among two or more oxidation states, thereby facilitating mediation of electron transfer during transformations of various substrates. Traditionally, ligands in catalytic metal complexes were viewed as sources of structural support or as sites for modulation of the properties of the metal center via synthetic tuning of steric or electronic effects. However, a large body of work has explored ligand "non-innocence", or the ability of ligands to actively participate in electron transfer and/or bond-making and -breaking steps in catalysis.[53] The most common class of non-innocent ligands is composed of redox-active ligands, which can undergo oxidation or reduction with no change to the formal

oxidation state at the metal center to which they are bound. This ability has been proposed by Chirik and Wieghardt as the key to replacement of expensive second- or third-row transition metal catalysts with their first row analogues, as the $1e^-$ redox processes of first-row metals can synergistically combine with $1e^-$ processes at their ligands to achieve the net $2e^-$ transfers that make heavier transition metals so effective for catalysis of organic reactions.[54]

In our group's work, the redox activity of a variety of diimine ligands plays a key role in modulating the reactivity and overpotential of hydrogen evolution catalysts of the type $[Cp^*Rh(diimine)(Cl)]^+$. The rhodium(I) complex Cp*Rh(phen), for example, exhibits extensive delocalization of electron density onto the redox-active phen ligand and stabilizes a very electron-rich metal center, facilitating catalysis at a modest overpotential.[19] Installation of strongly electron-withdrawing nitro ($–NO_2$) groups at the 4 and 4` positions of the bpy ligand increases its redox non-innocence to the extent that the first reduction of $[Cp^*Rh(Cl)(^{NO2}bpy)]^+$ is fully localized on the organic ligand.[55] This system is incapable of reaction with protons, suggesting that the reduction-stabilizing effect of ^{NO2}bpy might exceed a limit beyond which the reducing power of the metal center is inadequate for proton reduction. Similarly, while metal-centered $1e^-$ reduction of the $[Cp^*Rh(dppb)H]^+$ **3** occurs at –2.35 V vs. $Fc^{+/0}$, the analogous $[Cp^*Rh(pqn)H]^+$ (pqn = 8-(diphenylphosphino)quinoline) complex is reduced ca. 600 mV more positive.[56] This anodic shift is attributed to localization of the reduction event for this complex on the redox-noninnocent pqn ligand. As a result, if either rhodium hydride complex were a competent catalyst for hydrogen evolution, the pqn analogue would afford a much lower overpotential.

As discussed in Chapter 1, it is also possible to activate an inert $[Cp^*Rh^{III}–H]$ by ligand-centered oxidation. In cyclic voltammetry studies we observe that oxidation of dppb at +0.99 V vs. $Fc^{+/0}$ in **3** results in generation of a non-protonated $[Cp^*Rh^{III}]$ species. While the exact nature

of this reaction has not been explored further (e.g., identification of other metal-containing products or the fate of the hydride), we have determined that dppb oxidation gives rise to an increase in the acidity of the Rh–H bond by as much as 30 orders of magnitude. However, given the irreversibility of the dppb oxidation, we are unable to obtain a midpoint potential ($E_{1/2}$) with which to pinpoint the magnitude of thermochemical changes incurred by oxidation of **3**. We therefore targeted synthesis of a [Cp*Rh^{III}–H] supported by a diphosphine ligand with reversible electrochemistry at anodic potentials to gain insight into this new manifold of reactivity promoted by ligand-centered oxidation.

To carry out this work, we looked to an interesting class of redox-active ligands which consists of metallocenes such as ferrocene or cobaltocene appended with groups capable of coordinating to a second metal center. The reversibility of one-electron reduction or oxidation of such metallocenyl moieties provides access to two stable forms of the same ligand framework, enabling nearly effortless but dramatic tuning of the ligand field simply via application of an electrochemical potential. To illustrate this effect, Wrighton and coworkers have shown that ligand-centered oxidation of a $Re(CO)_3$ complex supported by bis-(diphenylphosphino)ferrocene (dppf) results in 10-20 cm^{-1} increases in the energies of the CO stretches, indicative of a decrease in the electron density at the metal center.[57] Similarly, Mirkin and coworkers found that oxidation of ferrocenyl groups appended to an arene ligand results in weakening of the metal-arene interaction by 3.3 kcal mol^{-1}.[58] Significant attention surrounds these "redox switches", with applications in electrochemical sensing,[59] metal ion transport systems,[60] and catalysis. In this last arena, Wrighton *et. al.* have shown that a rhodium complex ligated by bis-(diphenylphosphino)cobaltocene catalyzes hydrosilylation of ketones and alkenes in the cobalt(III) form but hydrogenation of ketones and alkenes in the reduced cobalt(II) state.[61]

Here, we discuss the preliminary results of our ongoing study of a new series of [Cp*Rh] complexes ligated by dppf. Analogous to the previous diphosphine and diimine-supported species studied, two-electron reduction of the [Cp*Rh^{III}–Cl] complex **4** yields the rhodium(I) species **5**; however, cyclic voltammetry (CV) studies of **5** in the weakly coordinating solvent THF reveal that the product of oxidation of **5** by one electron is stable on the CV timescale. Indeed, chemical oxidation by one electron of **5** yields a paramagnetic complex with an axial EPR spectrum indicative of a single rhodium-centered unpaired electron. Protonation of **5** returns an inert [Cp*Rh–H] (**7**) that is analogous to that described for the dppb system in Chapter 1. However, oxidation of the dppf iron center in **7** is quasireversible at fast scan rates, enabling identification of a midpoint potential ($E_{1/2}$ = +0.41 V vs. $Fc^{+/0}$) for use in determining accurate thermochemical values. Notably, oxidation of dppf increases the acidity of the rhodium-hydride by 23 pK_a units. Based on these findings, we postulate that alternative metallocenyl diphosphine ligands on the [Cp*Rh] framework might promote highly selective, tunable catalysis for reactions beyond proton reduction. Future directions for this project are also described.

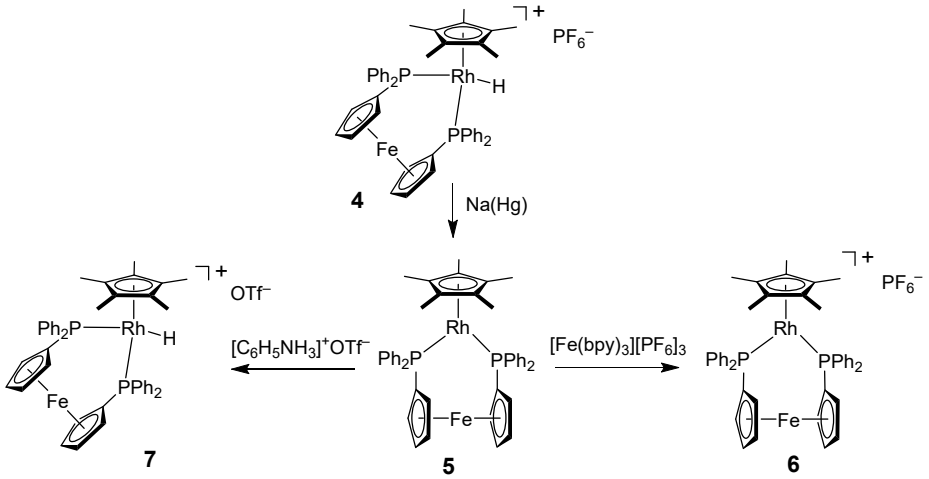

Scheme 2.1: Summary of preparation and reactivity of [Cp*Rh] complexes supported by the dppf ligand.

Electrochemistry of [Cp*Rh(dppf)Cl][PF_6] (4)

The synthesis, spectroscopic characterization, and XRD structure of the [Cp^*Rh^{III}–Cl] chloride complex of dppf (**4** in Scheme 2.1) has been previously reported;[62] however, the electrochemical properties of **4** have not been investigated in any prior work. At oxidizing potentials, the CV of **4** in THF (Figure 2.1) contains one quasireversible couple centered at 0.38 V vs. $Fc^{+/0}$ with a peak-to-peak separation of 158 mV typical of $1e^-$ couples in THF ($\Delta E_p(Fc^{+/0}) \approx 200$ mV in THF). We assign this couple to $Fe^{III/II}$ cycling in the ferrocene moiety of the dppf ligand. The shift in potential positive of underivatized ferrocene is similar to that observed for iron-centered oxidation in an analogous ruthenium(II) complex of dppf ($E_{1/2} = 0.41$ V vs. $Fc^{+/0}$).[63] The peak anodic and cathodic currents for the $Fe^{III/II}$ couple vary linearly with the square root of scan rate (Figure 2.2), indicating that both **4** and the product of its oxidation (presumably [Cp^*Rh^{III}(Cl)(dppf)]$^{2+}$) are freely diffusing in solution.

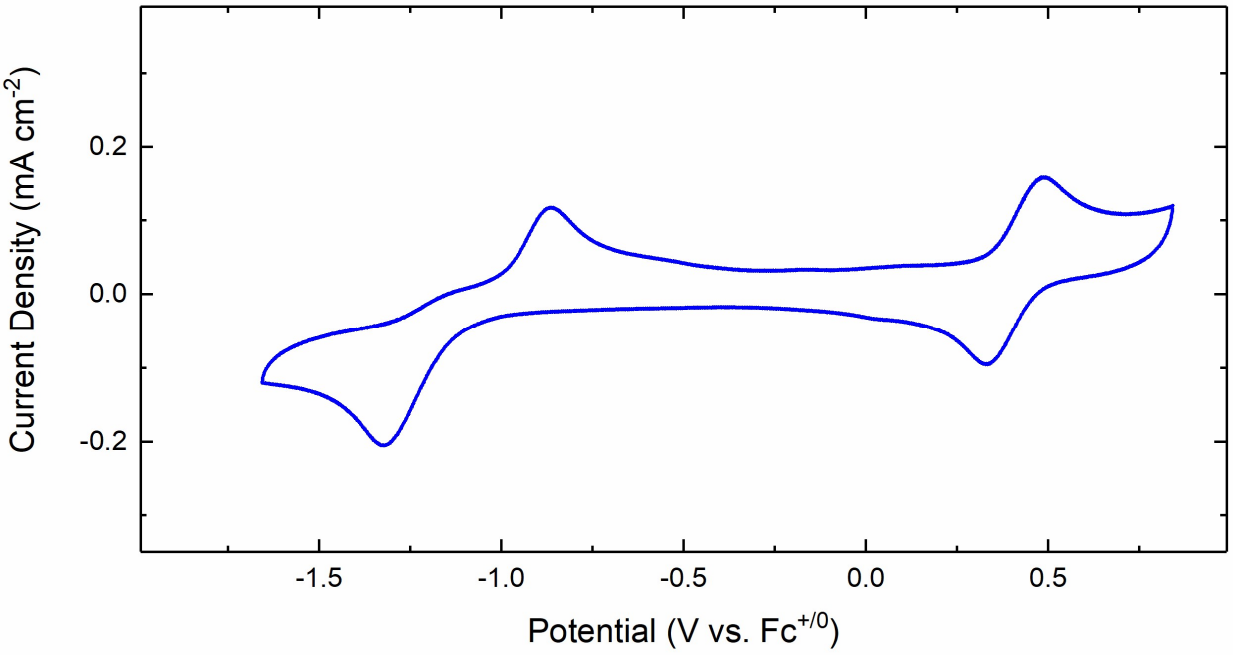

Figure 2.1: Cyclic voltammetry of **4** (THF, 0.1 M [^{n}Bu$_4$N][PF_6], 100 mV/s). The second complete cycle of voltammetry is shown here. The trace was collected beginning at –0.6 V vs. $Fc^{+/0}$ and sweeping cathodically.

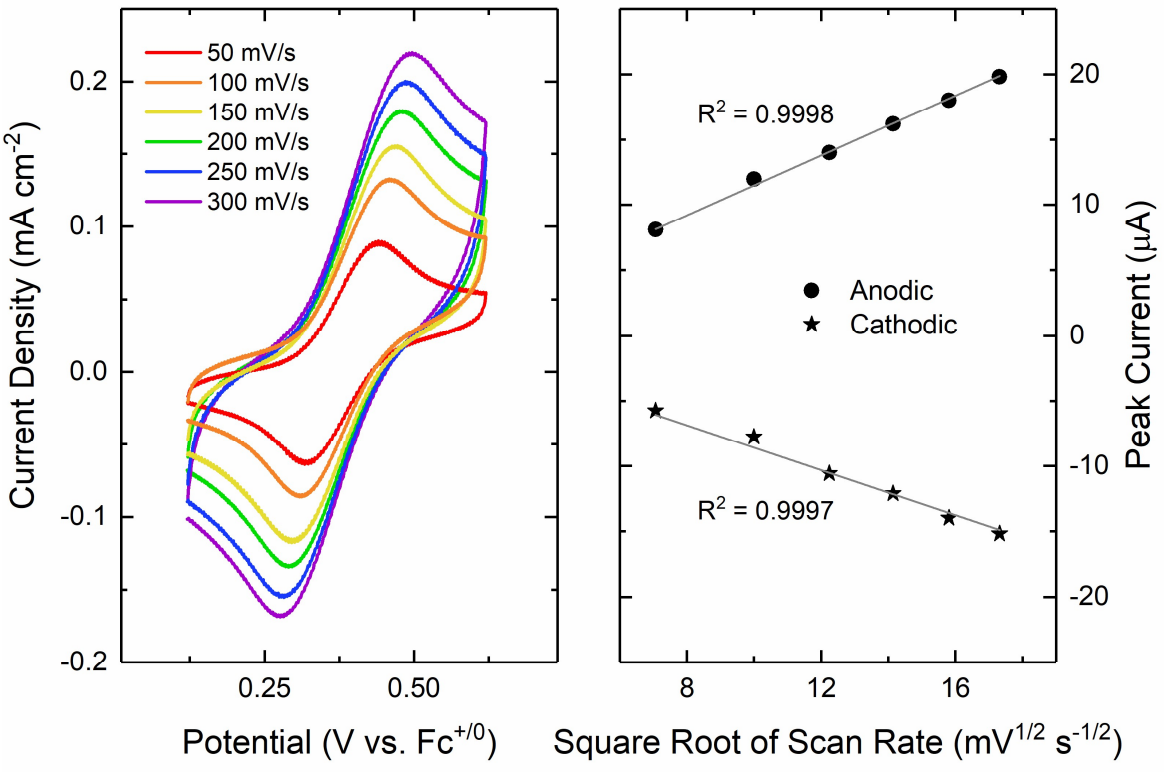

Figure 2.2. Left: cyclic voltammetry of **4** at varying scan rate in THF (0.1 M [^{n}Bu$_4$N][PF$_6$], highly oriented pyrolytic graphite working electrode). The initial potential of all voltammograms is ca. +0.1 V vs. Fc$^{+/0}$. Right: linear dependence of peak cathodic current on square root of scan rate with the y-intercept set to 0.

Scanning cathodically from ca. –0.6 V vs. Fc$^{+/0}$, **4** undergoes a reduction followed by a return oxidation, with $E_{1/2}$ = –1.12 V vs. Fc$^{+/0}$ (Figure 2.1) and approximately double the cathodic current of the Fe$^{III/II}$ couple of **4** ($i_{p,c}$(Fe$^{III/II}$) = –7.8 μA, $i_{p,c}$(–0.89 V) = –14.7 μA). We can therefore assign this feature as 2e$^-$ reduction of the rhodium center, analogous to the 2e$^-$ reduction of the dppb-supported [Cp*Rh–Cl] **1**. The peak currents of the Rh$^{III/I}$ couple vary linearly with square root of scan rate, indicating that both **4** and its reduced form are freely diffusing and soluble in THF; notably, cyclic voltammetry of **4** in CH$_3$CN does not produce this linear trend, likely due to insolubility of the corresponding rhodium(I) species in CH$_3$CN. We therefore chose to conduct all electrochemical experiments with [Cp*Rh(dppf)] species in THF.

Even accounting for the poor electron transfer properties of THF relative to acetonitrile, the peak-to-peak separation of the $Rh^{III/I}$ couple for **4** is quite large (ca. 460 mV) and the anodic wave is rather broad, consistent with an underlying chemical step in the observed redox profile. Given the similarities between the rhodium-centered features in cyclic voltammetry of **4** and **1**, **4** likely undergoes the same ECE-type mechanism with potential inversion—i.e., following $1e^-$ reduction, loss of the chloride ligand generates a transient $17e^-$, five-coordinate species with a reduction potential equal to or more positive than that of the initial $18e^-$ chloride-bound complex **4**. This assignment is substantiated by the appearance of a small cathodic feature positive of the principal $2e^-$ reduction of **4** after several scans (Figure 2.3), reminiscent of the feature in electrochemistry of **1** assigned to reduction of the solvento complex $[Cp^*Rh(dppb)(NCCH_3)]^{2+}$ generated *in situ* from oxidation of the $18e^-$, five-coordinate $[Cp^*Rh^I]$ complex **2**. In the case of **4** in THF, the reduction feature of the analogous solvento species $[Cp^*Rh(dppf)(THF)]^+$ is less pronounced because THF is a significantly poorer ligand than CH_3CN, favoring rebinding of chloride rather than formation of the solvento complex.

The reduction of the dppf complex occurs ca. 250 mV more negative than the dppb complex. The wider bite angle of dppf relative to dppb may be the source of this shift; the six-membered metallocycle required by dppf enforces a P–Rh–P bite angle of 95.6° in **4**,[62] compared to 81.76° in the dppb-supported complex **1**.[64] Both $[Cp^*Rh^{III}–Cl]$ complexes are pseudo-octahedral, so the ability of dppf to better approximate the ideal octahedral L–M–L angle of 90° may increase overlap between the ligand and metal orbitals.[65] Because dppf is primarily a σ-donor to the rhodium(III) center, this would lead to a more electron-rich metal center, giving rise to the cathodic shift in $2e^-$ reduction of **4** compared to **1**.[66]

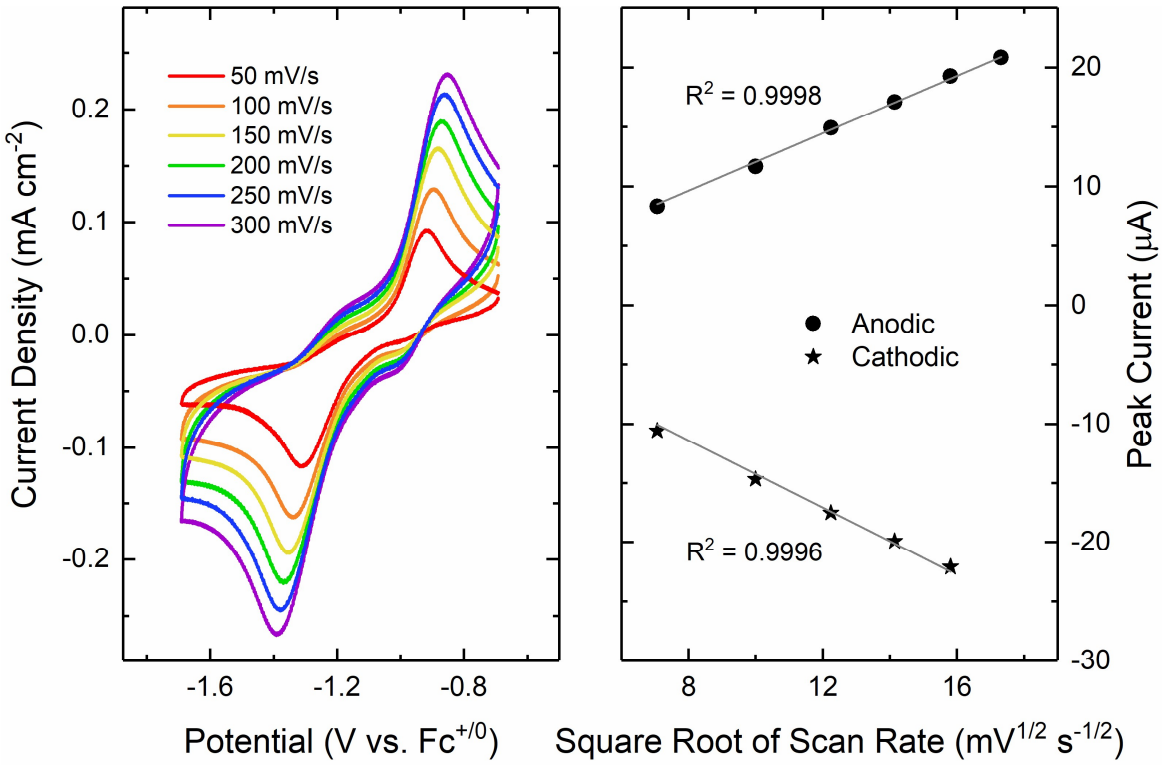

Figure 2.3. Left: cyclic voltammetry of **4** at varying scan rate in THF (0.1 M [^{n}Bu$_4$N][PF$_6$], highly oriented pyrolytic graphite working electrode). The initial potential of all voltammograms is ca. –0.7 V vs. Fc$^{+/0}$. Right: linear dependence of peak cathodic current on square root of scan rate with the y-intercept set to 0.

Synthesis and NMR Characterization of [Cp*Rh(dppf)] (5)

Consistent with our assignment of the quasi-reversible redox event centered at –1.12 V vs. Fc$^{+/0}$ in electrochemistry of **4** as a 2e$^-$ Rh$^{III/I}$ couple, reduction of **4** with excess sodium amalgam (10 equiv.) in THF yields the reddish-brown diamagnetic solid **5** following extraction with toluene. The ^{1}H NMR of this compound (Figure 2.4) is qualitatively very similar to that of its dppb-supported analogue **2**; the 15-proton singlet at 1.48 ppm corresponds to the methyl protons of the Cp* ring, while the 8-proton multiplet at 8.05 ppm, the 8-proton triplet (J = 7.5 Hz) at 7.20 ppm, and the 4-proton triplet (J = 7.3 Hz) at 7.10 ppm strongly resemble the peak shapes of the *ortho*, *meta*, and *para* phenyl protons, respectively, in **2**. The spectrum of **5** also includes two singlets at 4.24 ppm and 3.84 ppm which represent the protons on the Cp rings of the ferrocene moiety.

Notably, the presence of only two signals for the Cp rings indicates that **5** has C_{2v} symmetry in solution, consistent with loss of chloride to generate the five-coordinate pseudo-square planar complex depicted in Figure 2.4; in the C_s complex **4**, the Cp rings show twice as many peaks because the dppf ligand is tilted up, orienting two sets protons on each Cp ring toward the extra chloride ligand and the other two sets toward Cp*. Similarly, as observed in **2**, the number of signals representing phenyl protons halves in moving from C_s **4** to C_{2v} **5**. The $^{31}P\{^{1}H\}$ NMR spectrum of **5** (Figure 2.6) shows a doublet at 50.07 ppm with $^{1}J_{P,Rh}$ = 232 Hz, indicating that dppf remains coordinated to the metal center and corroborating formation of a rhodium(I) species ($^{1}J_{P,Rh}$ = 230 in the [Cp*Rh^{I}] complex **2**).

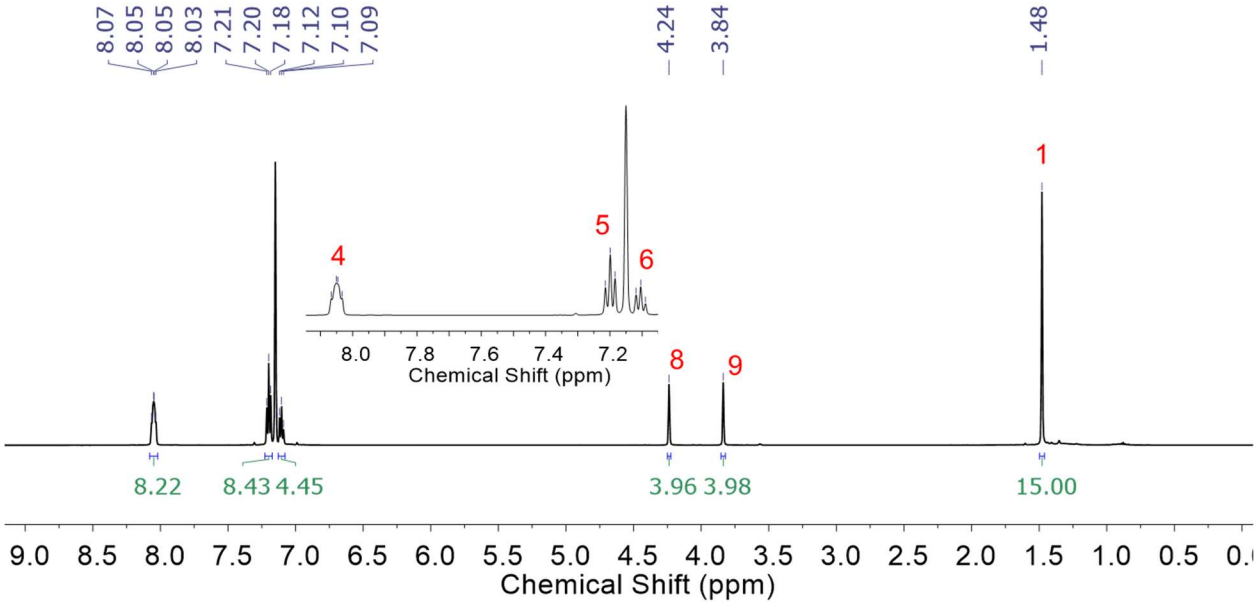

Figure 2.4: ^{1}H NMR spectrum (C_6D_6, 500 MHz) of **5**. See Figure 2.5 for key to numbering scheme.

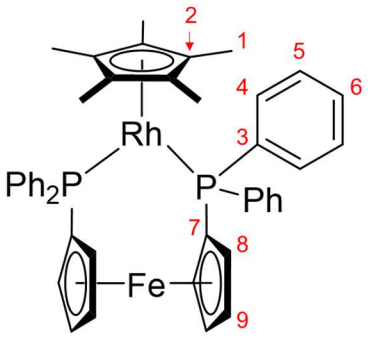

Figure 2.5: Numbering scheme for assignment of NMR data for complex **5**.

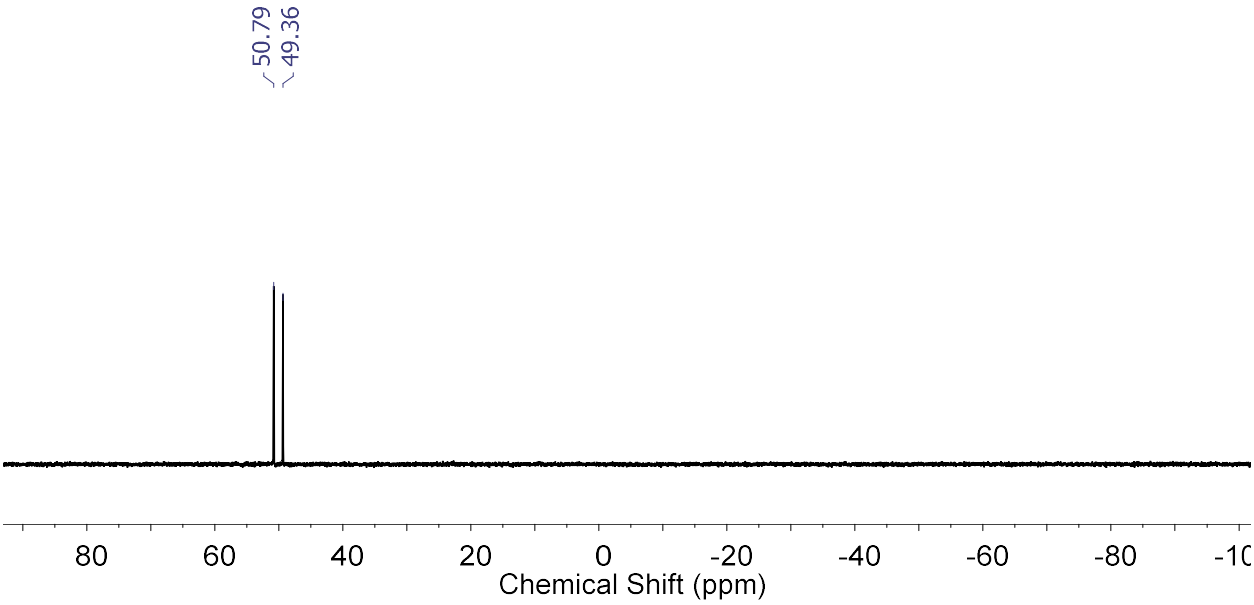

Figure 2.6: $^{31}P\{^{1}H\}$ spectrum (C_6D_6, 162 MHz) of **5**.

The $^{13}C\{^{1}H\}$ spectrum of **5** (Figure 2.7) is also consistent with the proposed structure. The nine carbon environments in **5** were located in the spectrum, and all peaks were assigned on the basis of HSQC spectroscopy (see Appendix A2 for spectra and rationale). The two Cp environments were differentiated by the increase in coupling to phosphorus expected when moving from the carbon directly adjacent to the phosphorus substituent to the next carbon in the ring; this trend is observed between the two triplets at 74.45 and 71.51 ppm, which have J = 5.5 Hz and J = 3.3 Hz, respectively. As observed with the dppb ligand, the phenyl carbons appear as triplets with coupling constants of ca. 7 Hz despite the magnetic inequivalence of the two I = ½ phosphorus nuclei.

While the source of this splitting pattern remains unclear, it does appear to remain relatively constant across multiple rhodium-diphosphine frameworks.

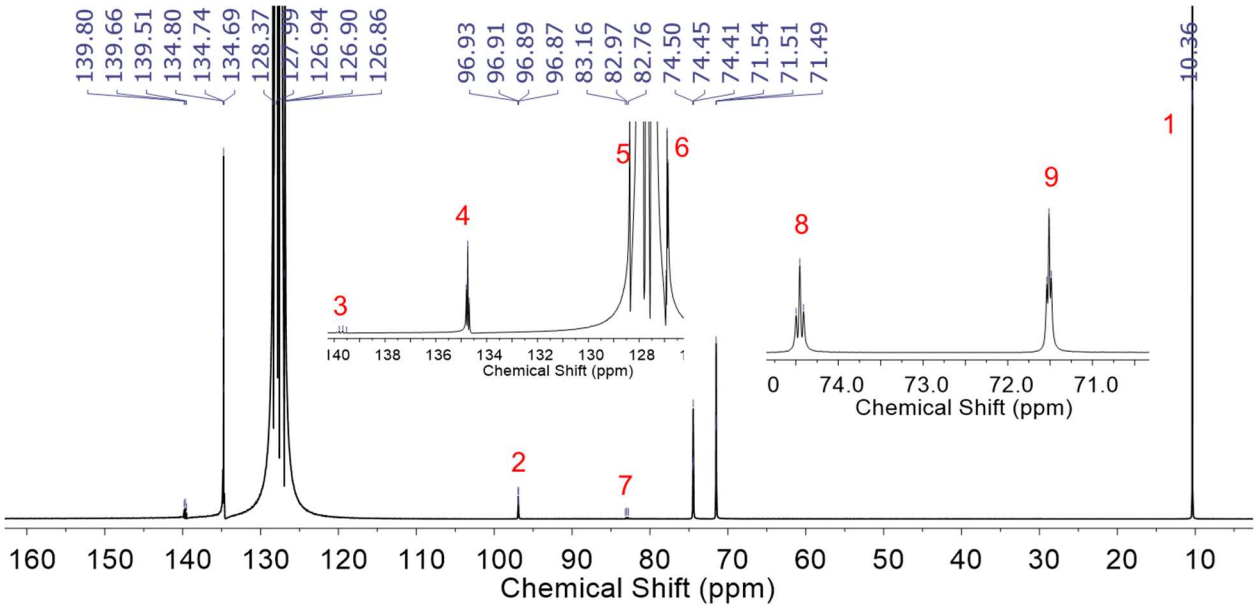

Figure 2.7: $^{13}C\{^{1}H\}$ NMR spectrum (C_6D_6, 126 MHz) of **5**. See Figure 2.5 for key to numbering scheme.

Cyclic Voltammetry of [Cp*Rh(dppb)] (5)

Beginning at negative potentials and sweeping anodically at 100 mV/s, the cyclic voltammogram of **5** first shows a quasireversible redox event centered at –0.96 V vs. $Fc^{+/0}$ with ΔE_p = 171 mV (Figure 2.9). The peak currents of this couple vary linearly with the square root of scan rate (Figure 2.8), indicating that **5** and its oxidized form are freely diffusing and soluble in THF. The peak of the anodic wave coincides with the $Rh^{III/I}$ oxidation in **4**, suggesting that **5** is generated *in situ* by electrochemical $2e^-$ reduction of **4**. However, scanning further positive reveals an irreversible anodic feature with $E_{p,a}$ = –0.01 V vs. $Fc^{+/0}$, followed by another quasireversible redox couple at +0.51 V vs. $Fc^{+/0}$. Based on this oxidizing midpoint potential and the similarity of the peak-to-peak separation to that of the $Fe^{III/II}$ couple in **4** (ΔE_p = 178 and 158 mV in **5** and **4**, respectively), the second quasireversible event can be assigned as the $Fe^{III/II}$ couple in **5**. It is shifted

ca. 130 mV positive of the $Fe^{III/II}$ redox potential for **4**. This indicates that the iron(II) species being oxidized at +0.51 V in the CV of **5** is less electron rich than **4**, which has an analogous oxidation at +0.38 V; the primary difference between these two systems is the absence of chloride anions in cyclic voltammetry of **5**. Thus, while presence of the X-type chloride ligand in **4** mitigates charge buildup upon oxidation, the lack of available chloride anions in the cyclic voltammetry of **5** prevents this stabilization and shifts the $Fe^{III/II}$ potential positive.

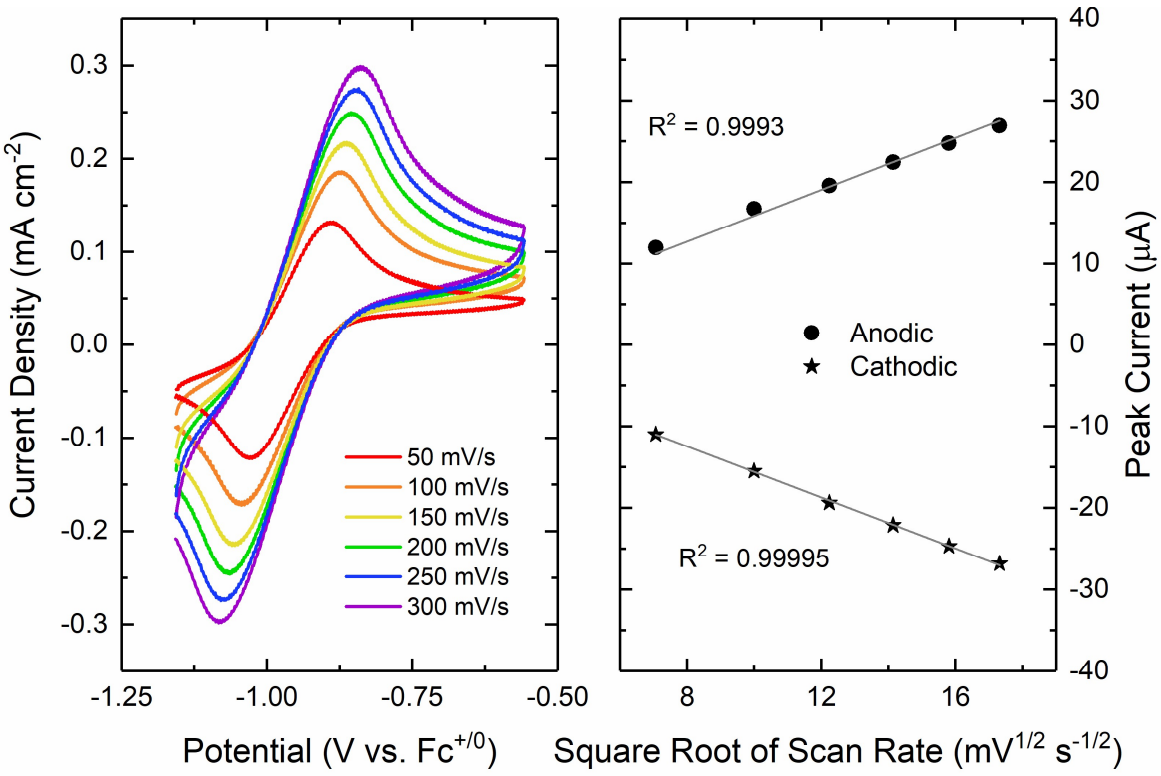

Figure 2.8: Left: cyclic voltammetry of **5** at varying scan rate in THF (0.1 M $[^nBu_4N][PF_6]$, highly oriented pyrolytic graphite working electrode). The initial potential of all voltammograms is ca. –1.2 V vs. $Fc^{+/0}$. Right: linear dependence of peak cathodic current on square root of scan rate with the y-intercept set to 0.

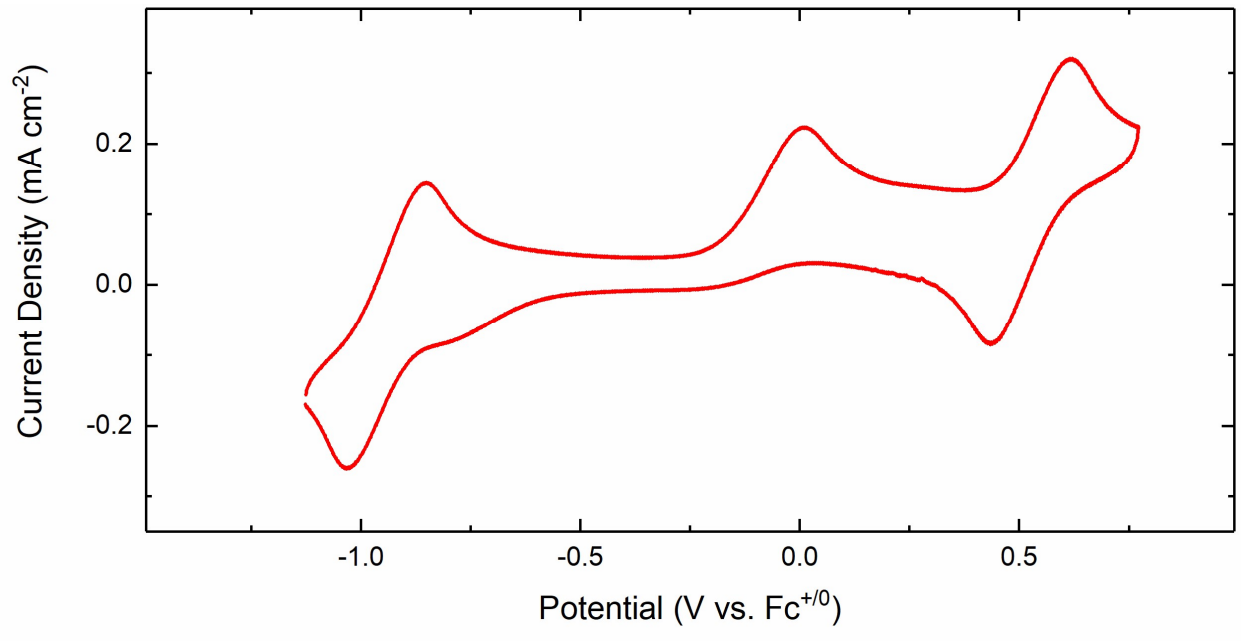

Figure 2.9: Cyclic voltammetry of **5** (THF, 0.1 M [^{n}Bu$_4$N][PF$_6$], 100 mV/s). The second complete cycle of voltammetry is shown here. The trace was collected beginning at ca. –1.2 V vs. Fc$^{+/0}$ and sweeping anodically.

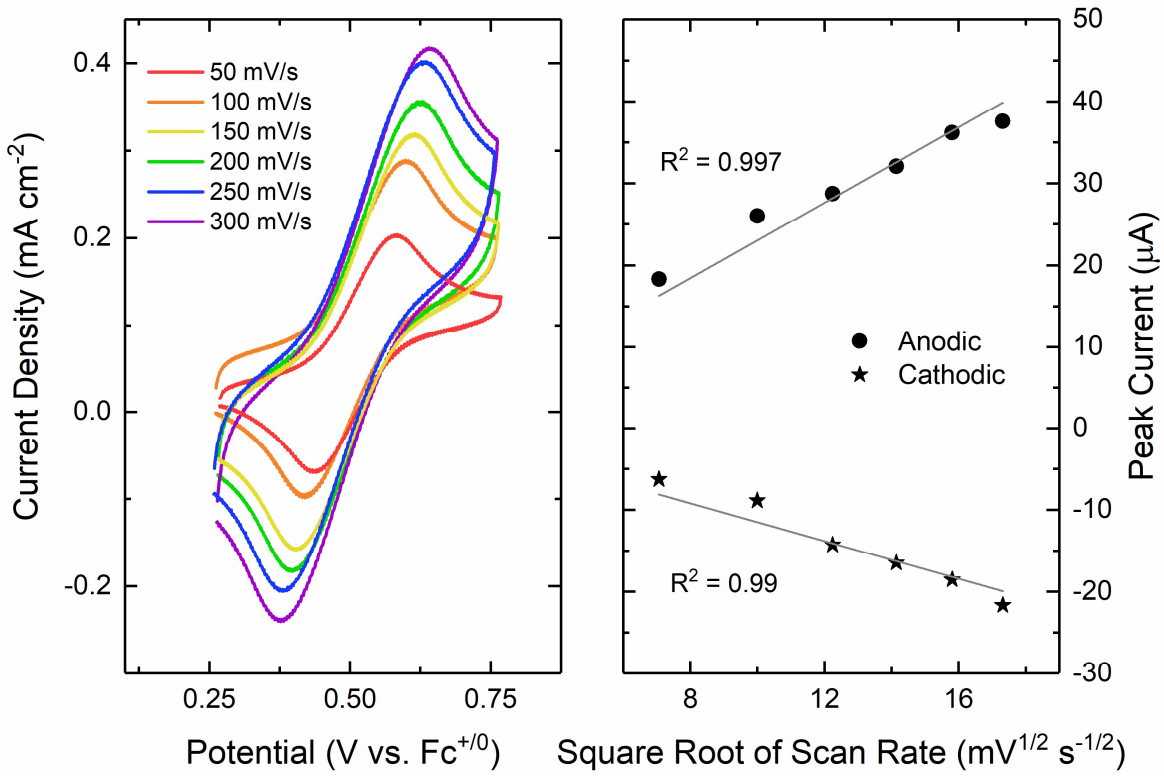

Figure 2.10: Left: cyclic voltammetry of **5** at varying scan rate in THF (0.1 M [^{n}Bu$_4$N][PF$_6$], highly oriented pyrolytic graphite working electrode). The initial potential of all voltammograms is ca. +0.25 V vs. Fc$^{+/0}$. Right: linear dependence of peak cathodic current on square root of scan rate with the y-intercept set to 0.

Notably, the peak-to-peak separations for the rhodium-centered couple at –0.96 V and the Fe$^{III/II}$ event are very similar (ΔE_p = 171 mV and 178 mV, respectively), as are the heights of the two couples ($i_{p,a} - i_{p,c}$ = 26 μA and 20 μA). Given the assignment of the positive event as a 1e$^-$ ferrocene couple, the redox activity at –0.96 V attributed to the rhodium center therefore must also be a 1e$^-$ process rather than the 2e$^-$ ECE process that is typical of [Cp*Rh] systems supported by bidentate diimine or diphosphine ligands. Thus, we assign the quasireversible event at –0.96 V as the Rh$^{II/I}$ couple in **5**. Meanwhile, the irreversible oxidation at ca. 0 V vs. Fc$^{+/0}$ (which is observed both in isolated **5** and in electrochemical experiments that generate **5** *in situ* in the absence of chloride anions, *vide infra*) corresponds to 1e$^-$ oxidation of rhodium(II) to rhodium(III). In fact, this oxidation does not appear to be fully irreversible; the broad feature at –0.82 (Figure 2.9) is

only present after traversing the 1e$^-$ oxidation at –0.01 V, indicating that the species reduced at –0.85 V is produced in the electrochemical oxidation at –0.01 V.

Our working interpretation of this unusual CV profile centers around the poor ligand properties of THF compared to CH_3CN. As shown in Scheme 2.2, oxidation of **5** likely yields a 17e$^-$, five coordinate, rhodium(II) species. However, while the analogous species supported by dppb in acetonitrile is in equilibrium with a 19e$^-$, six coordinate, rhodium(II)-solvento species which can immediately undergo subsequent oxidation, this equilibrium (if it exists at all) is shifted much more dramatically toward the 17e$^-$ species in poorly coordinating THF solution. Thus, the 17e$^-$ species persists in solution and is not oxidized until –0.01 V, well positive of the $Rh^{III/II}$ potentials observed even in those complexes that do not display potential inversion upon formation of the 19e$^-$ solvento species.[56] Upon oxidation, the resulting 16e$^-$ rhodium(III) species would likely be electron-deficient enough to require immediate binding of THF to form the 18e$^-$ Rh^{III} solvento complex $[Cp^*Rh(dppf)(THF)]^{2+}$. This species can then undergo reversible oxidation at the iron center of dppf (consistent with our interpretation of the anodic shift in potential of the $Fe^{III/II}$ couple compared to that of **4**). The broad feature at –0.82 V would then correspond to reduction of $[Cp^*Rh(dppf)(THF)]^{2+}$. The exceptionally wide peak-to-peak separation of the formally $Rh^{III/II}$ "couple" (ΔE_p = 810 mV) is consistent with our current interpretation, as the anodic wave corresponds to oxidation of a 17e$^-$ species to a 16e$^-$ species while the cathodic wave corresponds to reduction of an 18e$^-$ solvento species to a 19e$^-$ solvento species (i.e., an unfavorable oxidation does not track directly with a favorable reduction as is the case in a typical 1e$^-$ redox couple with no associated chemical steps). To test this hypothesis, we will perform electrochemical titration experiments with either CH_3CN or a source of chloride anions (such as $^nBu_4NCl$) to shift the

equilibrium of sixth ligand coordination to the rhodium(II) species (i.e., the leftmost vertical equilibrium process in Scheme 2.2) toward the rhodium(II) solvento complex.

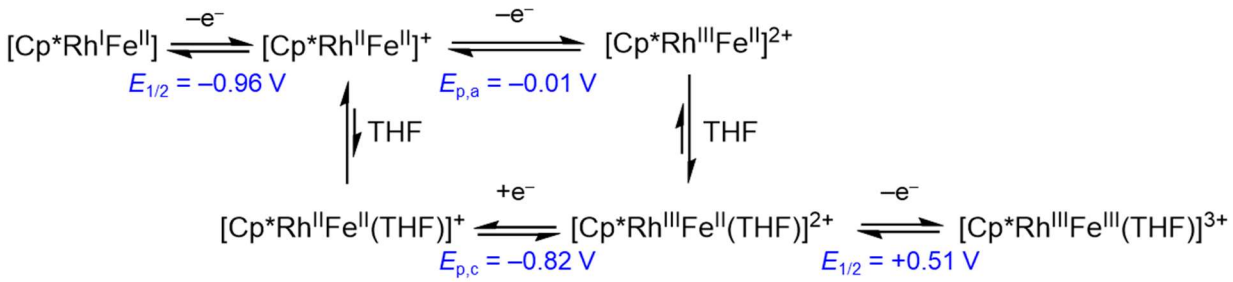

Scheme 2.2: Interpretation of the CV profile of **5**, including potentials for each assigned redox process from data in Figure 2.9. The dppf ligand is abbreviated to Fe^{n} (n = II,III) for simplicity.

Synthesis and EPR Characterization of [Cp*Rh(dppf)]$^{+}$ (6)

While further work is necessary to fully characterize the processes giving rise to the second oxidative feature in cyclic voltammetry of **5**, assignment of the 1e^{-} couple centered at –0.96 V vs. $Fc^{+/0}$ (Figures 2.8 and 2.9) as a $Rh^{II/I}$ couple is substantiated by parallel chemical work. Specifically, addition of 1 equiv. decamethylferrocenium ($[Cp^*_2Fe]^{+}$, $E_{1/2}$ = –0.59 V vs. $Fc^{+/0}$) as a THF suspension to a THF solution of **5** leads to rapid color change from reddish-brown to dark green.[40] The reduction potential of $[Cp^*_2Fe]^{+}$ falls well positive of the $Rh^{II/I}$ couple of **5** and lies negative of not only the peak anodic potential assigned as $Rh^{III/II}$ oxidation ($E_{p,a}$ = –0.01 V vs. $Fc^{+/0}$), but also the midpoint potential of this oxidation and its return cathodic feature ($E_{1/2}(Rh^{III/II})$ = –0.43 V vs. $Fc^{+/0}$), suggesting that this choice of oxidant should result in removal of only one electron from complex **5**. Indeed, hexanes extraction after removal of volatiles contains decamethylferrocene in ca. 95% yield, indicating that electron transfer to $[Cp^*_2Fe]^{+}$ has occurred to completion. Subsequent washing with Et_2O and toluene followed by extraction with THF yields the dark green solid **6** that is ^{1}H NMR-silent (Figure 2.11). The $^{31}P\{^{1}H\}$ NMR spectrum of this material (Figure 2.12) shows no peaks corresponding to the dppf ligand, but does exhibit a septet

at –148 ppm ($^1J_{P,F}$ = 706 Hz) corresponding to the $[PF_6]^-$ counteranion. Taken together, these spectra are indicative of formation of a paramagnetic cation such as $[Cp^*Rh^{II}(dppf)]^+$, the predicted product of $1e^-$ oxidation of **5** based on its electrochemical profile.

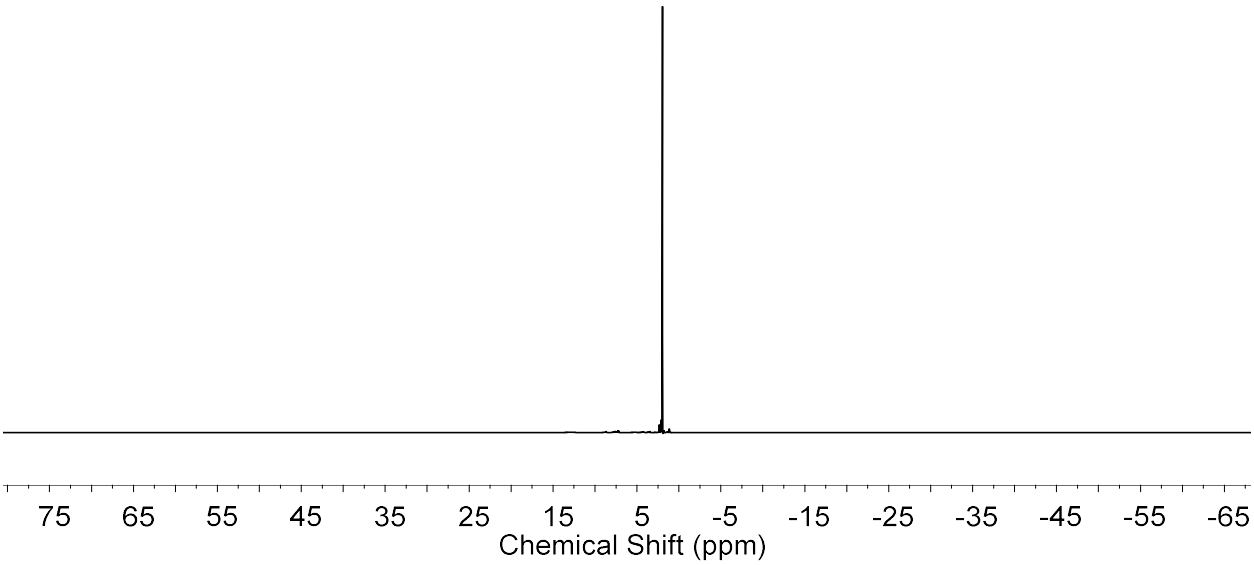

Figure 2.11: ^1H NMR (CD_3CN, 400 MHz) of **6**.

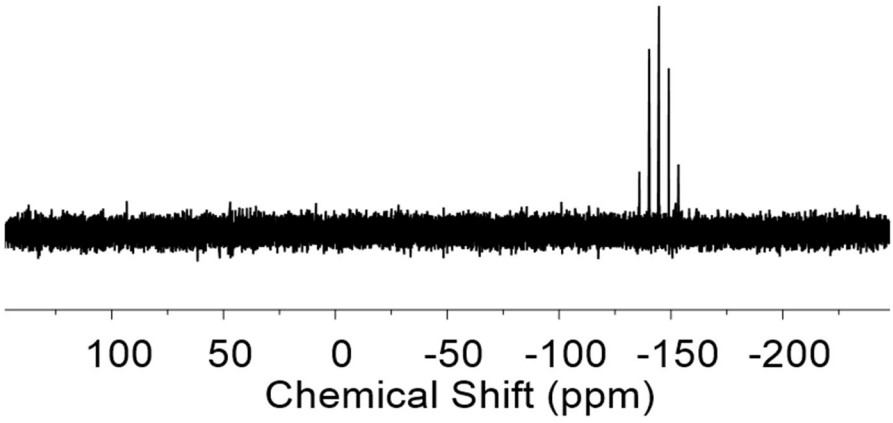

Figure 2.12: $^{31}P\{^1H\}$ NMR (CD_3CN, 162 MHz) of **6**.

The X-band EPR spectrum of **6** (Figure 2.13) shows a distinct signal with axial symmetry (g_1 = 2.18, $g_{2,3}$ = 2.03), confirming that oxidation of **5** with $[Cp^*_2Fe]^+$ generates a paramagnetic species. The relatively small g anisotropy (Δg = 0.15) of the signal suggests that this oxidation is rhodium-centered, as oxidation at the iron center of the dppf ligand would generate a ferrocenium-type system characterized by much broader signals (e.g., for the ferrocenium ion, Δg = 3.08, with g_1 = 4.36 and $g_{2,3}$ = 1.28).[67] The g values observed for **6** are much more consistent with literature values for rhodium(II) systems.[38,68] While the spectrum displays no resolved hyperfine coupling, as would be expected for an unpaired electron on a I = ½ rhodium directly adjacent to two I = ½ phosphorus nuclei, this profile is remarkably similar to that of a rhodium(II) species supported by an arene ligand and two phosphines in pseudo-square planar geometry.[69] We therefore assign the product of oxidation of **5** as $[Cp^*Rh^{II}(dppf)]^+$, consistent with our interpretation of the CV data for **5**. In future work, simulation of the EPR spectrum could provide an explanation for the lack of observable hyperfine or superhyperfine splitting. Furthermore, spectroelectrochemical studies with **5** are planned to confirm that the isolated compound **6** is indeed the product of electrochemical oxidation of **5** at –0.96 V vs. $Fc^{+/0}$.

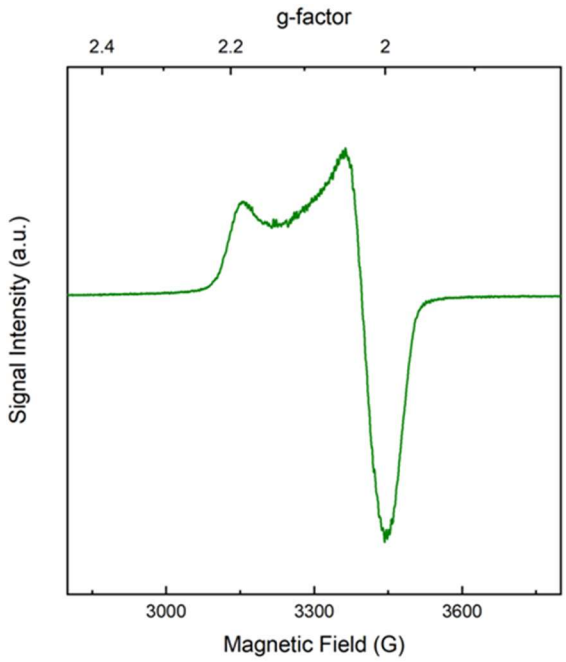

Figure 2.13: X-band EPR spectrum of isolated **6** in toluene (T = 8 K, modulation amplitude = 4.0 G, time constant = 2.56 ms).

Synthesis, NMR Characterization, and Chemical Reactivity of [Cp*Rh(dppf)H][OTf] (7)

We next turned to interrogation of the reactivity of the [Cp*Rh^{I}] complex **5** with a proton source for comparison to the dppb-supported analogue. Addition of a thawing acetonitrile solution of anilinium triflate (pK_a = 18.9 in CH_3CN[6]) to a thawing THF solution of **5** results in lightening of the reaction solution from a dark red-brown to a red-orange. Following workup and extraction with THF, **7** can be isolated as a red-orange solid. While a ^{1}H NMR of **7** free of solvent peaks has not yet been obtained, the preliminary spectrum in Figure 2.14 exhibits a characteristic hydride signal at –11.3 ppm. While the hydride in **3** appears as a quartet with $^1J_{H,Rh} \approx {}^2J_{H,P} \approx 29$ Hz, the hydride peak for **7** is a triplet of doublets with $^1J_{H,Rh}$ = 18.7 Hz and $^2J_{H,P}$ = 32.6 Hz. Inspection of an eventual XRD crystal structure of **7** may help to shed light on the source of this attenuation in coupling to the rhodium center; however, we have not yet grown crystals suitable for diffraction. Meanwhile, the Cp* methyl protons appear as a 15H doublet of triplets (J = 2.9, 1.5 Hz) almost

identical to that observed for **3** ($^{4}J_{H,P}$ = 2.9 Hz, $^{4}J_{H,H}$ = 1.2 Hz). The overlapping peaks in the aromatic region of **5** integrate to a total of 20 protons, as expected for the four phenyl groups of the dppf ligand. Finally, the dppf Cp protons appear as four 2H signals with unresolved splitting at 4.37, 4.31, 4.23, and 4.15 ppm. This pattern is consistent with formation of the C_s piano-stool complex **7**, in which two sets of Cp protons point up toward Cp* and two sets point down toward the hydride, giving rise to four distinct proton environments on the dppf Cp rings. The $^{31}P\{^{1}H\}$ NMR spectrum of **7** (Figure 2.15) is also consistent with formation of the [Cp*Rh^{III}–H] **7**. The lone doublet at 46.43 ppm corresponding to the dppf phosphorus atoms coupling to the I = ½ rhodium nucleus has $^{1}J_{P,Rh}$ = 149.8 Hz, a magnitude characteristic of phosphines bound to Rh(III) centers.

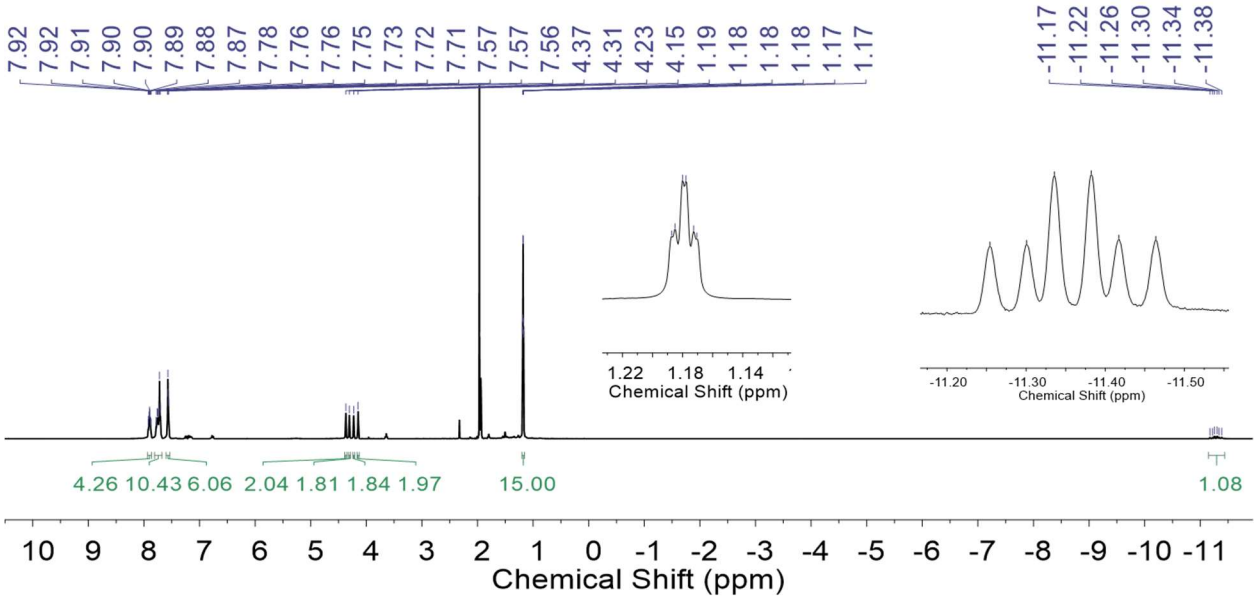

Figure 2.14: ^{1}H NMR spectrum (CD_3CN, 400 MHz) of **7**.

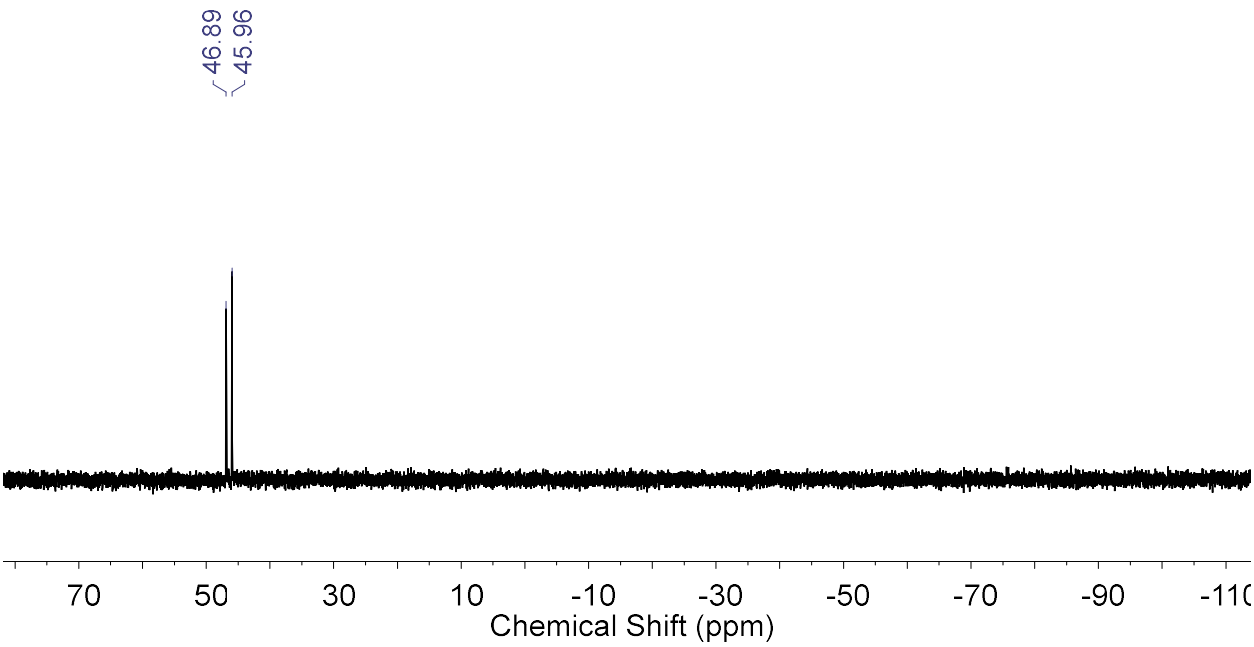

Figure 2.15: $^{31}P\{^{1}H\}$ NMR spectrum (CD_3CN, 162 MHz) of **7**.

Due to the lack of readily available thermochemical constants in THF solvent, we have not calculated the thermodynamic driving force for H_2 evolution from **5** and an acid based on the reduction potential of **5** in THF. However, as observed with the dppb analogue **3**, addition of 1 equiv. of $[DMFH]^+$ (pK_a = 6.1 in CH_3CN) to **7** results in no reactivity over the course of 24 hours (Figure 2.16), indicating that the dppf-supported rhodium-hydride is of comparable stability to the dppb analogue.

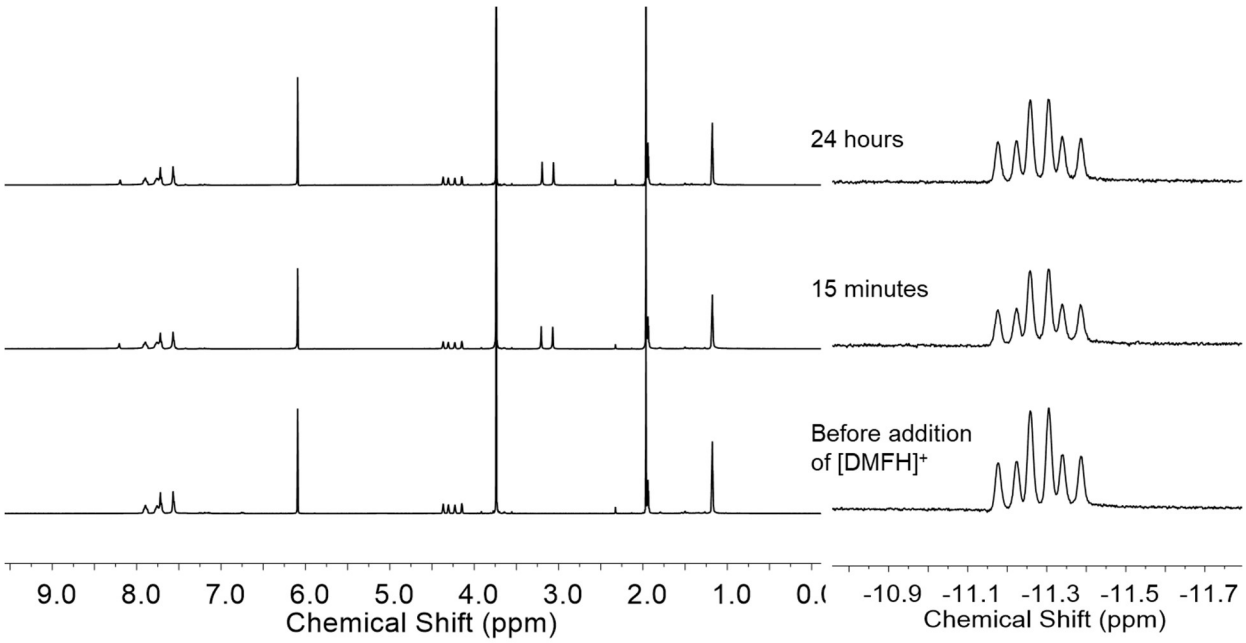

Figure 2.16: ^{1}H NMR spectra (CD_3CN, 400 MHz) of $[DMFH]^+$ additions to **7**. Trimethoxybenzene is also present as an internal standard.

Cyclic Voltammetry of [Cp*Rh(H)(dppf)][OTf] (7)

Like the dppb analogue, **7** is redox-inactive between ca. –0.2 and –1.2 V vs. $Fc^{+/0}$ (black scan in Figure 2.17). Upon scanning further anodically, however, **7** appears to undergo a quasireversible oxidation centered at +0.41 V vs. $Fc^{+/0}$ with ΔE_p = 137 mV. Given the oxidizing potential, this redox activity is almost certainly centered at the Fe center of the dppf ligand. Intriguingly, traversing this seemingly reversible iron-centered couple gives rise to a new cathodic feature with $E_{p,c}$ = –1.01 V vs. $Fc^{+/0}$. Comparison to cyclic voltammetry of **5** identifies this wave as reduction of $[Cp^*Rh^{II}(dppf)]^+$ to $Cp^*Rh^{I}(dppf)$, indicating that oxidation of dppf in **7** stimulates loss of the hydride ligand (which could proceed via homolytic H-atom transfer or heterolytic deprotonation pathways). Indeed, upon close inspection of the redox event at ca. +0.4 V in **7** at varying scan rates (Figure 2.18), a second anodic wave with $E_{p,a}$ = +0.54 V follows the initial oxidation at slower scan rates (50-150 mV s^{-1}). Similarly, at slower scan rate (50 mV s^{-1}) the coupled cathodic wave with $E_{p,c}$ = +0.36 V shows a shoulder at ca. +0.49 V. These secondary anodic and cathodic waves

form a quasireversible process centered at +0.51 V vs. $Fc^{+/0}$, remarkably similar to the midpoint potential of the $Fe^{III/II}$ couple in **5** ($E_{1/2}$ = +0.51 V). The second couple disappears as the scan rate is increased. Taken together, these data suggest that following oxidation of **7**, a chemical reaction occurs that generates $[Cp^*Rh^{III}(dppf)]^{2+}$ which subsequently undergoes oxidation at the dppf ligand at +0.51 V vs. $Fc^{+/0}$. Faster scan rates eclipse the rate of this chemical process, giving rise to a more electrochemically reversible $Fe^{III/II}$ couple. Thus, the potential of this quasireversible event accessed by fast scan rates (+0.41 V) provides a midpoint potential for use in thermochemical determinations. However, further interrogation of the reaction induced by oxidation of **7** via experiments with chemical oxidants is necessary.

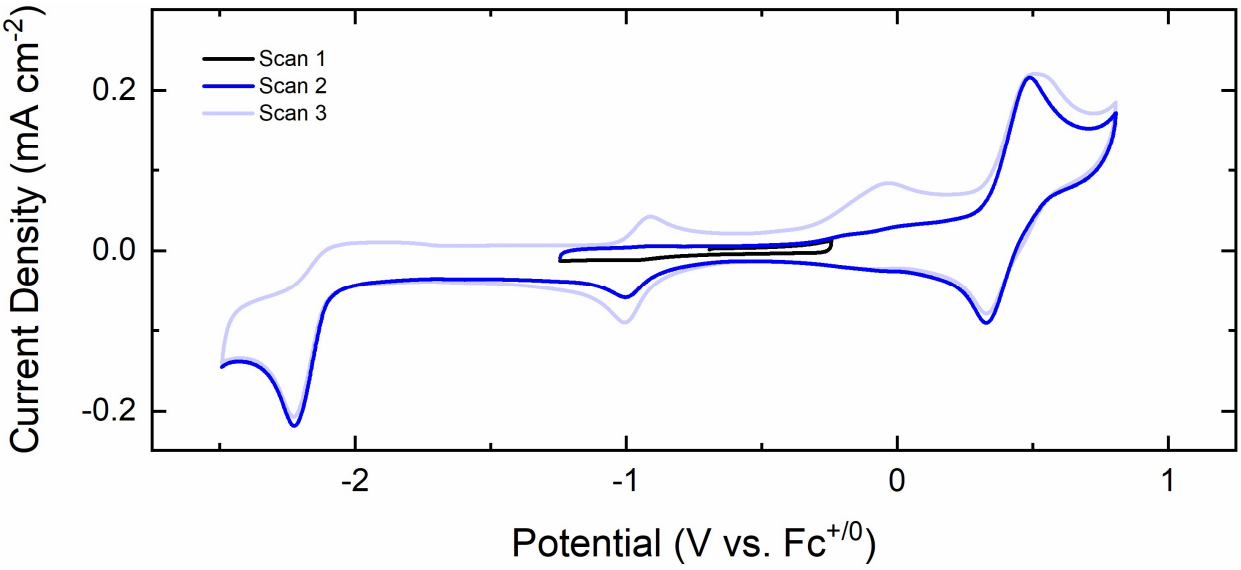

Figure 2.17: Multiple scans of cyclic voltammetry of **7** in THF (electrolyte: 0.1 M $^nBu_4PF_6$) . The initial potential of the voltammogram is at ca. –0.7 V vs. $Fc^{+/0}$. Working electrode: highly oriented pyrolytic graphite; 100 mV s^{-1} scan rate.

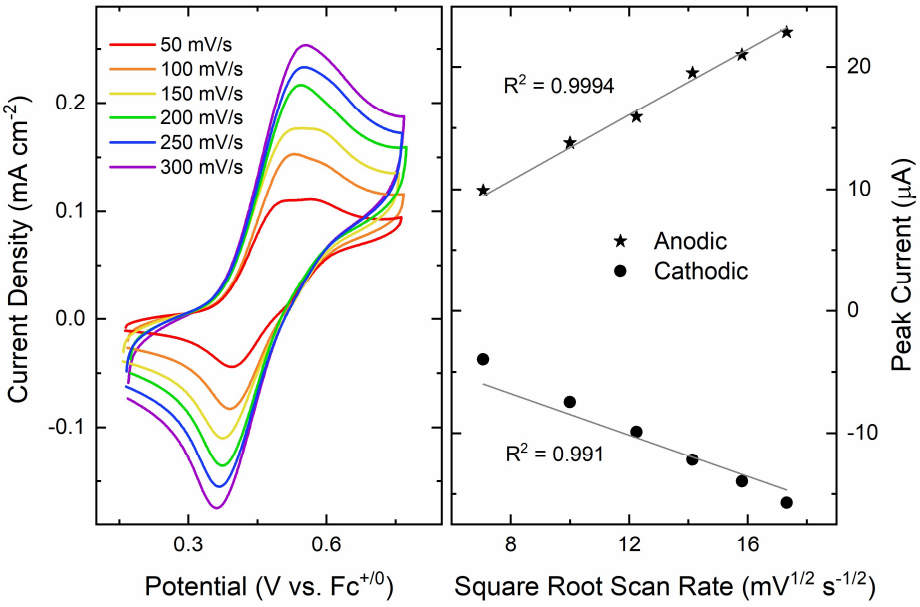

Figure 2.18: Left: cyclic voltammetry of **7** at varying scan rate in THF (0.1 M [^{n}Bu$_4$N][PF$_6$], highly oriented pyrolytic graphite working electrode). The initial potential of all voltammograms is ca. +0.2 V vs. Fc$^{+/0}$. Right: linear dependence of peak cathodic current on square root of scan rate with the y-intercept set to 0.

Meanwhile, scanning to negative potentials with **7** reveals an irreversible 1e$^-$ reduction with $E_{p,c}$ = –2.23 V. Following this reduction, two new anodic waves grow in with $E_{p,a}$ = –0.91 V and –0.01 V, corresponding to the potentials assigned as the Rh$^{II/I}$ and Rh$^{III/II}$ oxidations of **5**, respectively. This profile suggests that the product of 1e$^-$ reduction of **7** reacts to form the [Cp*Rh^I] species **5**. Notably, the presence of the irreversible oxidation at –0.01 V vs. Fc$^{+/0}$ for *in situ*-generated **5** is further evidence that this feature does indeed correspond to redox activity of **5** rather than a persistent impurity. The electrochemical response of **7** at reducing potentials is highly reminiscent of that observed for the dppb analogue **3**. As described in Chapter 1, the irreversibility of 1e$^-$ reduction of **3** is the result of chemical reaction of a transient [Cp*Rh^{II}(dppb)H]^0 species to generate H$_2$ and the corresponding [Cp*Rh^I] complex **2**. Analogous chemical and electrochemical experiments to those performed to characterize the reductive chemistry of **3** will be repeated with

7 to confirm the dppf-supported rhodium-hydride also has access to cathodically-activated mode for hydrogen evolution.

Thermochemical Properties of [Cp*Rh(dppf)H][OTf] (7)

Like in the case of the dppb-supported system, our chemical and electrochemical characterization of **4**, **5**, **6**, and **7** facilitate straightforward determination of the thermodynamic driving force for various reactions on this platform. Figure 2.19 summarizes the experimentally determined free energy changes determined thus far for the ET, PT, and H• transfer reactions involving the dppf-supported complexes. Regrettably, the pronounced insolubility of **5** in CH_3CN (and resulting inability to determine the midpoint potentials for ET pathways involving non-protonated species) mandates that all values relevant to thermochemical determinations be obtained in THF. Thus, it is important to emphasize that the *BDFE* and pK_a values for the dppf-supported species in THF cannot be directly compared to those for the dppb analogues in CH_3CN. We have not yet obtained a literature value for the free energy of formation and solvation of H^- from one proton and two electrons in THF solution, precluding determination of hydricity from a pK_a and two reduction potentials; thus, we are currently exploring alternative routes for determining the ΔG_{H^-} values in Figure 2.19.

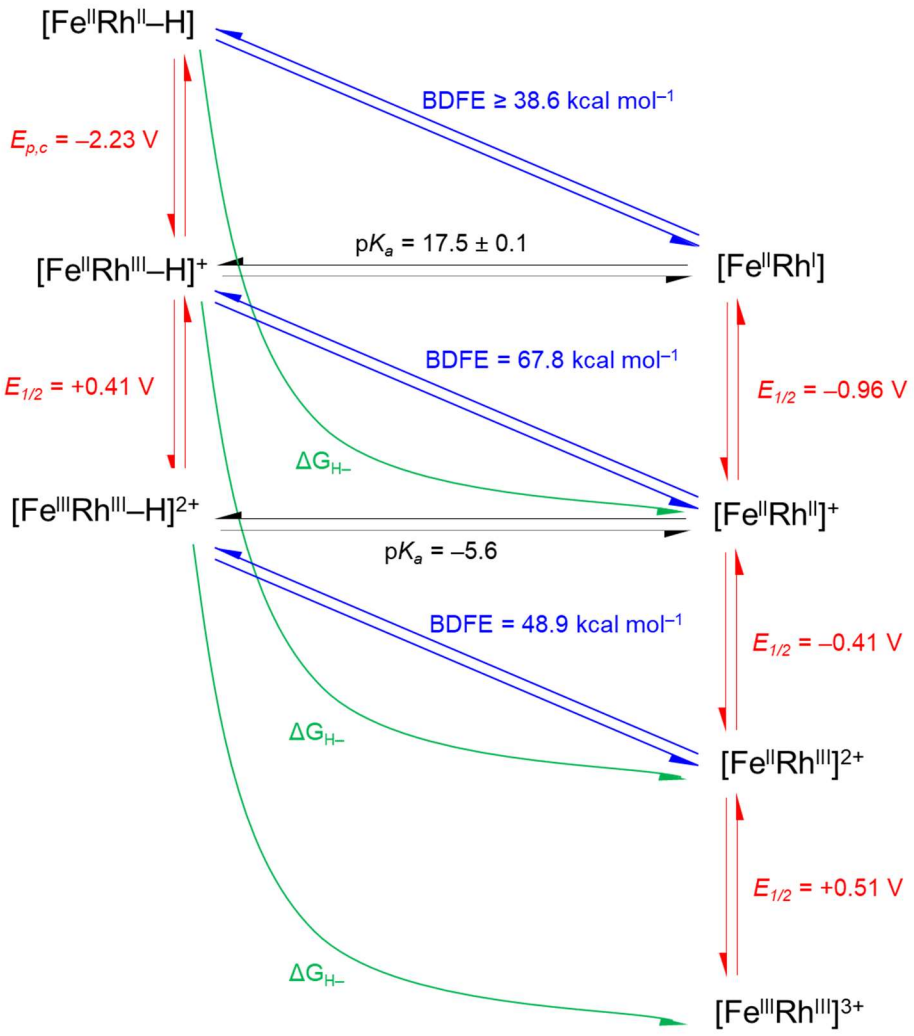

Figure 2.19: Thermochemical "square" scheme for the [Cp*Rh(dppf)] system.

Determination of the redox potentials associated with the vertical ET steps in Figure 2.19 has been discussed in detail previously in this chapter. To summarize, non-protonated **5** has two well-defined quasireversible redox couples in cyclic voltammetry corresponding to $Rh^{II/I}$ and $Fe^{III/II}$ processes ($E_{1/2}$ = –0.96 V and +0.41 V vs. $Fc^{+/0}$, respectively). The midpoint potential for the $Rh^{III/II}$ couple of **5** carries more uncertainty; the potential listed corresponds to the midpoint potential of the second oxidation of **5** at –0.01 V vs. $Fc^{+/0}$ and the cathodic feature at –0.82 V vs. $Fc^{+/0}$ which appears to result from the second oxidation. Because our explanation for this exceptionally large

peak-to-peak separation relies heavily on the importance of solvent binding (i.e., the solvent binding constant for a $[Cp^*Rh^{II}(dppf)]^+$ species is much smaller than that for a $[Cp^*Rh^{III}(dppf)]^{2+}$ species in THF), failure to account for solvent coordination in the equilibrium between $[Cp^*Rh^{II}(dppf)]^+$ and $[Cp^*Rh^{III}(dppf)(THF)]^{2+}$ might give rise to large errors in determination of the free energy change associated with this step. Thus, any thermochemical parameters dependent on this value (i.e., the *BDFE* of the oxidized form of **7** (**7**$^+$)) are, at best, approximations. **7** exhibits one quasireversible $Fe^{III/II}$ couple centered at +0.41 V vs. $Fc^{+/0}$. However, 1e$^-$ reduction of **7** is fully irreversible even at fast scan rates (0.5 V s^{-1}), necessitating reliance on the peak cathodic potential. As such, calculations with this value produce lower bounds for the true *BDFE* and hydricity of the reduced form of **7** (**7**$^-$).

The pK_a of **7** was determined by a titration experiment analogous to that described for **3**: varying volumes of neat triethylamine (pK_a $[Et_3NH]^+$ = 14.9 in THF[70]) were added to a solution of **7** and the absorbance of the resulting solution was monitored at 290 nm. Whereas **2** and **3** have a window where one complex absorbs strongly but the other does not, **7** and **5** have qualitatively similar electronic absorption profiles (see Figures 2.20 and 2.21). However, it is possible to derive an equation to calculate the concentration of one species based on total absorbance at a wavelength where the extinction coefficients ε for both species are known:[71]

$$[Rh^I] = \frac{A - \varepsilon_H[Rh]_{tot}}{\varepsilon_{RhI} - \varepsilon_H} \quad (31)$$

In eq. 5, A is the absorbance at a given wavelength of a mixture of $[Rh^I]$ and [Rh–H] species, $[Rh]_{tot}$ is the total concentration of rhodium-containing species, and ε_H and ε_{RhI} are the molar absorptivities of the [Rh–H] and $[Rh^I]$ species, respectively, at that wavelength. Based on precisely determined molar absorptivities for **5** and **7** at 290 nm, where the spectra of **5** and **7** show the best separation, we determined the concentration of **5** generated in the presence of a varying number of equivalents

of base (Figure 2.22). With these values we found the pK_a of **7** to be 17.5 ± 0.1 in THF. While this value cannot be directly compared to the pK_a of **3** in CH_3CN, by extrapolating the difference in pK_a for triethylammonium in each solvent ($\Delta pK_a \approx 4$) to the rhodium-hydride we can estimate the pK_a of **7** to be ca. 21 in CH_3CN, quite similar to the pK_a of **3** (20.0 ±0.1).

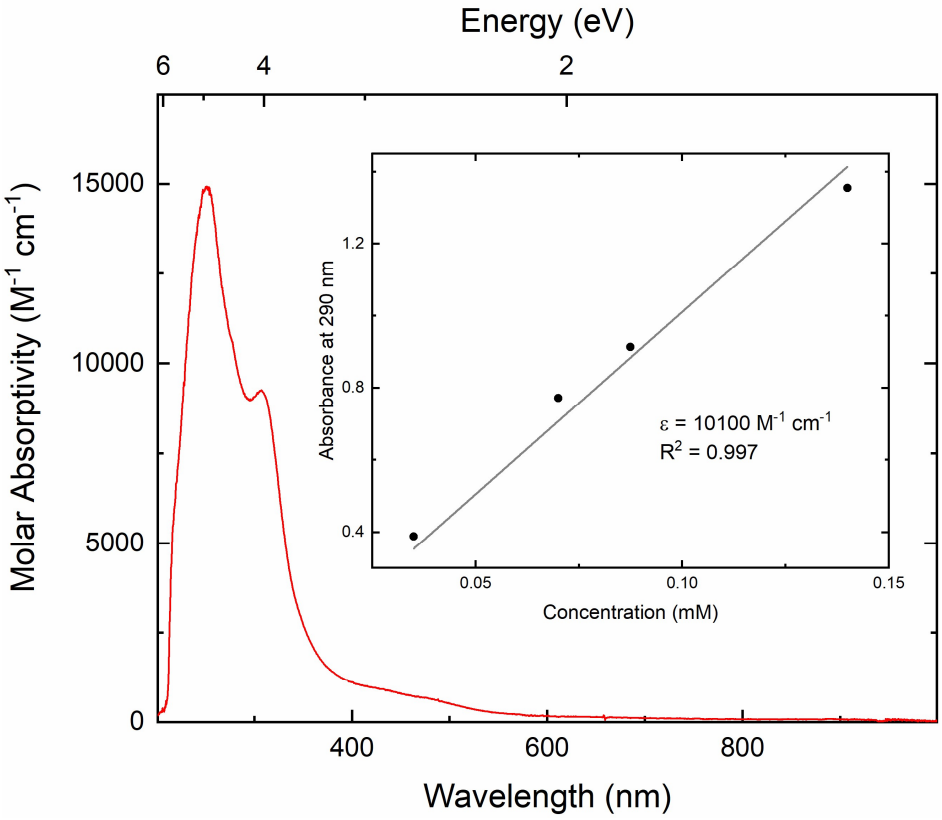

Figure 2.20: Electronic absorption spectrum of **7** in THF. The inset shows a plot of absorbance at 290 nm vs. concentration used to calculate molar absorptivity at this wavelength for use in pK_a determinations.

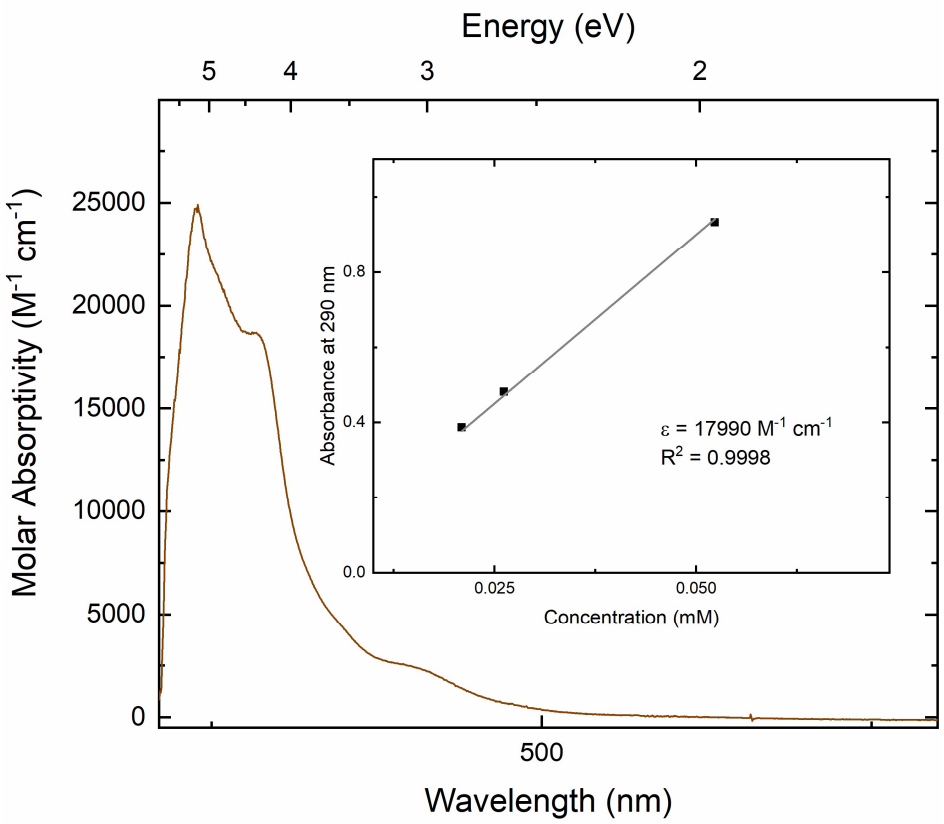

Figure 2.21: Electronic absorption spectrum of **7** in THF. The inset shows a plot of absorbance at 290 nm vs. concentration used to calculate molar absorptivity at this wavelength for use in pK_a determinations.

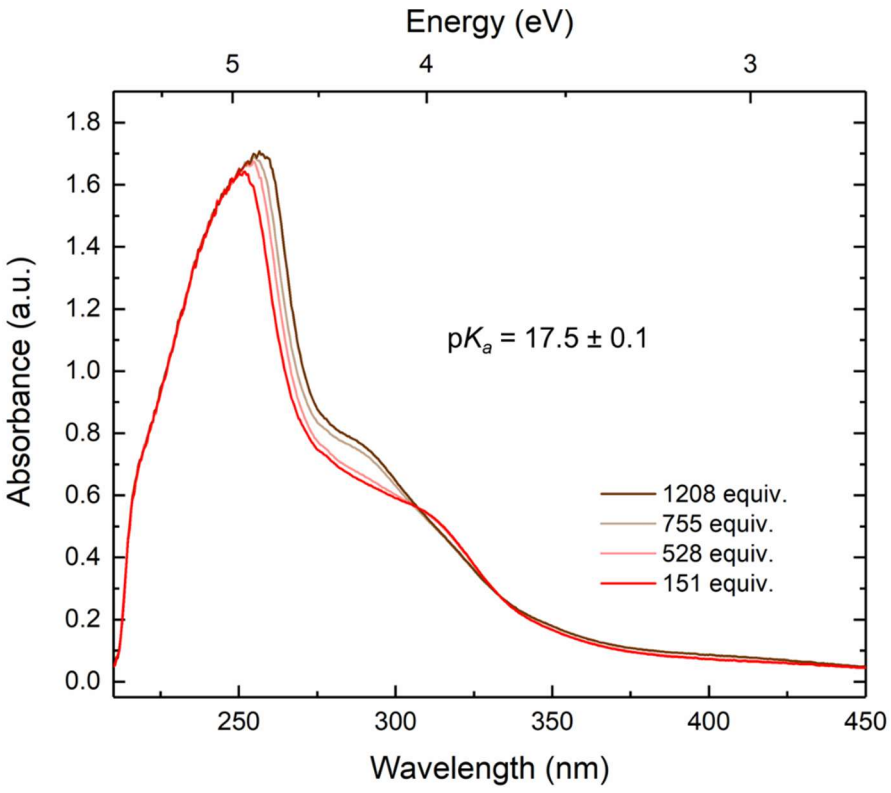

Figure 2.22: Electronic absorption data for addition of Et_3N to **7** in THF to determine pK_a. $[\mathbf{7}]_i$ = 0.04 mM.

With all of these experimental data, we can determine the additional thermochemical values laid out in Figure 2.19. Using the established value of 66 kcal mol^{-1} as the constant for formation of H• in THF solution,[72] the *BDFE* of **7** can be determined reliably. A lower bound for the *BDFE* of **7**$^-$ can also be obtained based on the peak cathodic potential of 1e$^-$ reduction of **7**. As observed in the dppb analogue **3**, metal-centered reduction of the [Cp*Rh^{III}–H] results in a substantial weakening of the Rh–H bond; in both cases, the decrease in *BDFE* upon reduction is ca. –30 kcal mol^{-1}. The *BDFE* of **7**$^+$ depends both on a pK_a calculated from other thermochemical parameters (*vide infra*) rather than one measured directly and on the non-protonated (Rh$^{III/II}$) potential, a quantity which remains somewhat uncertain; further experiments are therefore necessary to assess the validity of the *BDFE* value listed for **7**$^+$ in Table 2.1.

Table 2.1: Thermodynamic driving force for homolytic H_2 evolution from the [Cp*Rh] monohydride **7** and its oxidized and reduced forms.

Species	*Metal Oxidation States*	*BDFE* [a]	$\Delta G^{o}_{HER,homolytic}$ [a]
7	$[Fe^{II}Rh^{III}]^{+}$	67.8	28.7
$\mathbf{7}^{+}$	$[Fe^{III}Rh^{III}]^{2+}$	48.9	–9.1
$\mathbf{7}^{-}$	$[Fe^{II}Rh^{II}]$	≥ 38.6	≥ –29.7

[a] kcal mol^{-1}.

Eq. 14 can be rearranged to solve for the pK_a of $\mathbf{7}^{+}$ with the *BDFE* of **7** and the reversible potential for oxidation of **7** at +0.41 V vs. $Fc^{+/0}$. The resulting value is –5.6, indicating an increase in the acidity of the Rh–H bond by 23 orders of magnitude following $1e^{-}$ oxidation of the iron center in the dppf ligand. This result suggests that the analogous value in the dppb system, for which an upper bound of an increase of ca. 30 pK_a units was determined based on the irreversible anodic peak potential of the dppb-supported rhodium hydride, is not a gross overestimation. Ligand-centered oxidation of [Cp*RhH(diphosphine)] species therefore appears to give rise to dramatic acidification of the rhodium-hydride bond, indicative of significant depletion of electron density at the rhodium center. This is in good agreement with the work of Mirkin and coworkers with rhodium(I) complexes supported by redox-active hemilabile ligands containing the ferrocenyl moiety; upon oxidation of their ligand, the binding constant of acetonitrile to the rhodium center increased by 7 orders of magnitude.[73]

As alluded to previously, THF is a less common solvent for thermochemical studies, resulting in a lack of readily available literature values for important constants such as the free energy associated with breaking down H_2 into two solvated hydrogen atoms (eq. 34 in Scheme 2.3), which is required to calculate the thermodynamic driving force for homolytic hydrogen evolution from a compound for which a *BDFE* has been measured (see Scheme 1.7). However, using the free energy of formation of H_2 from hydrogen atoms in the gas phase (eq. 32),[74] tabulated solubility values for H_2 in THF,[75] and the well-accepted assumption that the solvation energy of H_2 is approximately

equal to that of H•,[76] this necessary value (which is equivalent to the *BDFE* of H_2 in THF) can be derived (see Scheme 2.3).

$$H_{2(g)} \rightleftharpoons 2H\bullet_{(g)} \qquad \Delta G^{o} = 97.2 \text{ kcal mol}^{-1} \qquad (32)$$

$$2H\bullet_{(g)} \rightleftharpoons 2H\bullet_{(solv)} \qquad \Delta G^{o}_{THF} = 9.7 \text{ kcal mol}^{-1} \qquad (33)$$

$$H_{2(g)} \rightleftharpoons 2H\bullet_{(solv)} \qquad BDFE_{H2,THF} = 106.9 \text{ kcal mol}^{-1} \qquad (34)$$

Scheme 2.3: Derivation of *BDFE* of H_2 in THF.

With the *BDFE* of H_2 in THF in hand, we can calculate the driving force for homolytic H_2 evolution from **7** and its oxidized and reduced forms (**7**$^+$ and **7**$^-$). The results are summarized in Table 2.1. Qualitatively, the thermodynamically favorable reactivity pathways of **7** are identical to those of **3**; the initial [$Fe^{II}Rh^{III}$–H] species are inert to homolytic hydrogen evolution, consistent with the observed long-term stabilities of these isolated complexes. In both ligand frameworks, 1e$^-$ reduction at the rhodium center weakens the Rh–H bond substantially enough to favor hydrogen evolution. However, the predicted spontaneity is significantly more extreme in the dppb case ($\Delta G^{o}_{HER,homolytic}$ = –41.5 kcal mol^{-1}), especially considering the driving force in the dppf system is likely less favorable than the lower bound listed in Table 2.1 ($\Delta G^{o}_{HER,homolytic} \geq$ –29.7 kcal mol^{-1}). Analysis of the source of this change reveals that it stems primarily from the different solvent systems, specifically from the difference in the constant associated with formation of H• in each solvent. This result illustrates the necessity that thermodynamic values like *BDFE* not be compared directly across solvents, and suggests that in this system, use of acetonitrile as solvent might promote reactivity. Intriguingly, while the homolytic HER reaction from reduced **3** is more thermodynamically favorable than from reduced **7**, the irreversibility of the corresponding electrochemical reduction waves (indicative of the rate of chemical reaction of the reduced species) is more pronounced in **7** (compare Figure 2.17 to 1.21). Counter to the thermodynamic driving

force, reactivity with reduced **7** may be more kinetically favored compared to the case of reduced **3**.

Conclusions and Future Directions

Protonation of Cp*Rh(dppf) results in formation of $[Cp^*Rh(dppf)H]^+OTf^-$, providing just the second example of a diphosphine-supported rhodium monohydride to contrast with the many examples of protonated Cp* complexes of the type $[(Cp^*H)Rh(diimine)]^+$. Like the analogous $[Cp^*Rh(dppb)H]^+$ described in Chapter 1, the rhodium-hydride bond in the dppf complex is inert to reaction to generate H_2 with even a strong acid such as $[DMFH]^+$. However, the isolated hydride undergoes both an irreversible $1e^-$ reduction at –2.23 V and a quasireversible oxidation at +0.41 V vs. $Fc^{+/0}$. The metal-centered reduction gives rise to a ca. 30 kcal mol^{-1} decrease in the *BDFE* of the Rh–H moiety, suggesting that the reduced rhodium hydride likely undergoes a similar homolytic H_2 evolution reaction to that observed with the dppb analogue. The reversibility of the dppf $Fe^{III/II}$ couple in the hydride **7** provides access to accurate thermochemical determinations of the effect of ligand-centered oxidation in this system. We find that oxidation of dppf results in acidification of the Rh–H bond by 23 orders of magnitude, indicating that the oxidation state of the ligand has a dramatic effect on the electron density at the rhodium center.

Given these findings, an interesting next step would be study of the cobaltocene analogue to the dppf ligand (i.e., bis-(diphenylphosphino)cobaltocenium, dppc).[77] As described for the dppb system, homolytic hydrogen evolution from the reduced hydride species is much more thermodynamically favorable than CO_2 hydrogenation; however, it is possible to derive the conditions under which the reverse would be true. A key result of this derivation is that a small potential difference between the $Rh^{II/I}$ couple of the non-protonated species and the first reduction of the protonated species favors CO_2 hydrogenation over hydrogen evolution. Because cobaltocene

undergoes reductive chemistry rather than the oxidative processes of dppf, $1e^-$, ligand-centered reduction of a proposed $[Cp^*Rh(dppc)H]^{2+}$ species would be accessible at a much less negative potential than the rhodium-centered reductions of dppb- and dppf-supported rhodium-hydrides. Thus, preparation and development of the analogous the [Cp*Rh(dppc)] system could represent an attractive strategy to target selective electrocatalytic CO_2 hydrogenation.

Appendix 1

GENERAL CONSIDERATIONS

All manipulations were carried out in dry N_2-filled gloveboxes (Vacuum Atmospheres Co., Hawthorne, CA) or under N_2 atmosphere using standard Schlenk techniques unless otherwise noted. All solvents were of commercial grade and dried over activated alumina using a PPT Glass Contour (Nashua, NH) solvent purification system prior to use, and were stored over molecular sieves. All chemicals were from major commercial suppliers and used as received after extensive drying. $[Cp^*RhCl_2]_2$ was prepared according to literature procedure.[78] Deuterated NMR solvents were purchased from Cambridge Isotope Laboratories; CD_3CN was dried over CaH_2 and C_6D_6 was dried over sodium/benzophenone. ^1H, ^{13}C, ^{19}F, and ^{31}P NMR spectra were collected on 400 or 500 MHz Bruker spectrometers. For ^1H and ^{13}C NMR, chemical shifts (δ) are referenced to $(CH_3)_4Si$ (TMS). Referencing to TMS was carried out by reporting relative to the chemical shift of the residual protio-solvent signal in CD_3CN and C_6D_6 in the case of ^1H spectra and the chemical shift of the deuterated solvent itself ($\underline{C}D_3CN$, $\underline{C}_6D_6$) in the case of ^{13}C spectra.[79] Heteronuclear NMR spectra were referenced to the appropriate external standard following the recommended scale based on ratios of absolute frequencies (Ξ).[80,81] ^{19}F NMR spectra are reported relative to CCl_3F, and ^{31}P NMR spectra are reported relative to 85% aqueous H_3PO_4. Chemical shifts are reported in units of ppm and coupling constants (*J*) are reported in Hz. Electronic absorption spectra were collected with an Ocean Optics Flame spectrometer, in a 1-cm pathlength quartz cuvette. Elemental analyses were performed by Midwest Microlab, Inc. (Indianapolis, IN).

Appendix 2

ADDITIONAL NMR CHARACTERIZATION

2D NMR Analysis and Supplemental Heteronuclear Spectra of 1

As shown by the dotted lines in Figure A2.1, the three most upfield ^{1}H NMR signals of **1** share COSY cross peaks and must therefore represent the three proton environments on one set of phenyl groups. The triplet (J = 7.7 Hz) at 7.29 ppm is coupled to the multiplet at 6.91 ppm as well as the triplet (J = 7.6 Hz) at 7.53 ppm. Because the triplet at 7.53 ppm only integrates to two protons, it must correspond to the protons *para* to the phosphorus atoms. The four-proton triplet must represent the protons *meta* to the phosphorus atoms because it shows coupling to both other signals. This leaves the multiplet as the protons *ortho* to the phosphorus atoms. Identical reasoning was used to assign the 4-proton triplet (J =7.6 Hz) at 7.61 ppm, the 2-proton triplet (J = 7.9 Hz) at 7.72 ppm, and the 4-proton multiplet at 7.82 ppm as the *meta*, *para*, and *ortho* protons on the other set of phenyl groups. Finally, the 2-proton multiplets at 7.64 ppm and 7.77 ppm couple to each other and must correspond to the benzyl protons 12 and 13.

As shown in the NOESY spectrum in Figure A2.2, the Cp* ligand of **1** shows a cross peak with the multiplet at 6.91 ppm but not with the multiplet at 7.82 ppm, meaning the more upfield set of phenyl protons is tilted closer to the Cp* methyl groups in space and can be assigned to protons 4, 5, and 6. Meanwhile, the more downfield phenyl protons can be assigned as protons 7, 8, and 9. Similarly, in the boxed section of the same NOESY spectrum in Figure A2.3, one of the *ortho* phenyl protons shows a cross peak with the multiplet at 7.77 but not with the multiplet at 7.64 ppm, indicating that the more downfield multiplet is closer to the phenyl groups and can be assigned as proton 12 while the multiplet at 7.64 ppm corresponds to proton 13.

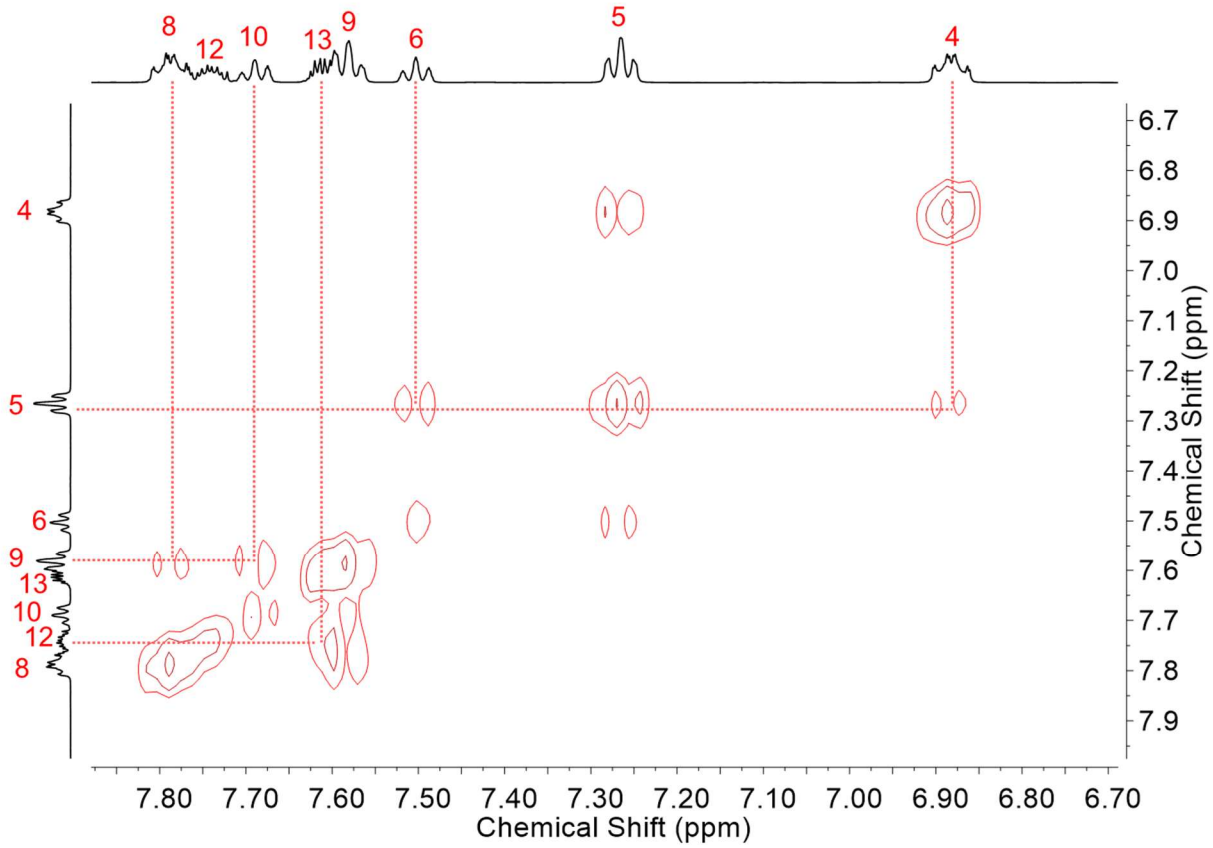

Figure A2.1: Aromatic region of ^{1}H COSY spectrum (500 MHz, CD_3CN) of **1**.

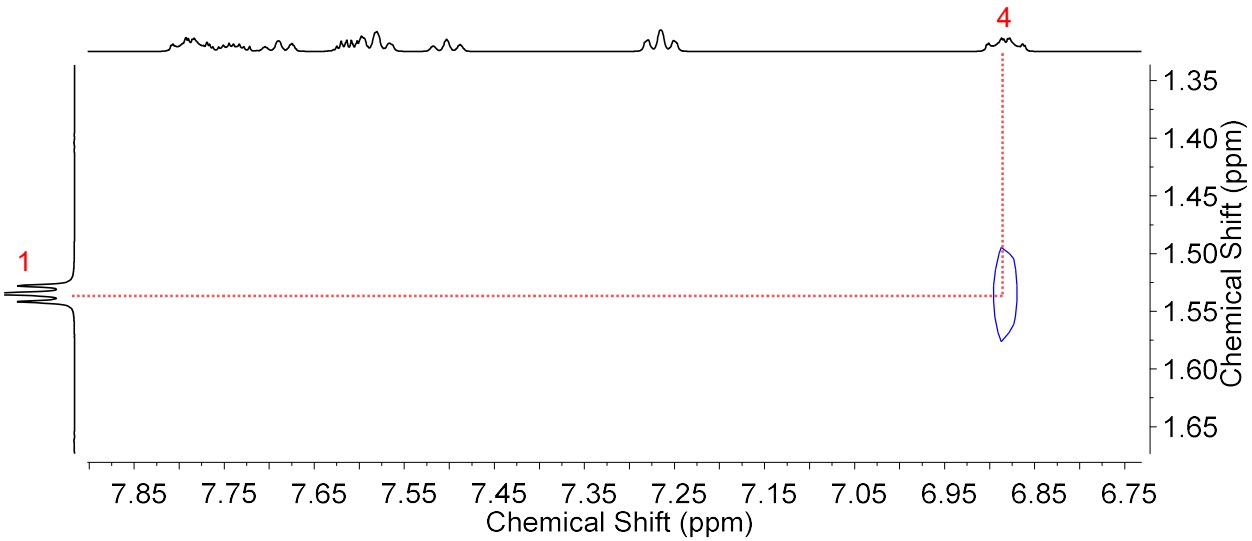

Figure A2.2: Abbreviated ^{1}H NOESY spectrum (500 MHz, CD_3CN) of **1**.

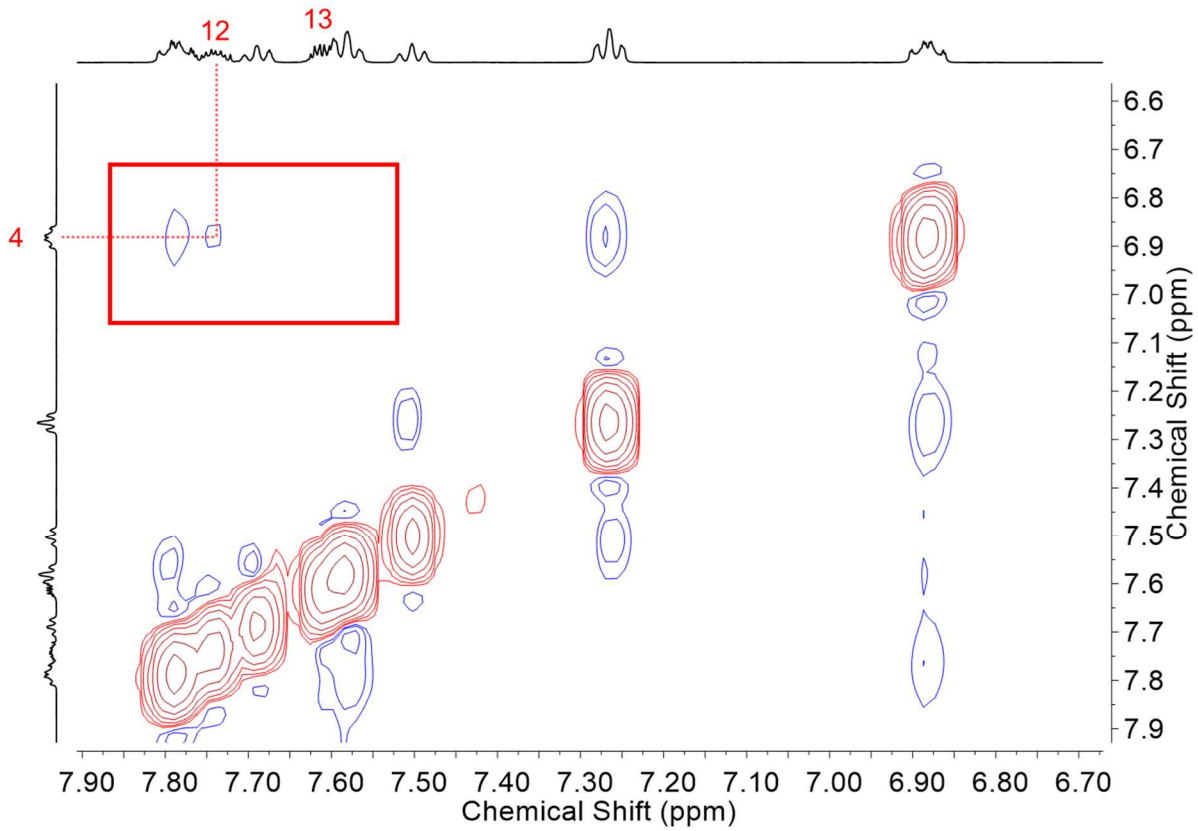

Figure A2.3: Aromatic region of ^{1}H NOESY spectrum (500 MHz, CD_3CN) of **1**.

Because the triplet ($^{3}J_{C,P}$ = 1.5 Hz) at 7.89 ppm in the $^{13}C\{^{1}H\}$ spectrum of **1** has an HSQC cross peak with the methyl protons of **1** (Figure A2.4), it can be assigned as the methyl carbons in the Cp* ring (i.e., carbon 1). The *ortho* and *meta* protons of both the "up" and "down" phenyl groups are coupled to the signals in the $^{13}C\{^{1}H\}$ NMR at 134.22, 132.49, 128.04, and 127.65 ppm, allowing these peaks to be assigned as carbons 8, 4, 5, and 9, respectively. The clear cross peak between the *para* proton of the "up" phenyl groups and the carbon signal at 131.18 ppm identifies this peak as carbon 6. The blue lines in Figure A2.4 indicate that all of the aromatic protons of **1** exhibit cross peaks in this region, indicating that the missing peaks for carbons 10, 12, and 13 are indeed present as overlapping signals. The HMBC spectrum of **1** (Figure A2.5) shows a cross peak between one of the benzene proton signals and the weak multiplet at 139.8 ppm, which can

therefore be identified as the quaternary benzene carbon 11. Similarly, the weak doublet at 125.98 ppm has a cross peak with the *meta* protons of the choride-oriented phenyl rings while the multiplet at approximately 128.2 ppm that is nearly obscured by the peak for carbon 5 has a cross peak with the *meta* protons of the Cp* oriented phenyl rings, allowing these two signals to be assigned as carbons 7 and 3, respectively.

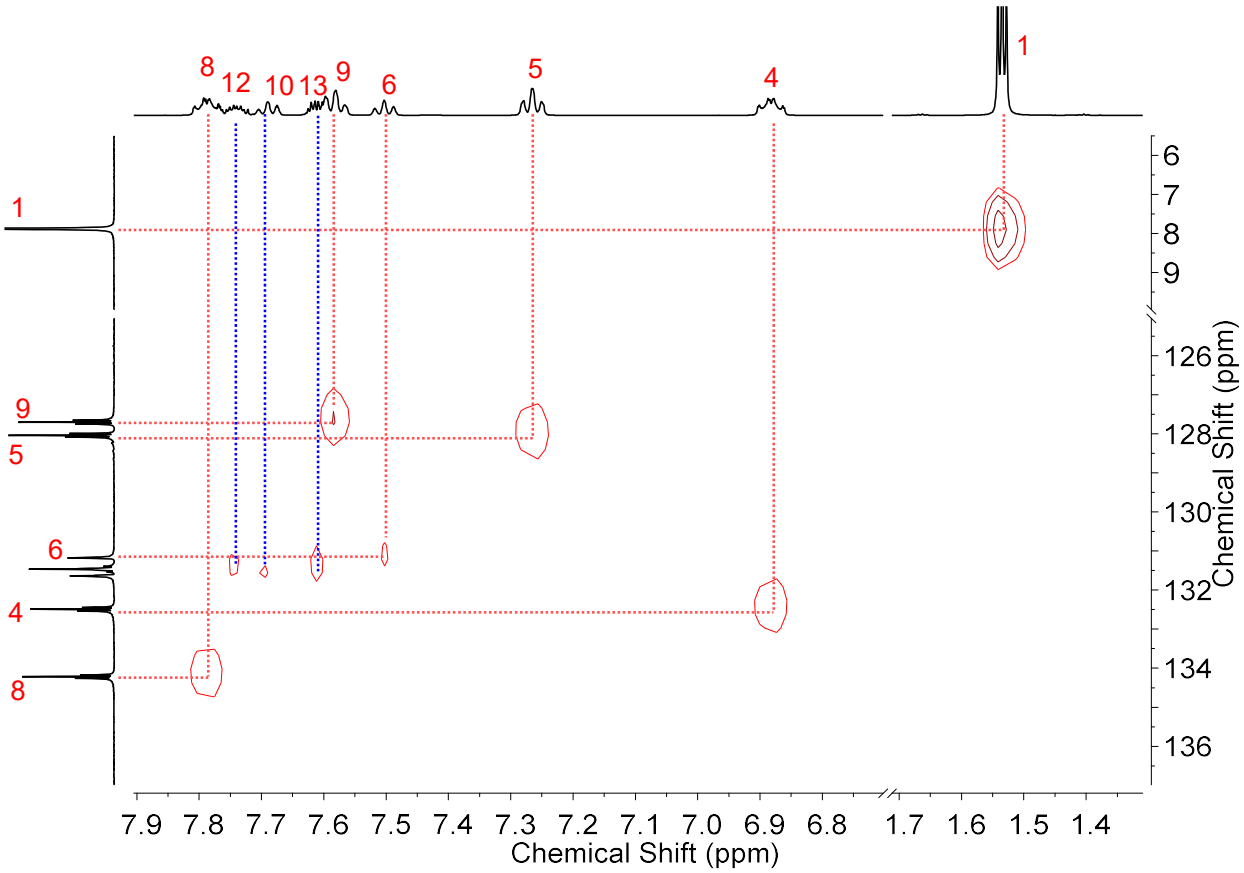

Figure A2.4: Abbreviated $^{1}H - ^{13}C\{^{1}H\}$ HSQC spectrum (500 – 126 MHz, CD_3CN) of **1**.

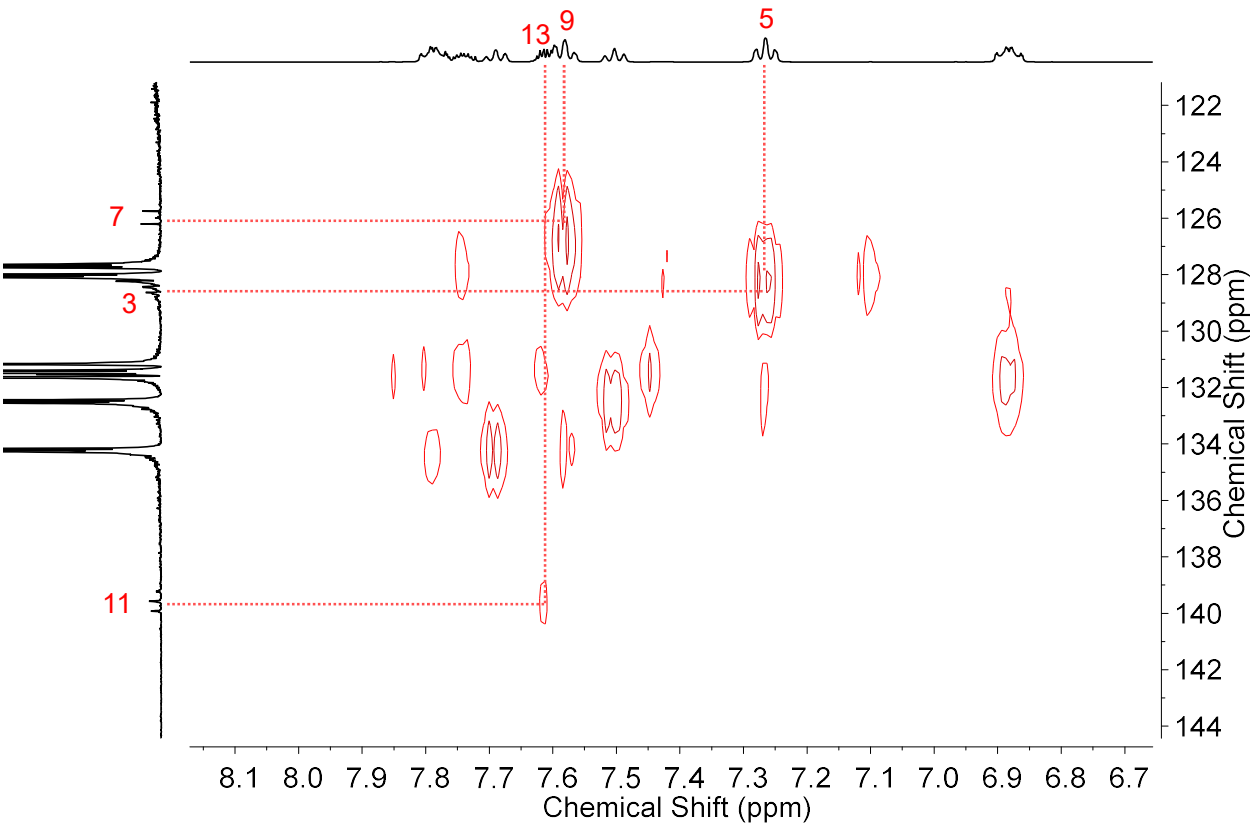

Figure A2.5: Aromatic region of the $^{1}H - {}^{13}C\{^{1}H\}$ HMBC spectrum (500 – 126 MHz, CD_3CN) of **1**.

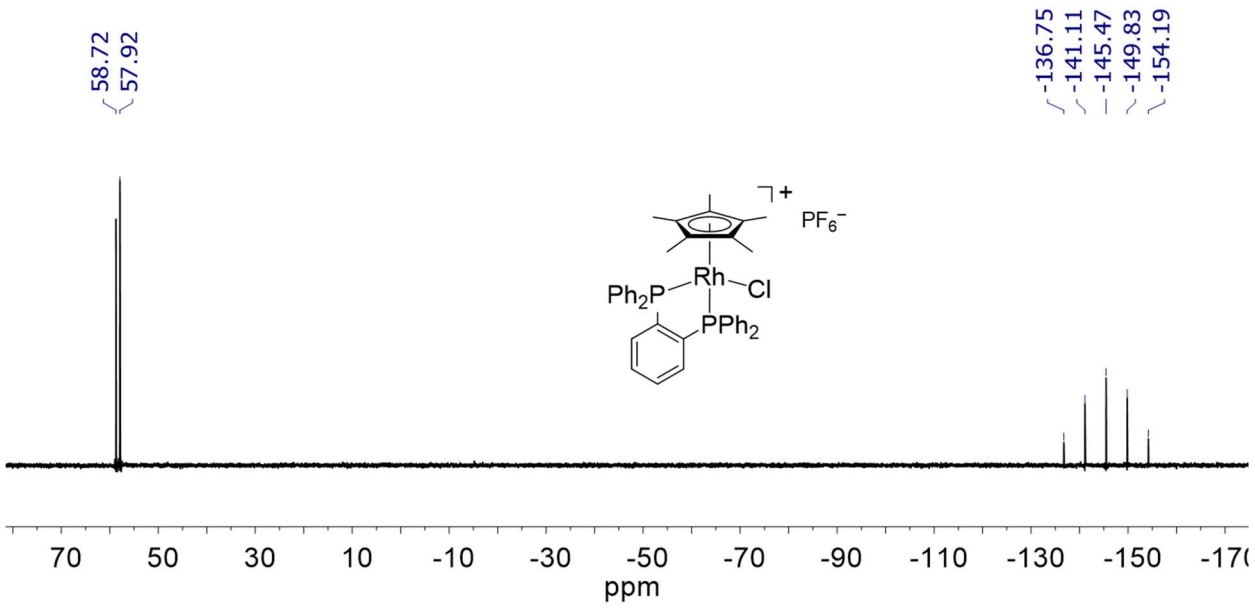

Figure A2.6: $^{31}P\{^{1}H\}$ NMR spectrum (162 MHz, CD_3CN) of **1**.

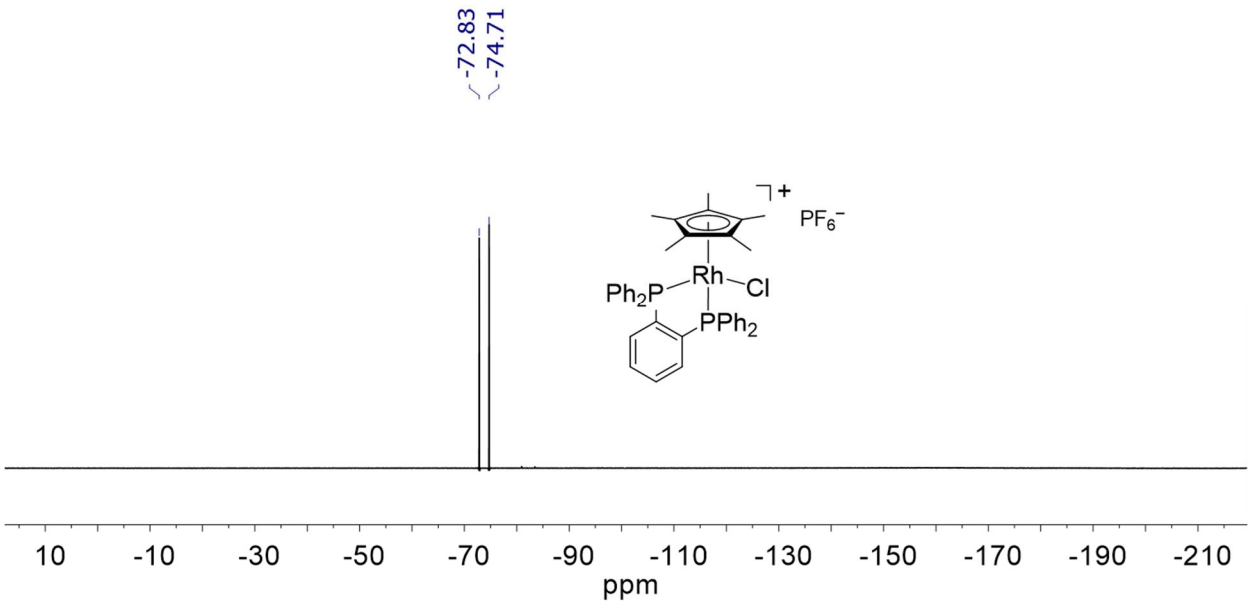

Figure A2.7: ^{19}F NMR spectrum (376 MHz, CD_3CN) of **1**.

Full Assignment Rationale and 2D NMR Analysis of 2

Given the distinct similarities in the aromatic peak shapes of **2** compared to **1**, we can assign the 8-proton multiplet at 7.79 ppm in Figure 1.8 as the *ortho* position (proton 4); the triplet (J = 7.4 Hz) at 7.13 ppm which is partially obscured by the solvent residual peak as the *meta* position (proton 5); and the 4-proton triplet (J = 7.5 Hz) at 7.05 ppm as the *para* position (proton 6). By NOESY (Figure A2.8), the 2-proton multiplet at 7.52 ppm shows a cross peak with the *ortho* protons of the phenyl groups and can therefore be assigned as the protons adjacent to the phosphorus substituents of the benzyl bridge (proton 8), leaving the second proton environment of the benzyl bridge (proton 9) as the 2-proton multiplet at 6.81 ppm.

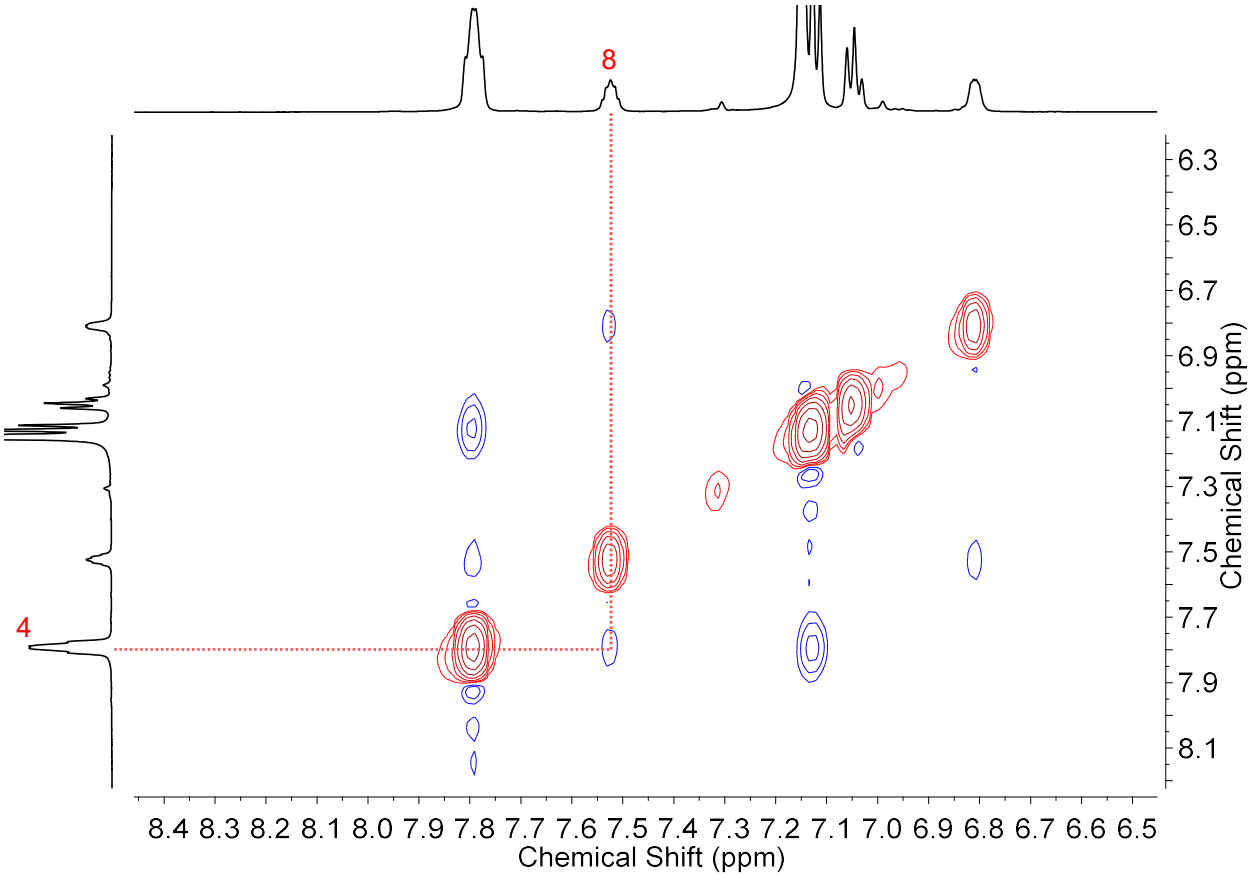

Figure A2.8: Aromatic region of ^{1}H NOESY spectrum (500 MHz, C_6D_6) of **2**.

The 6 proton environments of **2** are clearly correlated to six of the $^{13}C\{^{1}H\}$ signals in Figure 1.10 via HSQC (Figure A2.9), allowing these signals to be assigned as follows: the triplet (J = 6.4 Hz) at 133.37 ppm is the *ortho* carbons of the phenyl rings; the less intense triplet (J = 9.3 Hz) at 130.27 is the carbons adjacent to the phosphorus atoms on the benzyl bridge; the singlet at 129.10 ppm is the benzyl carbons farthest from the phosphorus atoms, as is suggested by the lack of coupling; the singlet at 128.75 ppm is the *para* carbons of the phenyl rings; and the signal at 128.75 that is almost obscured by the C_6D_6 peak is the *meta* carbons. Finally, the quaternary carbons of the phenyl and benzyl rings can be identified by HMBC (Figure A2.10): the upfield triplet (J = 48 Hz) at 150.00 ppm corresponds to the benzyl quaternary carbons while the triplet (J = 18 Hz) at 149.62 ppm corresponds to the phenyl quaternary carbons.

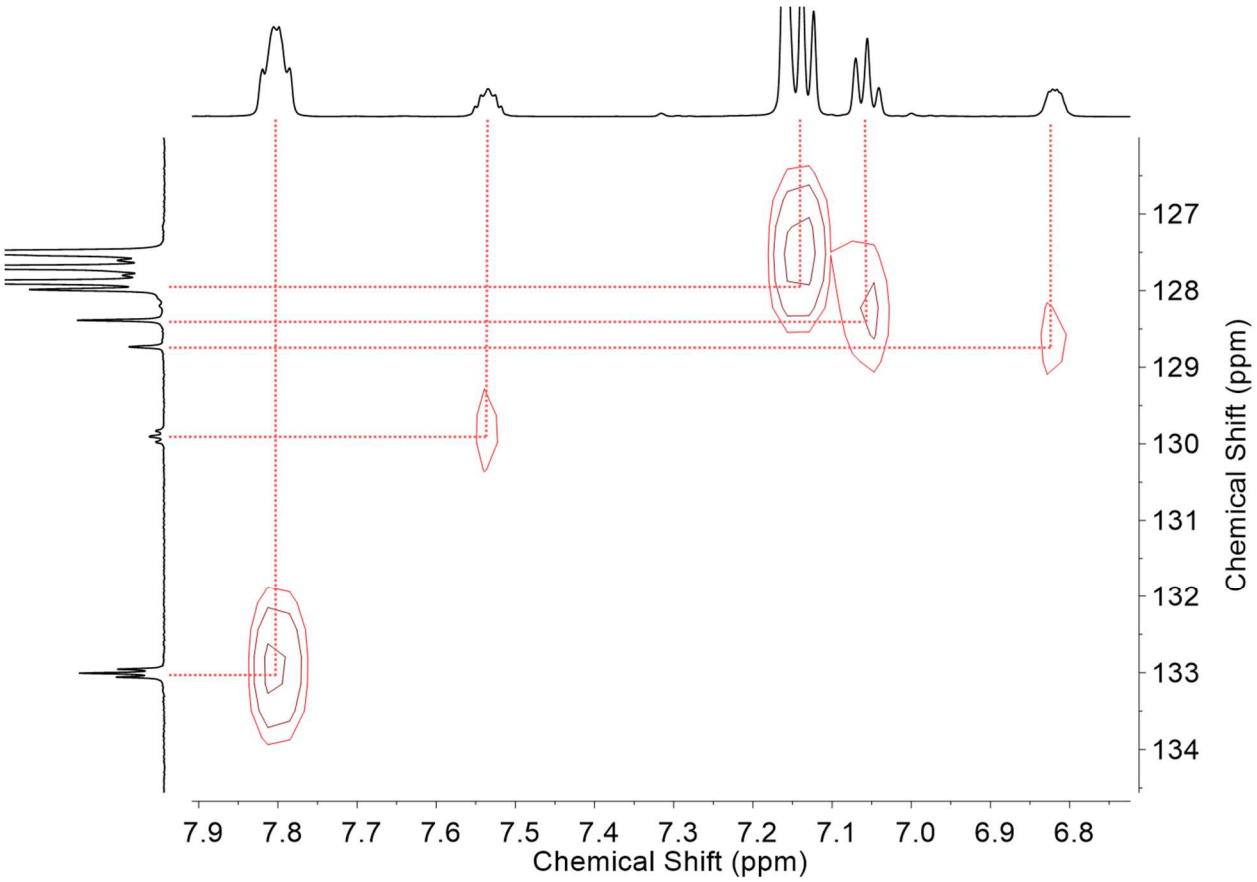

Figure A2.9: Aromatic region of $^{1}H - ^{13}C\{^{1}H\}$ HSQC spectrum (500 – 126 MHz, C_6D_6) of **2**.

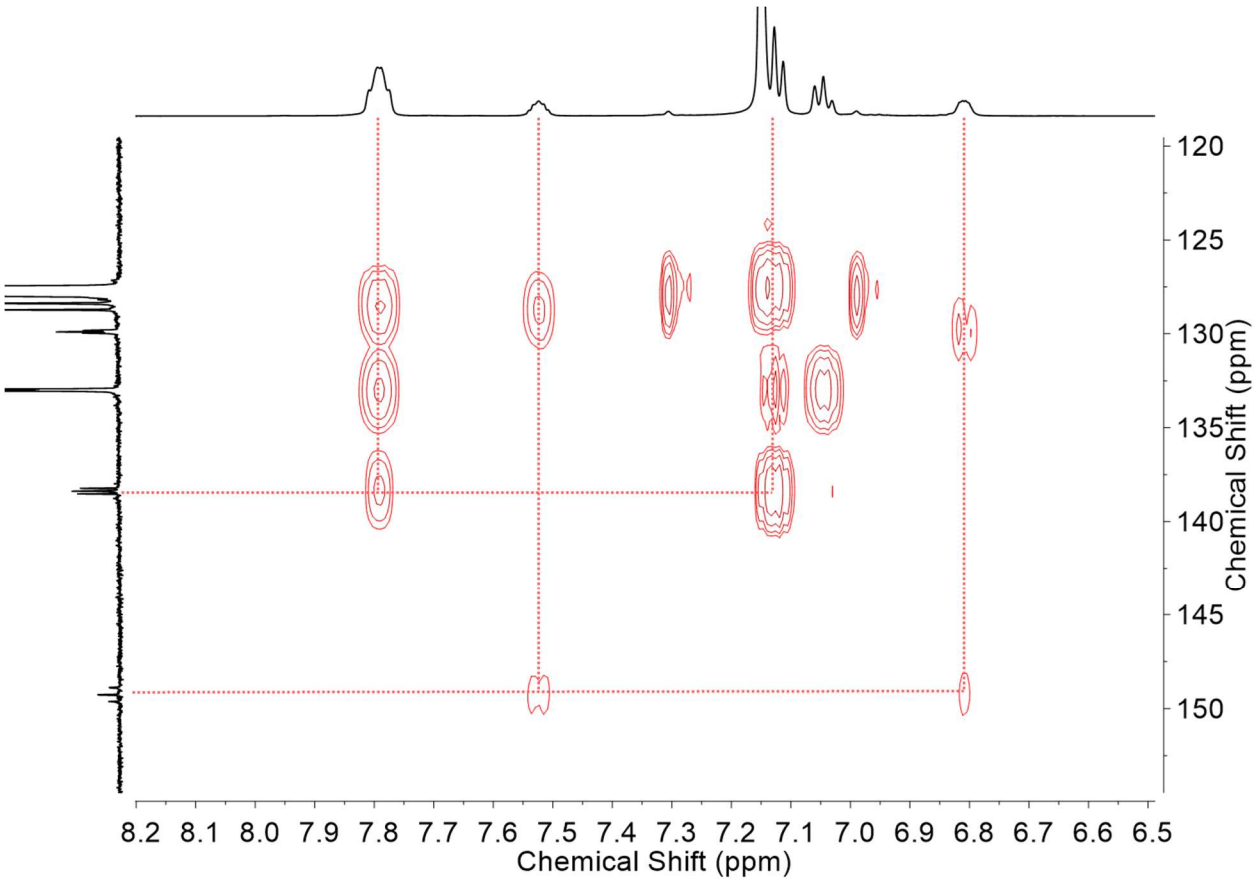

Figure A2.10: Aromatic region of $^{1}H - ^{13}C\{^{1}H\}$ HMBC spectrum (500 – 126 MHz, C_6D_6) of **2**.

2D NMR Analysis of 5

As evidenced in Figure A2.11, assignment of peaks in the aliphatic region of the proton and carbon NMRs of **5** is relatively straightforward. The clear Cp* methyl signals for each nuclei couple to each other by HSQC. Assuming that in the $^{13}C\{^{1}H\}$ spectrum the more downfield triplet with a larger magnitude coupling constant represents the carbon environment directly adjacent to the phosphorus substituent, the identities of the two Cp proton environments can be to determined based on cross peaks with the assigned carbon environments. Similarly, in the aromatic region (Figure A2.12), assignment of the proton peaks as the *ortho*, *meta*, and *para* positions of the phenyl rings by analogy to **2** facilitates assignment of the ^{13}C peaks representing the carbon nuclei they are directly bonded to. While there is significant overlap between one of the carbon signals and

the benzene solvent residual peak, there is enough separation between the corresponding proton signals that a clear cross peak emerges for the *para* position.

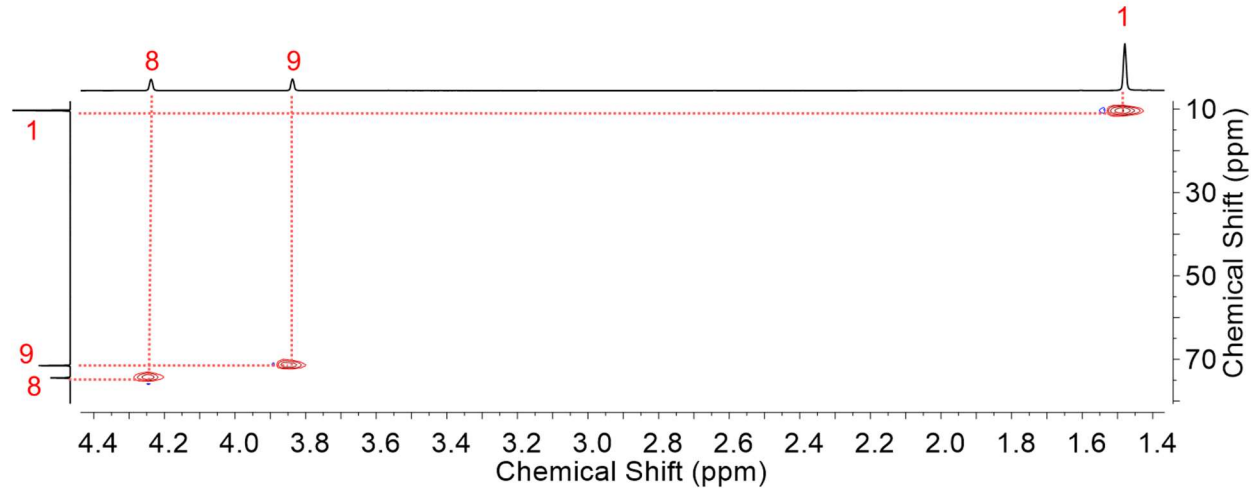

Figure A2.11: Aliphatic region of $^{1}H - ^{13}C\{^{1}H\}$ HSQC spectrum (500 – 126 MHz, C_6D_6) of **5**.

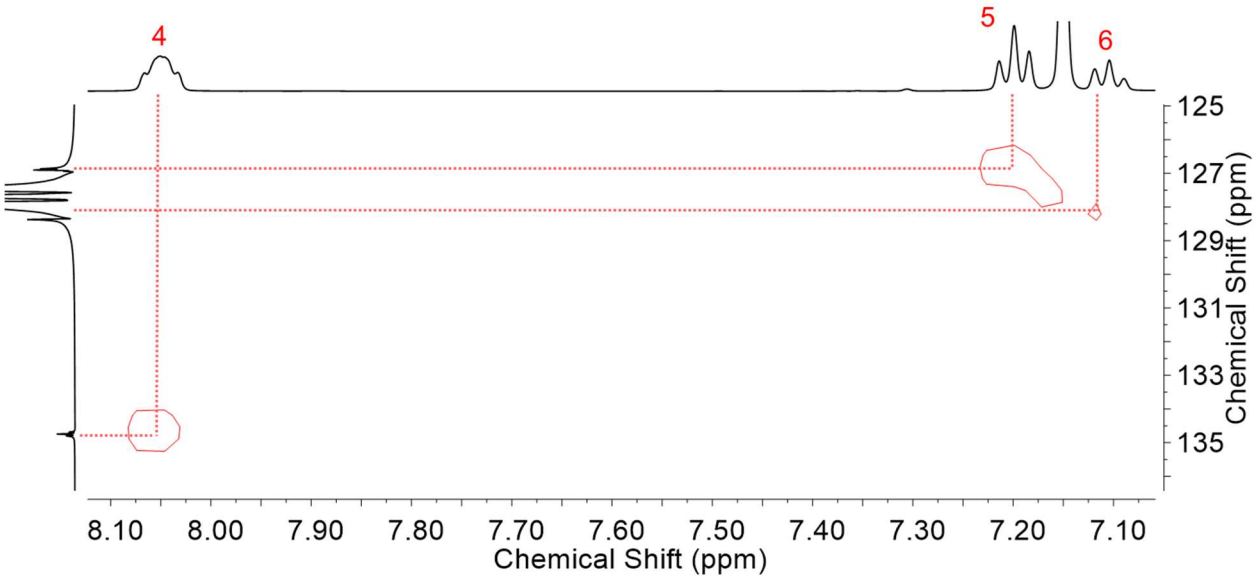

Figure A2.12: Aromatic region of $^{1}H - ^{13}C\{^{1}H\}$ HSQC spectrum (500 – 126 MHz, C_6D_6) of **5**.

Appendix 3

CRYSTALLOGRAPHIC INFORMATION

Refinement Details for 1 and 3

Sets of diffraction data [30098(**1**) and 63680(**3**) reflections using 1º-wide ω- or ϕ-scan frames with scan times of 6-12 seconds (**1**) or 5-20 seconds (**3**)] were collected[82] for single-domain crystals of **1** and **3** using monochromated Cu Kα radiation (λ=1.54178 Å) on a Bruker Proteum Single Crystal Diffraction System with dual CCD detectors and associated Helios high-brilliance multilayer optics and a shared Bruker MicroSTAR microfocus Cu rotating anode x-ray source operating at 45 kV and 60 mA. Data for both compounds were collected with an Apex II CCD detector. The integrated data[83] were corrected empirically for variable absorption effects using equivalent reflections. The Bruker software package SHELXTL was used to solve both structures using "direct methods" techniques. All stages of weighted full-matrix least-squares refinement were conducted using F_o^2 data with the SHELXTL XL v2014 software package.[84] Final crystallographic details are summarized in Table A3.1.

The asymmetric unit of **1** contains one $[Cp^*Rh(dppb)(Cl)]^+$ cation, one disordered $[PF_6]^-$ anion and a disordered tetrahydrofuran molecule of crystallization. The asymmetric unit of **3** contains one $[Cp^*Rh(dppb)(H)]^+$ cation and one triflate anion. The final structural models for both structures incorporated anisotropic thermal parameters for all nonhydrogen atoms and isotropic thermal parameters for all incorporated hydrogen atoms. Although most of the Cp* and dppb hydrogen atoms for both structures appeared in difference Fourier maps, they were placed at riding model idealized positions in the final cycles of least squares refinement. Cp* methyl groups for both structures were incorporated into the structural models as idealized rigid groups (using sp^3-hybridized geometry and a C-H bond length of 0.98 Å) that were allowed to rotate about their C-C bonds in least-squares refinement cycles. The dppb hydrogen atoms for both structures were included in the structural model as idealized atoms (assuming sp^2-hybridization of the carbon

atoms and C-H bond lengths of 0.95 Å). The isotropic thermal parameters of all idealized hydrogen atoms in both structures were fixed at values 1.2 (non-methyl) or 1.5 (methyl) times the equivalent isotropic thermal parameter of the carbon atom to which they are covalently bonded. The coordinated hydride hydrogen atom in **3** was located from a difference Fourier (third highest peak) and included in the least squares refinement as an independent isotropic atom whose parameters were allowed to vary in least-squares refinement cycles.

The $[PF_6]^-$ anion in **1** is disordered with two preferred (54%/46%) orientations in the lattice. The bond lengths and angles for the minor orientation were restrained to have similar values to those of the major orientation. The THF molecule of crystallization in **1** is also disordered. Since it was not possible to unambiguously distinguish between carbon and oxygen atoms, hydrogen atoms were not included in the structural model for this moiety. One atom in the ring is 65/35 disordered between two envelop positions for the ring. Based on combined electron density and refinements of occupancy factors, this disordered atom was eventually assigned as the ring oxygen. It was necessary to eventually restrain the positions of atoms in this THF molecule of crystallization. This was done by restraining the C-C and C-O bond lengths and the C-C-C, C-C-O and C-O-C bond angles to appropriate tetrahedral multiples of a free variable incorporated for the C-C bond length that refined to a final value of 1.41(1) Å. Mild restraints were applied to the anisotropic thermal parameters of the minor-occupancy (35%) THF oxygen atom (O1S′).

Table A3.1. Crystal and Refinement Data for [Cp*Rh(dppb)(Cl)] [PF_6] •THF(**1**) and [Cp*Rh(dppb)(H)]- [OTf] (**3**).

	1	**3**
CCDC number	1819758	1819757
Empirical formula	$C_{44}H_{39}ClF_6OP_3Rh$	$C_{41}H_{40}F_3O_3P_2RhS$
Formula weight	929.02	834.64
Temperature	200(2) K	200(2) K
Wavelength	1.54178 Å	1.54178 Å
Crystal system	Monoclinic	Orthorhombic
Space group	$P2_1/c$ - C_{2h}^5 (No. 14)	Pbca - D_{2h}^{15} (No. 61)
a	17.1256(6) Å	16.3843(3) Å
b	15.5204(6)Å	16.4369(3) Å
c	18.0614(7)Å	28.2029(5) Å
a	90.00°	90.00°
β	117.307(2)°	90.00°
γ	90.00°	90.00°
Volume	4265.7(3)Å^3	7595.2(2) Å^3
Z	4	8
Density (calculated)	1.447 g/cm^3	1.460 g/cm^3
Absorption coefficient	5.39 mm^{-1}	5.39 mm^{-1}
F(000)	1888	3424
Crystal size	0.095 x 0.055 x 0.040 mm^3	0.71 x 0.20 x 0.11 mm^3
Theta range	2.90 to 70.36°	3.13 to 70.36°
Index ranges	$-20\leq h\leq 15$, $-18\leq k\leq 17$, $-20\leq l\leq 22$	$-20\leq h\leq 18$, $-19\leq k\leq 16$, $-32\leq l\leq 33$
Reflections collected	30098	63680
Independent reflections	7680 [R_{int} = 0.058]	7114 [[R_{int} = 0.088]
Completeness to θ = 66°	96.7 %	99.2 %
Absorption correction	Multi-scan	Multi-scan
Max. and min. transmission	1.000 and 0.730	1.000 and 0.723
Refinement method	Full-matrix least-squares on F^2	Full-matrix least-squares on F^2
Data / restraints / parameters	7680/41/584	7114/0/469
Goodness-of-fit on F^2	1.037	1.018
Final R indices [I>2σ(I)]	R1[a] = 0.046, wR2[b] = 0.116	R_1 = 0.039, wR_2 = 0.093
R indices (all data)	R1 = 0.057, wR2 = 0.125	R_1 = 0.055, wR_2 = 0.102
Largest diff. peak and hole	0.80 and -0.48 e$^-$/Å^3	1.25 and -1.44 e$^-$/Å^3

[a] $R1\ \Sigma||F_o|-|F_c|| / \Sigma|F_o|$ [b] $wR2 = [\ \Sigma\ [w(F_o^2-F_c^2)^2] / \Sigma\ [w(F_o^2)^2]\ ]^{1/2}$

Table A3.2: Selected Bond Lengths for **1** and **3**.

Bond	**1** (Å)	**3** (Å)
Rh–P1	2.2947(8)	2.2405(9)
Rh–P2	2.3135(8)	2.2605(8)
Rh–Cp*	1.870	1.886
Rh–H17	—	1.76(7)

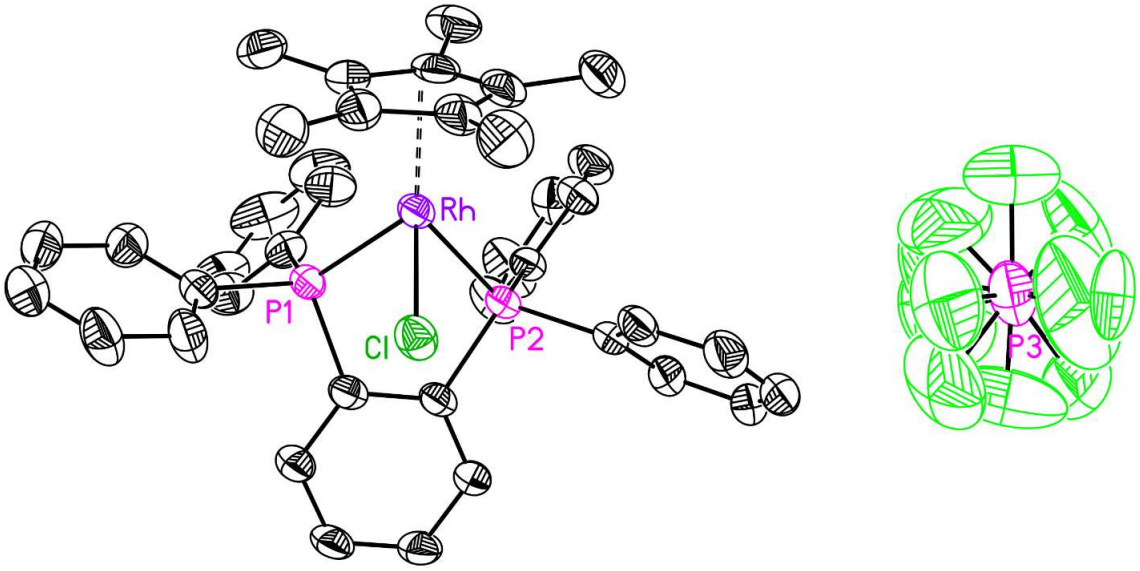

Figure A3.1: Full solid-state structure of **1**. Hydrogen atoms and associated solvent molecule omitted for clarity. Displacement ellipsoids shown at the 50% probability level.

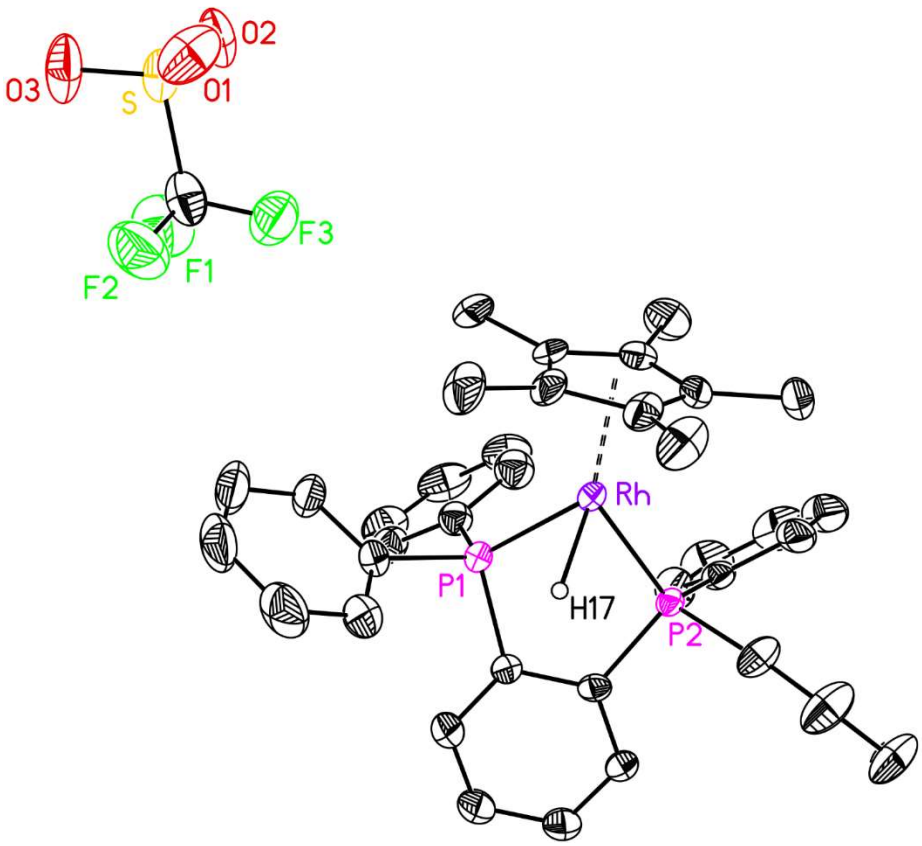

Figure A3.2: Full solid-state structure of **3**. Hydrogen atoms except H17 omitted for clarity. Displacement ellipsoids shown at the 50% probability level.

References

[1] Brown, D. U.S. Hydrogen Production. *Cryogas International*, **2016**, 22-23.

[2] Randolph, K.; Miller, E.; Peterson, D.; Lyubovsky, M.; Cierpik-Gold, K.; Sink, C.; Li, D.; Holladay, J.; Chapman, B.; Soto, H.; Rufael, T. Hydrogen Production Technical Team Roadmap. *U.S. DRIVE Partnership*. **2017**.

[3] Wiedner, E.; Chambers, M.; Pitman, C.; Bullock, R.; Miller, J.; Appel, A. Thermodynamic Hydricity of Transition Metal Hydrides. *Chem. Rev.* **2016**, *116*, 8655-8692.

[4] Pegis, M.; Roberts, J.; Wasylenko, D.; Mader, E.; Appel, A.; Mayer, J. Standard Reduction Potentials for Oxygen and Carbon Dioxide Couples in Acetonitrile and *N,N*-Dimethylformamide. *Inorg. Chem.* **2015**, *54*, 11883-11888.

[5] Kölle, U.; Grätzel, M. Rhodium(III) Complexes as Homogeneous Catalysts for the Photoreduction of Protons to Hydrogen. *Angew. Chem.* **1987**, *99*, 572-574.

[6] Muckerman, J. T.; Skone, J. H.; Ning, M.; Wasada-Tsutsui, Y. Toward the Accurate Calculation of pK_a Values in Water and Acetonitrile. *Biochim. Biophys. Acta Bioenerg.* **2013**, *1827*, 882-891.

[7] Henke, W. C.; Lionetti, D.; Moore, W. N. G.; Hopkins, J. A.; Day, V. W.; Blakemore, J. D. Ligand Substituents Govern the Efficiency and Mechanistic Path of Hydrogen Production with [Cp*Rh] Catalysts. *ChemSusChem* **2017**, *10*, 4589-4598.

[8] Ruppert, R.; Herrmann, S.; Steckhan, E. Efficient indirect electrochemical in-situ regeneration of NADH: electrochemically driven enzymatic reduction of pyruvate catalyzed by d-Idh. *Tetrahedron Lett.* **1987**, *28*, 6583-6.

[9] Cosnier, S.; Deronzier, A.; Vlachopoulos, N. Carbon/poly[pyrrole-$[(C_5Me_5)Rh(III)(bpy)Cl]^+$] Modified Electrodes; a Molecularly-Based Material for Hydrogen Evolution (bpy = 2,2'-bipyridine) *J. Chem. Soc., Chem. Commun.* **1989**, 1259-1261.

[10] Caix, C.; Chardon-Noblat, S.; Deronzier, A.; Moutet, J. -C.; Tingry, S. (Pentamethylcyclopentadienyl)(polypyridyl)rhodium and Iridium Complexes as Electrocatalysts for the Reduction of Protons to Dihydrogen and the Hydrogenation of Organics. *J. Organomet. Chem.* **1997**, *540*, 105-111.

[11] Blakemore, J. D.; Gupta, A.; Warren, J. J.; Brunschwig, B. S.; Gray, H. B. Noncovalent Immobilization of Electrocatalysts on Carbon Electrodes for Fuel Production. *J. Am. Chem. Soc.* **2013**, *135*, 18288-18291.

[12] Kölle, U.; Kang, B. S.; Infelta, P.; Comte, P.; Grätzel, M. Electrochemical and Pulse-Radiolytic Reduction of (Pentamethylcyclopentadienyl)(polypyridyl)rhodium Complexes. *Chem. Ber.* **1989**, *122*, 1869-1880.

[13] Lo, H. C.; Leiva, C.; Buriez, O.; Kerr, J. B.; Olmstead, M. M.; Fish, R. H. Regioselective Reduction of NAD^+ Models, 1-Benzylnicotinamide Triflate and β-Nicotinamide Ribose-5'-methyl Phosphate, with in Situ Generated $[CpRh(Bpy)H]^+$: Structure-Activity Relationships, Kinetics, and Mechanistic Aspects in the Formation of the 1,4-NADH Derivatives. *Inorg. Chem.* **2001**, *40*, 6705-6716.

[14] Steckhan, E.; Herrmann, S.; Ruppert, R.; Dietz, E.; Frede, M.; Spika, E. Analytical Study of a Series of Substituted (2,2'-bipyridyl)(pentamethylcyclopentadienyl)rhodium and -iridium Complexes with Regard to their Effectiveness as Redox Catalysts for the Indirect Electrochemical and Chemical Reduction of $NAD(P)^+$. *Organometallics* **1991**, *10*, 1568-1577.

[15] Abura, T.; Ogo, S.; Watanabe, Y.; Fukuzumi, S. Isolation and Crystal Structure of a Water-Soluble Iridium Hydride: A Robust and Highly Active Catalyst for Acid-Catalyzed Transfer Hydrogenations of Carbonyl Compounds in Acidic Media. *J. Am. Chem. Soc.* **2003**, *125*, 4149-4154.

[16] Kütt, S.; Rodima, T.; Saame, J.; Raamat, E.; Mäemets, V.; Kaljurand, I.; Koppel, I. A.; Garlyauskayte, R. Y.; Yagupolskii, Y. L.; Yagupolskii, L. M.; Bernhardt, E.; Willner, H.; Leito, I. J. Equilibrium Acidities of Superacids. *Org. Chem.* **2011**, *76*, 391-395.

[17] Pitman, C. L.; Finster, O. N. L.; Miller, A. J. M. Cyclopentadiene-Mediated Hydride Transfer from Rhodium Complexes. *Chem. Commun.* **2016**, *52*, 9105-9108.

[18] Quintana, L. M. A.; Johnson, S. I.; Corona, S. L.; Villatoro, W.; Goddard, W. A.; Takase, M. K.; VanderVelde, D. G.; Winkler, J. R.; Gray, H. B.; Blakemore, J. D. Proton-Hydride Tautomerism in Hydrogen Evolution Catalysis. *Proc. Nat. Acad. Sci. U.S.A.* **2016**, *113*, 6409-6414.

[19] Peng, Y.; Ramos-Garcés, M. V.; Lionetti, D; Blakemore, J. D. Structural and Electrochemical Consequences of [Cp*] Ligand Protonation. *Inorg. Chem*. **2017**, *56*, 10824-10831.

[20] Chalkley, M. J.; Oyala, P. H.; Peters, J. C. Cp* Noninnocence leads to a Remarkably Weak C–H Bond via Metallocene Protonation. *J. Am. Chem. Soc.* **2019**, *141*, 4721-4729.

[21] Johnson, S. I.; Gray, H. B.; Blakemore, J. D.; Goddard, W. A. Role of Ligand Protonation in Dihydrogen Evolution from a Pentamethylcyclopentadienyl Rhodium Catalyst. *Inorg. Chem.* **2017**, *56*, 11375-11386.

[22] Klingert, B.; Werner, H. Basic Metals. XLII. Metal Basicity of the Complexes $C_5Me_5Rh(PMe_3)_2$, $C_5Me_5Rh(C_2H_4)PMe_3$, and $C_5Me_5Rh(C_2H_4)P_2Me_4$: New Pentamethylcyclopentadienyl rhodium(I) and -rhodium(III) Compounds. *Chem. Ber.* **1983**, *116*, 1450-1462.

[23] Faller, J. W.; D'Alliessi, D. G. Tunable Stereoselective Hydrosilylation of PhC≡CH Catalyzed by Cp*Rh Complexes. *Organometallics* **2002**, *21*, 1743-1746.

[24] Chow, P.; Zargarian, D.; Taylor, N. J.; Marder, T. B. Synthesis of Hydrido-bis(acetylide) Complexes of Rhodium and the Molecular Structures of Mer-trans-$[Rh(PMe_3)_3(H)(C{\equiv}CPh)_2]$ and Mer-trans-$[\{Rh(dmpe)(H)(C{\equiv}CSiMe_3)_2\}_2(\mu\text{-dmpe})]$ (dmpe = $Me_2PCH_2CH_2PMe_2$). *J. Chem. Soc., Chem. Commun.* **1989**, 1545-1547.

[25] Zhang, F.; Jia, J.; Dong, S.; Wang, W.; Tung, C.-H., *Organometallics* **2016,** *35*, 1151-1159.

[26] Faraone, F.; Bruno, G.; Schiavo, S. L.; Tresoldi, G.; Bombieri, G. η^5-Cyclopentadienylrhodium(I) complexes containing diphosphines and their reactions with the electrophiles H^+ and Me^+. Crystal and molecular structure of $[Rh(\eta^5\text{-}C_5H_5)(CO)(Ph_2PCH_2PPh_2)]$, a complex with a unidentate bis(diphenylphosphino)methane ligand. *J. Chem. Soc., Dalton Trans.* **1983**, 433-438.

[27] Klingert, B.; Werner, H. Synthesis and Reactivity of $[C_5Me_5Rh(\mu\text{-}PMe_2)]_2$: Addition and Insertion Reactions of Oxygen and its Homologs to the Rh_2P_2 Unit. *J. Organomet. Chem.* **1983**, *252*, C47-C52.

[28] Klingert, B.; Werner, H. Metal Complexes with Bridging Dimethylphosphido Ligands. VIII. Protonation of Doubly Bridged Pentamethylcyclopentadienylrhodium(II) Complexes and Subsequent Reactions of the μ-hydridodirhodium Cation $[(C_5Me_5Rh)_2(\mu\text{-}PMe_2)_2(\mu\text{-}H)]^+$. *J. Organomet. Chem.* **1987**, *333*, 119-128.

[29] Jones, W. D.; Kuykendall, V. L.; Selmeczy, A. D. Ring Migration Reactions of (C_5Me_5) $Rh(PMe_3)H_2$. Evidence for η3 Slippage and Metal-to-Ring Hydride Migration. *Organometallics* **1991**, *10*, 1577-1586.

[30] Edelbach, B. L.; Jones, W. D. Mechanism of Carbon-Fluorine Bond Activation by (C_5Me_5) $Rh(PMe_3)H_2$. *J. Am. Chem. Soc.* **1997**, *119*, 7734-7742.

[31] Gelabert, R.; Moreno, M.; Lluch, J. M.; Lledós, A.; Pons, V.; Heinekey, D. M. Synthesis and Properties of Compressed Dihydride Complexes of Iridium: Theoretical and Spectroscopic Investigations. *J. Am. Chem. Soc.* **2004**, *126*, 8813-8822.

[32] (a) Roy, S.; Sharma, B.; Pécaut, J.; Simon, P.; Fontecave, M.; Tran, P. D.; Derat, E.; Artero, V. Molecular Cobalt Complexes with Pendant Amines for Selective Electrocatalytic Reduction of Carbon Dioxide to Formic Acid. *J. Am. Chem. Soc.* **2017,** *139*, 3685-3696. (b) Elgrishi, N.; Kurtz, D. A.; Dempsey, J. L. Reaction Parameters Influencing Cobalt Hydride Formation Kinetics: Implications for Benchmarking H_2-Evolution Catalysts. *J. Am. Chem. Soc.* **2017,** *139*, 239-244

[33] Castillo, C. E.; Stoll, T.; Sandroni, M.; Gueret, R.; Fortage, J.; Kayanuma, M.; Daniel, C.; Odobel, F.; Deronzier, A.; Collomb, M.-N., *Inorg. Chem.* **2018,** *57*, 11225-11239.

[34] Dadci, L.; Elias, H.; Frey, U.; Hoernig, A.; Koelle, U.; Merbach, A. E.; Paulus, H.; Schneider, J. S. π-Arene Aqua Complexes of Cobalt, Rhodium, Iridium, and Ruthenium: Preparation, Structure, and Kinetics of Water Exchange and Water Substitution. *Inorg. Chem.* **1995**, *34*, 306-315.

[35] Farrer, N. J.; McDonald, R.; Piga, R.; McIndoe, J. S. Bisphosphine Monoxides with *o*-phenylene Backbones in Pt, Pd and Fe Complexes. *Polyhedron* **2010**, *29*, 254-261.

[36] Reinhardt, R.; Kaim, W. Complexes of α-diimines with Pentamethylcyclopentadienylrhodium in Different Oxidation States. *Z. Anorg. Allg. Chem.* **1993**, *619*, 1998-2005.

[37] Kaim, W.; Reinhardt, R.; Waldhoer, E.; Fiedler, J. Electron Transfer and Chloride Ligand Dissociation in Complexes $[(C_5Me_5)ClM(bpy)]^+/[(C_5Me_5)M(bpy)]^n$ (M = Co, Rh, Ir; n = 2+, +, 0, -): A Combined Electrochemical and Spectroscopic Investigation. *J. Organomet. Chem.* **1996**, *524*, 195-202.

[38] Lionetti, D.; Day, V. W.; Blakemore, J. D. Synthesis and Electrochemical Properties of Half-Sandwich Rhodium and Iridium Methyl Complexes. *Organometallics* **2017**, *36*, 1897-1905.

[39] Blakemore, J. D.; Hernandez, E. S.; Sattler, W.; Hunter, B. M.; Henling, L. M.; Brunschwig, B. S.; Gray, H. B. Pentamethylcyclopentadienyl Rhodium Complexes. *Polyhedron* **2014**, *84*, 14-18.

[40] Connelly, N. G.; Geiger, W. E. Chemical Redox Agents for Organometallic Chemistry. *Chem. Rev.* **1996**, *96*, 877-910.

[41] Lionetti, D.; Hopkins, J. A.; Boyd, E. A.; Peng, Y.; Lassalle-Kaiser, B.; Blakemore, J. D. Determining the Thermochemical Influence of Metal- versus Ligand-Centered Protonation in Half-Sandwich Complexes. *In preparation.*

[42] Appel, A. M.; Helm, M. L. Determining the Overpotential for a Molecular Electrocatalyst. *ACS Catalysis* **2013**, *4*, 630-633.

[43] Schmidtmann, M.; Coster, P.; Henry, P. F.; Ting, V. P.; Weller, M. T.; Wilson, C. C. Determining hydrogen positions in crystal engineered organic molecular complexes by joint neutron powder and single crystal X-ray diffraction. *CrystEngComm* **2014,** *16*, 1232-1236.

[44] Appel, A. M.; Helm, M. L. Determining the Overpotential for a Molecular Electrocatalyst. *ACS Catalysis* **2013**, *4*, 630-633.
[45] Warren, J. J.; Tronic, T. A.; Mayer, J. M. Thermochemistry of Proton-Coupled Electron Transfer Reagents and its Implications. *Chem. Rev.* **2010**, *110*, 6961-7001.
[46] Waldie, K. M.; Ostericher, A. L.; Reineke, M. H.; Sasayama, A. F.; Kubiak, C. P. Hydricity of Transition-Metal Hydrides: Thermodynamic Considerations for CO_2 Reduction. *ACS Catal.* **2018,** *8*, 1313-1324.
[47] Dempsey, J. L.; Winkler, J. R.; Gray, H. B. Mechanism of H_2 Evolution from a Photogenerated Hydridocobaloxime. *J. Am. Chem. Soc.* **2010,** *132*, 16774-16776.
[48] Chambers, M. B.; Kurtz, D. A.; Pitman, C. L.; Brennaman, M. K.; Miller, A. J. M. Efficient Photochemical Dihydrogen Generation Initiated by a Bimetallic Self-Quenching Mechanism. *J. Am. Chem. Soc.* **2016,** *138*, 13509-13512.
[49] Creutz, C. Bipyridine Radical Ions. *Comments Inorg. Chem.* **1982**, *1*, 293-311.
[50] Bock, H.; Lechner-Knoblauch, U.; Hänel, P. Radical Ions. 70. The Effect of Phosphorus Substituents on the Cyclic Voltammetric Reduction of Aromatic π-systems. *Chem. Ber.* **1986**, *119*, 3749-3765.
[51] Price, A. J.; Ciancanelli, R.; Noll, B. C.; Curtis, C. J.; DuBois, D. L.; DuBois, M. R. $HRh(dppb)_2$, a Powerful Hydride Donor. *Organometallics* **2002**, *21*, 4833-4839.
[52] Liao, J. L.; Devereux Leon, R.; Fox, M. A.; Yang, C. C.; Chiang, Y. C.; Chang, C. H.; Lee, G. H.; Chi, Y. Role of the Diphosphine Chelate in Emissive, Charge-Neutral Iridium(III) Complexes. *Chem. – Eur. J.* **2017**, *24*, 624-635.
[53] de Bruin, B.; Lyaskovskyy, V. Redox Non-Innocent Ligands: Versatile New Tools to Control Catalytic Reactions. *ACS Catal.* **2012**, *2*, 270-279.
[54] Chirik, P. J.; Wieghardt, K. Radical Ligands Confer Nobility on Base-Metal Catalysts. *Science* **2010**, *327*, 794-795.
[55] Moore, W. N. G.; Henke, W. C.; Lionetti, D.; Day, V. W.; Blakemore, J. D. Single-Electron Redox Chemistry on the [Cp*Rh] Platform Enabled by a Nitrated Bipyridyl Ligand. *Molecules*, **2018**, *23*, 2857.
[56] Hopkins, J. A.; Lionetti, D.; Day, V. W.; Blakemore, J. D. Chemical and Electrochemical Properties of [Cp*Rh] Complexes Supported by a Hybrid Phosphine-Imine Ligand. *Organometallics*, **2019**, *38*, 1300-1310.
[57] Miller, T. M.; Ahmed, K. J.; Wrighton, M. S. Complexes of Rhenium Carbonyl Containing Ferrocenyl-Derived Ligands: Tunable Electron Density at Rhenium by Control of the Redox State of the Ferrocenyl Ligand. *Inorg. Chem.* **1989**, *28*, 2347-2355.
[58] Sassano, C. A.; Mirkin, C. A. Degenerate Exchange Reactions: A Novel and General Way to Determine the Thermodynamic Perturbations on Transition Metal Complexes that Result from Ligand Oxidation. *J. Am. Chem. Soc.* **1995**, *117*, 11379-11380.
[59] Beer, P. D. Redox-Responsive Macrocyclic Receptor Molecules Containing Transition-Metal Redox Centers. *Chem. Soc. Rev.* **1989**, *18*, 409-450.
[60] Saji, T. Electrochemical Ion Transport with Ferrocene Functionalized Crown Ether. *J. Chem. Soc. Commun.* **1986**, *9*, 716-717.
[61] Lorkovic, I. M.; Duff, R. R.; Wrighton, M. S. Use of the Redox-Active Ligand 1,1'-Bis(diphenylphosphino)cobaltocene to Reversible Alter the Rate of the Rhodium(I)-Catalyzed Reduction and Isomerization of Ketones and Alkenes. *J. Am. Chem. Soc.* **1995**, *117*, 3617-3618.

[62] Ma, J. F.; Yamamoto, Y. Preparation and Reactions of the (Pentamethylcyclopentadienyl)rhodium(III) Complexes Bearing 1,1'-bis(diphenylphosphinomethyl)ferrocene (dpmf) or 1,1'-bis(diphenylphosphino)ferrocene (dppf). *J. Organomet. Chem.* **1999**, *574*, 148-154.
[63] Sixt, T.; Fiedler, J.; Kaim, W. Iron Versus Ruthenium Oxidation in 1,1'-bis(diphenylphosphino)ferrocene-ruthenium(II) complexes: EPR and Spectroelectrochemical Evidence. *Inorg. Chem. Comm.* **2000**, *3*, 80-82.
[64] Boyd, E. A.; Lionetti, D.; Henke, W. C.; Day, V. W.; Blakemore, J. D. Preparation, Characterization, and Electrochemical Activation of a Model [Cp*Rh] Hydride. *Inorg. Chem.* **2019**, *58*, 3606-3615.
[65] Dierkes, P.; van Leeuwen, P. W. N. M. The Bite Angle Makes the Difference: a Practical Ligand Parameter for Dipihosphine Ligands. *Dalton. Trans.* **1999**, 1519-1529.
[66] Miedaner, A.; Haltiwanger, R. C.; DuBois, D. L. Relationship between the Bite Size of Diphosphine Ligands and Tetrahedral Distortions of "Square-Planar" Nickel (II) Complexes: Stabilization of Nickel(I) and Palladium(I) Complexes Using Diphosphine Ligands with Large Bites. *Inorg. Chem.* **1991**, *30*, 417-427.
[67] Elschenbroich, C.; Bilger, E.; Ernst, R. D.; Wilson, D. R.; Kralik, M. S. Closed, Half-Open, and Open Ferrocenes: Redox Behavior and Electron Spin Resonance of the Radical Cations. *Organometallics* **1985**, *4*, 2068.
[68] Fuchigami, K.; Rath, N. P.; Mirica, L. M. Mononuclear Rhodium(II) and Iridium(II) Complexes Supported by Tetradentate Pyridinophane Ligands. *Inorg. Chem. Comm.* **2017**, 9404-9408.
[69] Dixon, F. M.; Masar, M. S.; Doan, P. E.; Farrell, J. R.; Arnold, F. P.; Mirkin, C. A.; Incarvito, C. D.; Zakharov, L. N.; Rheingold, A. L. Rh(II) and Rh(I) Two-Legged Piano-Stool Complexes: Structure, Reactivity, and Electronic Properties. *Inorg. Chem.* **2003**, *42*, 3245-3255.
[70] Garrido, G.; Koort, E.; Rafols, C.; Bosch, E.; Rodima, T.; Leito, I.; Roses, M. Acid-Base Equilibria in Nonpolar Media: Absolute pK_a Scale of Bases in Tetrahydrofuran. *J. Org. Chem.* **2006**, *71*, 9062-9067.
[71] Helpful discussions with Davide Lionetti and Julie Hopkins.
[72] Cappellani, E. P.; Drouin, S. D.; Jia, G.; Maltby, P. A.; Morris, R. H.; Schweitzer, C. T. Effect of the Ligand and Metal on the pK_a Values of the Dihydrogen Ligand in the Series of Complexes $[M(H_2)H(L)_2]^+$, M = Fe, Ru, Os, Containing Isosteric Ditertiaryphosphine Ligands, L. *J. Am. Chem. Soc.* **1994**, *116*, 3375-3388.
[73] Allgeier, A. M.; Slone, C. S.; Mirkin, C. A.; Liable-Sands, L. M.; Yap, G. P. A.; Rheingold, A. L. Electrochemically Controlling Ligand Binding Affinity for Transition Metals via RHLs: The Importance of Electrostatic Effects. *J. Am. Chem. Soc.* **1997**, *119*, 550-559.
[74] Afeefy, H. Y.; Liebman, J. F.; Stein, S. E. Neutral Thermochemical Data. In NIST Chemistry WebBook, NIST Standard Reference Database Number 69; Linstrom, P. J., Mallard, W. G., Eds.; National Institute of Standards and Technology: Gaithersburg, MD, 20899; http://webbook.nist.gov (retrieved May 5, 2019).
[75] Hydrogen and Deuterium. In IUPAC Solubility Data Series, Vols. 5/6; Young, C. L., Ed.; Permagon: New York, 1981.
[76] Roduner, E. Hydrophobic Solvation, Quantum Nature, and Diffusion of Atomic Hydrogen in Liquid Water. *Radiat. Phys. Chem*. **2005**, *72*, 201.

[77] Rudie, A. W.; Lichtenberg, D. W.; Katcher, M. L.; Davison, A. Comparative Study of 1,1`-bis(diphenylphosphino)cobaltocenium hexafluorophosphate and 1,1`-bis(diphenylphosphino)ferrocene as Bidentate Ligands. *Inorg. Chem.* **1978**, *17*, 2859-2863.
[78] White, C.; Yates, A.; Maitlis, P. M. (η^5-Pentamethylcyclopentadienyl)rhodium and -iridium Compounds. *Inorg. Synth.* **1992**, *29*, 228-234.
[79] Fulmer, G. R.; Miller, A. J. M.; Sherden, N. H.; Gottlieb, H. E.; Nudelman, A.; Stoltz, B. M.; Bercaw, J. E.; Goldberg, K. I. NMR Chemical Shifts of Trace Impurities: Common Laboratory Solvents, Organics, and Gases in Deuterated Solvents Relevant to the Organometallic Chemist. *Organometallics* **2010**, *29*, 2176-2179.
[80] Harris, R. K.; Becker, E. D.; Cabral De Menezes, S. M.; Goodfellow, R.; Granger, P. NMR Nomenclature. Nuclear Spin Properties and Conventions for Chemical Shifts (IUPAC Recommendations 2001). *Pure Appl. Chem.* **2001**, *73*, 1795-1818.
[81] Harris, R. K.; Becker, E. D.; Cabral De Menezes, S. M.; Granger, P.; Hoffman, R. E.; Zilm, K. W. Further Conventions for NMR Shielding and Chemical Shifts (IUPAC Recommendations 2008). *Pure Appl. Chem.* **2008**, *80*, 59-84.
[82] Data Collection: SMART Software in APEX2 v2014.11-0 Suite. Bruker-AXS, 5465 E. Cheryl Parkway, Madison, WI 53711-5373 USA.
[83] Data Reduction: SAINT Software in APEX2 v2014.11-0 Suite. Bruker-AXS, 5465 E. Cheryl Parkway, Madison, WI 53711-5373 USA.
[84] Refinement: SHELXTL Software in APEX2 v2014.11-0 Suite. Bruker-AXS, 5465 E. Cheryl Parkway, Madison, WI 53711-5373 USA.